

Axion Quark Nuggets – Testing a Novel Dark Matter Model using the Cosmological Simulation ‘SLOW’ and Inferring its Observational Detectability



Master Thesis at the Faculty of Physics
Ludwig-Maximilians-University Munich

Submitted by

Julian Silvester Sommer

Supervised by

Prof. Dr. Klaus Dolag

Dr. Ludwig Böss

Dr. Ildar Khabibullin

Munich, 11th of March 2024

Axion Quark Nuggets – Überprüfung eines neuartigen Dunkle-Materie-Modells mit Hilfe der kosmologischen Simulation ‘SLOW’ und ihre Detektierbarkeit in Beobachtungen



Masterarbeit der Fakultät für Physik der
Ludwig-Maximilians-Universität München

Vorgelegt von

Julian Silvester Sommer

Betreut von

Prof. Dr. Klaus Dolag

Dr. Ludwig Böss

Dr. Ildar Khabibullin

München, den 11.03.2024

Contents

1	Introduction to Axion Quark Nuggets	1
1.1	Formation Process of Axion Quark Nuggets	2
1.2	Structure of Axion Quark Nuggets and Cosmological Properties	5
1.3	Possible Interaction Scenarios	8
1.4	Observation Proposals and Mysterious Detections	9
2	Methodology	15
2.1	Physical Description of AQNs	15
2.1.1	Internal AQN Temperatures Through Ambient Gas Interactions	15
2.1.2	Radiation Processes of AQNs	18
2.2	Emission of Simulated Particles	23
2.2.1	Mapping AQN Properties onto Halo Tracer Particles	23
2.2.2	ICM Bremsstrahlung	26
2.2.3	Radiation Through Cosmic Rays	27
2.2.4	SPH to Grid Mapping	27
2.3	The Constrained Simulation of the Local Universe ‘SLOW’	28
2.3.1	The Sample	28
3	Results	31
3.1	Environmental Impact onto Physical Properties of AQNs	31
3.1.1	Scaling Relations	31
3.1.2	Histograms	32
3.1.3	Radial Profiles	34
3.2	Spectral Profiles	36
3.2.1	Low Frequency Regime	38
3.2.2	High Frequency Regime	42
3.3	Cluster Maps	44
3.4	Observational Feasibility of Promising Cluster Candidates	48
4	Discussion	51
4.1	Comments on Observationally Motivated Phenomena	51
5	Outlook	53
5.1	Key Results	53
5.2	Future Work	55
	Appendices	75
A	Supplementary Figures	77
A.1	Spectra	77
A.2	SPH Maps of Additional Local Galaxy Clusters	77

B Supplementary Tables	87
C Abbreviations	93
D Units	95

Chapter 1

Introduction to Axion Quark Nuggets

In astronomy, we rely on observations and evidence to proof our rapidly evolving theories right or wrong. Justifying new theories through elaborate techniques accelerated our understanding of the universe from very basic concepts to sophisticated models of how objects behave and interact with each other. Light, in the form of electromagnetic waves has been the astronomer's tool of choice to study the mysteries of the universe even before telescopes were even developed. Over time, mankind discovered that smeared nebulae are in fact galaxies – islands of hundreds of billions of stars – and many more observations that expanded our knowledge of the universe immensely. But what if there is something that certainly exists but cannot be directly observed? Dark matter – historically anticipated to only interact gravitationally with its surroundings – is one prominent example. The properties of dark matter can be inferred by analyzing the velocity dispersion of galaxies in massive cosmological accumulations (Zwicky, 1933) and gravitational lensing in galaxy clusters (Reinhardt, 1971). Even though it is evident that dark matter exists, a single dark matter particle was never observed.

During Big Bang, a highly energetic environment sets the foundation for theories to emerge regarding matter and its composition. Modern theories describe a versatile zoo of dark matter models ranging from elementary particles (sterile neutrinos (Shi and Fuller, 1999, Boyarsky et al., 2006, Seljak et al., 2006, Gelmini et al., 2010), axion like particles (Hui et al., 2017)), Weakly Interacting Massive Particles (WIMPs) (Lee and Weinberg, 1977, Primack et al., 1988, Kolb and Turner, 1990), Massive Astrophysical Compact Halo Objects (MACHOS) (Alcock et al., 1993, 1998) with for instance primordial mass black holes as promising candidates (Afshordi et al., 2003, Frampton et al., 2010, Carr et al., 2016, Green and Kavanagh, 2021) and Composite Compact Objects (CCOs) exhibiting nuclear density (Witten, 1984, Farhi and Jaffe, 1984, de Rujula and Glashow, 1984), evolved from different cosmological environments. Constraints on mass, properties and number densities of these dark matter candidates can be made by various techniques. As for potential dark matter candidates, particle accelerators are instrumental in proposing mass boundaries for elementary particles, while gravitational wave detectors may aid in constraining the distribution of primordial black holes. It is rather rare that a dark matter candidate is observationally falsifiable by testing signatures in the electromagnetic spectrum.

Here we present a detailed analysis on the observational feasibility of a dark matter model that is proposed to obey properties of cold dark matter, but is still expected to be the origin of observable signatures that can be tested in a wide range of the electromagnetic spectrum, called the Axion Quark Nugget (AQN) (Zhitnitsky, 2003).

AQNs are not only capable of describing generic cold dark matter features of structure formation but also provide solutions on fundamental cosmological problems. Two of the most prominent mysteries are: (i) Why is the abundance of dark matter not extraordinarily lower or larger than the visible component? (ii) Why do we observe more matter over antimatter, and where does this imbalance come from?

As it will be described in further detail below, AQNs are capable of explaining the asymmetry of matter and antimatter and provide a natural solution why Ω_{dark} has a comparable quantity as Ω_{visible} .¹ In fact, AQNs are directly related to dark and visible matter due to a common formation process. This process further enables AQNs to exist in two forms of particle families – normal matter AQNs with a quark core surrounded by a sphere of positrons, and antimatter AQNs, consisting of an antiquark core and being surrounded by a sphere of electrons. To anticipate in general, we will follow the convention to use the abbreviation ‘AQN’ when speaking of Anti Axion Quark Nuggets throughout the thesis, as Anti Axion Quark Nuggets represent by far the most prominent electromagnetic signature out of these two families. These macroscopic particles are anticipated to interact with the surrounding gas and if ionized, a stronger interaction can be expected due to Coulomb attraction. The gas in galaxy clusters, called intracluster medium (ICM) is a highly suitable environment for both strong degrees of ionization of gas and AQNs. We therefore focus on AQN signatures in environments of galaxy clusters and analyze the impact of infalling substructures towards the central potential as they are surrounded by a dark matter halo moving through the ICM. These halos are expected to likely interact with the surrounding gas if we assume the dark matter to entirely consist of antimatter and matter AQNs. In this framework we utilize the constrained cosmological simulation of the local universe ‘SLOW’ (Dolag et al., 2023). Due to initial conditions based on real observations, a constrained cosmological simulation results from observationally cross-correlated galaxy clusters at present time. It is the aim of this Master’s Thesis to identify the most promising digital twins of observed galaxy clusters as suitable hosts to exhibit AQN signatures that can be tested with today’s state-of-the-art telescopes ranging from radio to gamma ray frequencies. Furthermore, the goal is to infer regions in cluster environments that pose the best detectability and estimate the strength of an AQN excess to be expected.

1.1 Formation Process of Axion Quark Nuggets

In order to explain the formation process of AQNs one has to describe the historic foundation of axions and their introduction by the theory of Quantum Chromodynamic (QCD). Described in the one of the most recent studies on the formation mechanism of AQNs by (Ge et al., 2017) and already introduced by (Peccei and Quinn, 1977, Kim, 1979, Dine et al., 1981), the lagrangian in a gauge theory like QCD can have an additional term:

$$\mathcal{L}_\theta = -\theta(t) \frac{g^2}{32\pi^2} \tilde{G}_{\mu\nu}^a G_{\mu\nu}^a. \quad (1.1)$$

In this term, $\theta(t)$ will later be referred to the axion field, g is the coupling constant and the gauge field $G_{\mu\nu}^a$ with its dual $\tilde{G}_{\mu\nu}^a$. This term induces a Charge-Conjugation Parity (\mathcal{CP}) violation, i.e. the phenomenon that the laws of physics do not behave in the same way under combined transformations of charge conjugation and parity. Here, charge conjugation means ‘replacing particles with their antiparticles’ and parity is referred to ‘inverting spatial coordinates’. This proposes a problem, because \mathcal{CP} violation is predicted by a theory that effortlessly describes the world we live in with many of its complexities, but this type of violation is simply not observed. Peccei and Quinn (1977) therefore introduced that the full QCD lagrangian \mathcal{L}_{QCD} should possess a chiral U(1) invariance, leading to the consequence that dynamical values of θ directly influence the definitions of different fields in \mathcal{L}_{QCD} . Different fields influenced by $\theta \neq 0$ are expected to be equivalent to a theory where $\mathcal{L}_\theta = 0$; thus, no \mathcal{CP} violation would occur. Wilczek (1978) and Weinberg (1978) independently found that a particle must be produced from the neutralizing θ field. Particles, that are the result of a field

¹ Ω_i is the dimensionless cosmological component with $\Omega_i \equiv \rho_i/\rho_{\text{crit}}$ while ρ_{crit} is the critical density in a flat Λ CDM universe.

which ‘washes away’ the problem of \mathcal{CP} violation. Described by these papers, the so-called axion (inspired by a laundry detergent from the 1970s)² is a particle that is very light and couples very weakly to ordinary matter.

In the framework of $\theta \neq 0$, the axion field can interpolate in a single vacuum state on different topological branches which we call k , i.e. $\theta \rightarrow \theta + 2\pi k$ (Vilenkin and Everett, 1982, Sikivie, 1982). These different interpolations can occur before inflation, with this phase being called the Peccei-Quinn (PC) phase. As it is pointed out by Ge et al. (2019), inflation cannot separate these different k branches, and, as a consequence, axion strings form of these different topological branches in which θ can interpolate in. This leads to the formation of a network of axion strings originating from different branches and only at a temperature of $T_{\text{osc}} \simeq 1 \text{ GeV}$, axion strings can form domain walls. Before the oscillation of the θ field (and since axion strings were formed before) the PC phase in one and the same vacuum state, the axion field is coherent and is therefore correlated on extremely large scales (Liang and Zhitnitsky, 2016) (the axion field would not be coherent for physically distinct vacuum states). This coherent state plays an important role on the value of θ that it globally possesses at the point where θ starts to oscillate, causing the string network to form domain-walls (DW) which can collapse to closed bubbles due to their topological defects. It is pointed out by Ge et al. (2017) that the DW formation is a two-stage process: because axion domain walls are formed from a single vacuum state, we will call them $N_{\text{DW}} = 1$ axion domain walls. It is because of the coherence of θ that during the DW formation a preferred matter or antimatter species of nuggets will be formed – it should be mentioned though, that an equal amount of nuggets would have been formed if $\theta = 0$ at the moment of the DW formation (Liang and Zhitnitsky, 2016). Only the sign of the coherent θ field before it started to oscillate dictates which nugget family is preferred to be formed.

At any point during $T \in [T_{\text{osc}}, T_{\text{crit,form}}]$ axion DWs can form (Ge et al., 2019) (and Sikivie (1982), Vilenkin and Everett (1982), for a general overview). During this time, axions get emitted because of the oscillation of the θ field under the misalignment mechanism (Abbott and Sikivie, 1983, Dine and Fischler, 1983, Preskill et al., 1983) and topological defects (Chang et al., 1998, Kawasaki et al., 2015, Fleury and Moore, 2016, Klaer and Moore, 2017, Gorghetto et al., 2018). In addition to emitting axions, the DWs acquire baryon charges at $T \in [T_{\text{osc}}, T_{\text{crit,form}}]$ from the Quark-Gluon Plasma (QGP). The reason for this charge accumulation is that a $N_{\text{DW}} = 1$ DW consists of axions, an η' field and the effective field of low-energy quarks. Additionally, it was discussed in Liang and Zhitnitsky (2016), Ge et al. (2017), Liang (2022) that a nontrivial topology in the low-energy quark field causes this baryon charge accumulation. After $T \lesssim T_{\text{crit,form}}$, the QGP turns into mesons and baryons; therefore, this stage is called QCD transition. During this phase, the axion DW itself can acquire baryon charge from two components: one is the domain wall itself with a baryon number of $N_{\text{W}} \approx \pm 2^3$ and the other one comes from changes in the θ field that is oscillating, i.e. $N_{\theta} \approx \Delta\theta$. The baryon charge on the domain wall B_{W} is directly proportional to N_{W} and can therefore have different signs for different bubbles. The baryon charge from the axion field B_{θ} depends on $\Delta\theta$, which can also have different signs but changes on larger scales. It is therefore possible to compare the total Baryon charge on the domain wall B_{W} with the background axion field baryon charge B_{θ} :

$$\delta(t) \equiv \frac{B_{\theta}}{B_{\text{W}}}, \quad (1.2)$$

which is time dependent. Following a detailed derivation in Liang (2022), one finds that the final radius R_f of a DW bubble establishes after $\sim 10^{-4}$ s. The termination of the oscillation

²<https://www.quantamagazine.org/how-axions-may-explain-times-arrow-20160107/>

³We use the convention N_{W} for baryon number on the wall, because we already defined N_{DW} to be the axion domain wall coming from different vacuum states.

and the end of the QCD transition are approximately in the same time range, but can deviate slightly. After the QCD transition the θ field changes from coherent characterization to being decoherent (it can therefore independently vary on large scales). Presented in [Liang \(2022\)](#), R_f is proportional to $\delta(t)$ with:

$$\frac{\Delta R_f}{R_f} = \frac{R_f(\mu < 0) - R_f(\mu > 0)}{R_f} = \frac{4}{3}\delta, \quad (1.3)$$

where μ is the chemical potential. From this relation it follows that depending on the sign of δ one either obtains matter AQNs (for $\delta > 0$) and antimatter AQNs (for $\delta < 0$). It is pointed out by [Liang \(2022\)](#) that antimatter AQNs have larger radii than matter AQNs. From this relation, one can infer that antimatter AQNs have a larger abundance by a factor of 0.35 than matter AQNs for $\delta \approx 0.087$ and $B_{\text{form}} \approx R_f^3$. What follows is the remarkable consequence that (under the assumption of zero baryon net-charge in the universe) one can estimate the baryon ratio relative to the visible matter via:

$$\bar{B}_{\text{AQN}} : B_{\text{AQN}} : B_{\text{visible}} \simeq 3 : 2 : 1, \quad (1.4)$$

with bars in the equation denoting the antimatter family. This naturally results in a visible-to-dark-matter ratio of $\Omega_{\text{dark}}/\Omega_{\text{visible}} \simeq 5$, as it is observed today. It is important to emphasize that this feature is a consequence of an approach overcome inconsistencies in QCD and was not initially motivated to explain the observed $\Omega_{\text{dark}}/\Omega_{\text{visible}}$ ratio.

At this stage, AQNs have been formed but are not stable yet, because the trapped baryon charges are in a hadronic state due to the excessively high temperature of the universe. Only after $T \lesssim 41$ MeV, the high surface pressure of the DW compresses trapped baryons into an extremely dense and stable state, called a Color Superconducting (CS) condensate ([Zhitnitsky, 2003](#), [Liang and Zhitnitsky, 2016](#)). AQNs in the CS phase exhibit an enormously large binding energy and hence the baryon charge is not available for the Big Bang Nucleosynthesis (BBN) at $T_{\text{BBN}} \sim 1$ MeV, where elements of metallicity $Z \leq 3$ were formed. Quark cores in the CS state are in the lowest energy state possible, and it is assumed that quarks in neutron stars obey the same state ([Alford et al., 2008](#)). It is important to note that AQNs remain in this state as it causes them to be stable over cosmic time scales ([Ge et al., 2017](#)).

In [Figure 1.1](#), a schematic sketch is presented to point out the most important formation steps of AQNs on a cosmic timescale in reference to well-studied cosmological events. Eras that do not belong to any of the colored boxes are eras proposed by established cosmological models and are taken from [Carroll and Ostlie \(2017\)](#). Others – like for instance, the ‘Grand Unification Era’ – would be in contradiction to the AQN model, but are still included in this sketch for the sake of completeness.

To ensure comprehensiveness, it is important to mention an alternative approach to explain the observed imbalance of matter over antimatter in the framework of \mathcal{CP} violation which enjoys greater acceptance in the scientific community. [Dimopoulos and Susskind \(1978\)](#) proposed that \mathcal{CP} violation might be the effect of baryogenesis. Baryogenesis, derived from the Greek words $\beta\alpha\rho\acute{\upsilon}\varsigma$ (heavy) and $\gamma\acute{\epsilon}\nu\epsilon\sigma\iota\varsigma$ (birth, origin, creation), meaning the ongoing creation and decay of baryons over cosmic evolution. Grand Unified Theories (GUTs) are required to substantiate baryogenesis, and proton decay is one of resulting consequences that GUTs predict ([Kolb and Turner, 1983](#)). Yet, an evident detection of proton decay remains to be discovered.

If the theory of AQNs on the other hand holds true, the asymmetry of matter to antimatter in the observable universe can be explained by a charge separation of baryons and antibaryons that is caused by charge accumulation in the axion DW bubbles at temperatures of $T \in [T_{\text{osc}}, T_{\text{crit,form}}]$. This theory allows an equal amount of antimatter and matter, with more antimatter being hidden in composite nuggets than the ordinary one, causing it to be unobservable. These nuggets are stable over cosmic time, as the quark core is in a dense CS

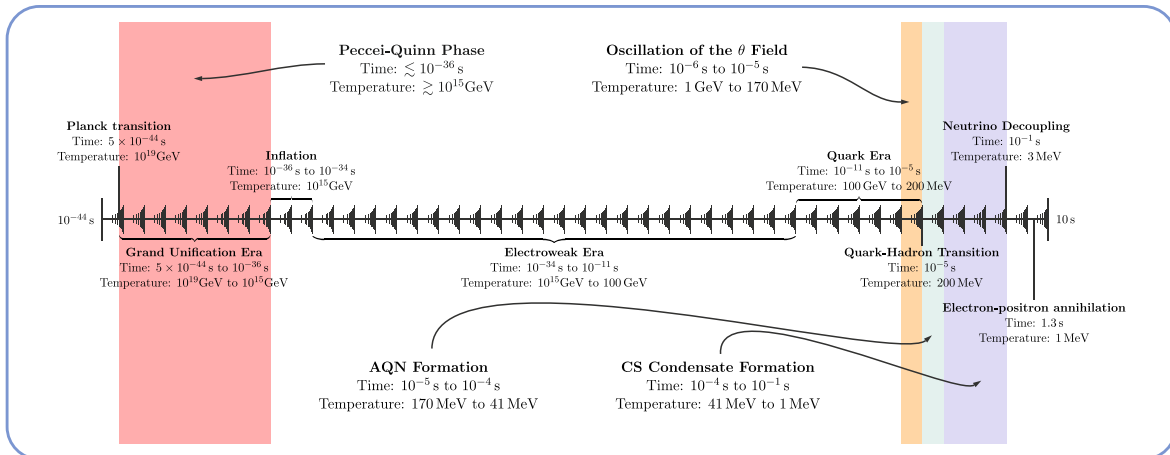


Figure 1.1: Sketch of cosmological eras in the early universe. Commonly acknowledged cosmological eras are taken from [Carroll and Ostlie \(2017\)](#). Formation eras relevant to the AQN theory are indicated by the colored boxes.

state. It serves as cold dark matter because these macroscopic particles exhibit a low number density due to individual masses of the order of $M_{\text{AQN}} \sim g$ (a more specific description will be addressed in the following section). In summary, the theory of AQNs provides many intriguing cosmological implications by explaining how the global baryon number in the universe remains zero and why the dark matter to visible matter ratio is approximately 5 since dark and visible matter share the same ancestor.

1.2 Structure of Axion Quark Nuggets and Cosmological Properties

Theory and observations, can provide boundary conditions on mass and size distribution which result in specific structures of AQNs. Furthermore, it is important to differentiate matter families as (anti-)AQN consist of a core of (anti)quarks surrounded by positrons/electrons that make the electrosphere. The electrosphere, which is surrounded by the $N_{\text{DW}} = 1$ axion DW and interactions of baryonic matter with the axion domain wall almost never occur. Fast oscillations of the $N_{\text{DW}} = 1$ axion DW exert a strong pressure on the quark core causing it to preserve in a CS state. The vacuum-ground-state energies inside and outside the nugget differ strongly compared to the outside and enable that only the external axion DW pressure suffices to prevent the AQN from decaying ([Zhitnitsky, 2023](#)). To prevent the DW to collapse further, Fermi pressure from the AQN counteracts the DW surface tension.

Parameters that describe the properties of an AQN are the baryon number B , the electric charge eQ , where Q typically corresponds to the number of positrons that depleted from an originally neutral AQN and in some scenarios the magnetization M ([VanDevender et al., 2017, 2020b](#)), which will be neglected in this study for reasons of simplification. It will be shown in later sections that Q highly depends on the temperature of the surrounding gas as positrons can deplete if the conditions suffice. Upper limits on B can be observationally constrained e.g. by non-detections from IceCube with $\langle B \rangle > 3 \times 10^{24}$ ([Lawson et al., 2019, Zhitnitsky, 2022a](#)). B results in the AQN's mass M_{AQN} and size R_{AQN} , with most recent detailed predictions on their distribution in [Ge et al. \(2019\)](#) and refined in ([Majidi et al., in prep.](#)). Since mass contributions from the electrosphere and the DW can be neglected, the baryonic mass component of an AQN can be estimated as follows:

$$M_{\text{AQN}} \approx m_p B \simeq 16.7 \left(\frac{B}{10^{25}} \right) \text{ g.} \quad (1.5)$$

In the state of a CS phase, one can assume the nuclear density to be $\rho_n = 3.5 \times 10^{14} \text{ g cm}^{-3}$ (Zhitnitsky, 2018) resulting in an AQN radius of:

$$R_{\text{AQN}} = \left(\frac{3M_{\text{AQN}}}{4\pi\rho_n} \right)^{1/3} \approx 2.25 \times 10^{-5} \text{ cm} \quad (1.6)$$

In a non-relativistic Boltzmann regime, McNeil Forbes and Zhitnitsky (2008b) found that the radial number density of positrons follows:

$$n(z) \simeq \frac{T_{\text{AQN}}}{2\pi\alpha} \left(\frac{1}{z + \bar{z}} \right)^2. \quad (1.7)$$

It is important to keep the unit conversion in mind. T_{AQN} in Equation 1.7 is in units of cm^{-1} , and α is the fine-structure constant, and z is the radial distance relative to the quark core (see Appendix D for unit conversions). At a specific distance above the quark core surface, a beta equilibrium will be established, which is where beta decay and electron capture balance out. \bar{z} is then defined to be the distance where positrons from the electrosphere reach a chemical potential of $\mu_{e^+} \simeq 10 \text{ MeV}$ while the beta equilibrium will be maintained (McNeil Forbes and Zhitnitsky, 2008b). We obtain:

$$\bar{z} = \frac{1}{\sqrt{2\pi\alpha}m_e \left(\frac{T_{\text{AQN}}}{m_e} \right)^{1/4}}. \quad (1.8)$$

It is important to consistently use proper unit conversion in Equation 1.8, too. Therefore, following Appendix D, m_e has to be converted into units of cm^{-1} (for an AQN with $T_{\text{AQN}} = 1 \text{ eV}$, one obtains for example $\bar{z} \approx 1.24 \times 10^{-9} \text{ cm}$). When choosing $z = 0$, it is not necessarily the spacial zero-position to the quark surface, but rather the onset of the Boltzmann regime, where the positrons are not too close to the surface anymore. For increasing T_{AQN} , less positrons are located directly at the quark surface and therefore $n(z)$ increments, too.

Ionized AQNs are characterized by a charge Q , and we will provide a more detailed expression for Q in Subsection 2.1.1. Positrons in the electrosphere are loosely bound due to their thermal motion, which rises with the internal AQNs temperature. One can define a T_{AQN} dependent region, where positron evaporation causes a certain net-charge Q to the AQN system that we call r_\star . A rough estimate for r_\star can be conducted by following Forbes et al. (2010) and Flambaum and Zhitnitsky (2019):

$$r_\star \sim \frac{\alpha Q}{T_{\text{AQN}}}. \quad (1.9)$$

Q depends on T_{AQN} and for a rough estimate we can assume $Q(T_{\text{AQN}} = 1 \text{ eV}) \simeq 1.46 \times 10^6$ and $Q(T_{\text{AQN}} = 10^{-2} \text{ eV}) \simeq 4.62 \times 10^3$, resulting in $r_\star(T_{\text{AQN}} = 1 \text{ eV}) \simeq 5.4 \times 10^{-2} \text{ cm}$ and $r_\star(T_{\text{AQN}} = 10^{-2} \text{ eV}) \simeq 1.71 \times 10^{-2} \text{ cm}$ following Appendix D. In the case of these numerical examples, this means that (for an AQN of temperature $T_{\text{AQN}} = 1 \text{ eV}$) 1.46×10^6 positrons have already left the system, resulting in a negative net-charge proportional to the number of evaporated positrons. Later in this study, we will find a similar argument as in Equation 1.9 that can be used to determine a radius depending on the environmental gas temperature where gas particles are slow enough to be captured by an AQN with a charge Q . Figure 1.2 shows the radial number density of positrons around an antiquark core from $z = 0$ to $r_\star = 5.4 \times 10^{-2} \text{ cm}$.

One can calculate the number of positrons below r_\star by integrating the positron number density $n(z)$ over a spheric shell in a range of $z \in [0, r_\star] \text{ cm}$. The total positron number is therefore:

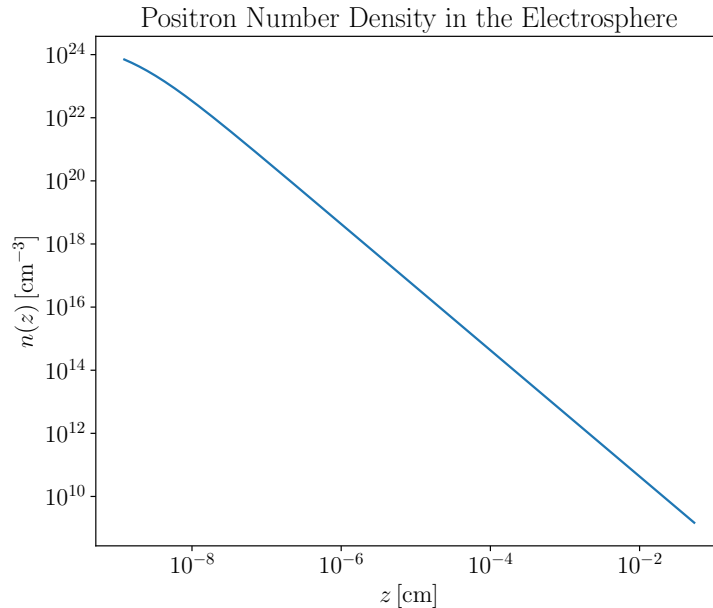


Figure 1.2: Radial number density $n(z)$ in the range of $z \in [1.24 \times 10^{-9}, r_*$] cm for an AQN at $T_{\text{AQN}} = 1$ eV.

$$N_{e^+} = \int_0^{r_*} dz \int_0^\pi d\vartheta \int_0^{2\pi} d\varphi n(z) z^2 \sin \vartheta \quad (1.10)$$

$$= \frac{2T_{\text{AQN}}}{\alpha} \left[z - \frac{\bar{z}^2}{\bar{z} + z} - 2\bar{z} \ln(\bar{z} + z) \right]_0^{r_*} \quad (1.11)$$

$$\approx 2.92 \times 10^6 \quad (1.12)$$

It can be seen in Equation 1.10 that $N_{e^+} = 2Q$. These N_{e^+} positrons try to compensate negative charges from the antiquark core with $N_{\bar{q}} = 3Q$, such that a net-charge of the full system of eQ is obtained at r_* . This means that at r_* , Q positrons have already left the system. The exact number of Q at a certain radius depends on T_{AQN} and in general, when $T_{\text{AQN}} \rightarrow 0$ we naturally obtain $Q \rightarrow 0$ and furthermore $N_{e^+} \rightarrow 0$, because less positrons will be in thermal motion and start to segregate at the surface for low internal AQN temperatures. It is important to note that $N_{e^+} \ll B$ with $\langle B \rangle \gtrsim 3 \times 10^{24}$ (Lawson et al., 2019), because we only considered positrons in the non-relativistic Boltzmann regime since $z = 0$ is not the physical quark core surface. Non-thermal positrons that contribute towards a neutral charge of an AQN are mostly located at a region closer to the surface, i.e. below $z = 0$. Only thermal positrons can contribute to the ionization state of an AQN once their thermal velocity suffices to escape the system. It becomes apparent that AQN mass contribution from the electrosphere becomes negligible when considering $M_{\text{tot},e^+} = m_e N_{e^+} \approx 2.66 \times 10^{-21}$ g.

The axion DW comprises 1/3 of the total mass of an AQN and extents much further than the nugget core with an DW radius roughly estimated to $R_{\text{DW}} \sim m_a^{-1} \sim \text{cm}$ (Liang, 2022). Liang (2022) furthermore described the DW with a thickness of $\sim 10^{-1}$ cm. In Figure 1.3, a not true-to-scale schematic slice of the structure of an AQN is visualized in order to show the different layers of an AQN at different scales.

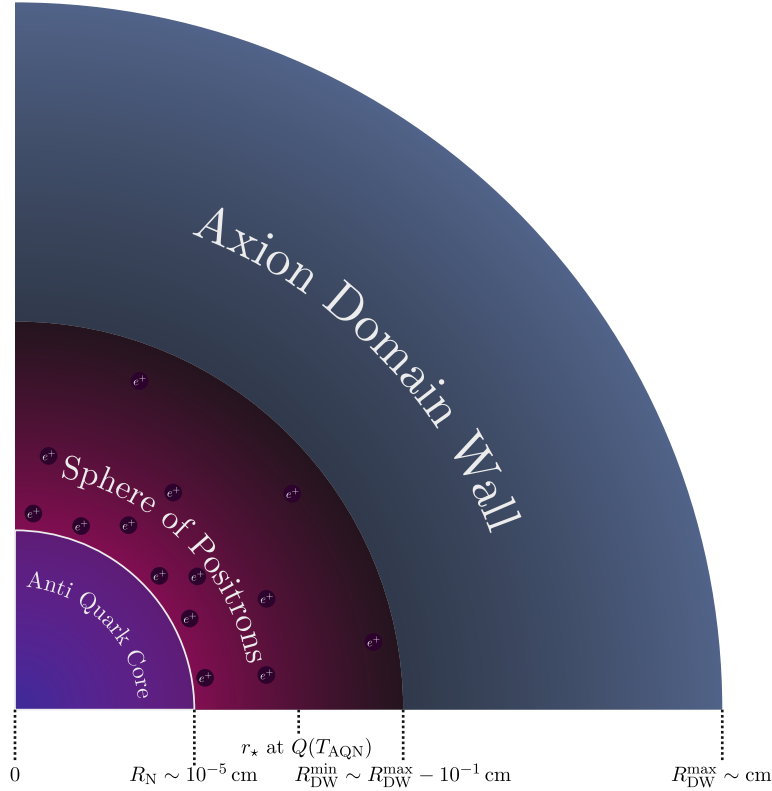


Figure 1.3: Schematic slice of an AQN (not true-to-scale).

1.3 Possible Interaction Scenarios

Throughout this thesis, B , M_{AQN} and R_{AQN} will be fixed to the previously estimated values of:

B	M_{AQN}	R_{AQN}
10^{25}	16.7 g	2.25×10^{-5} cm

Table 1.1: AQN parameters that were utilized for the numerical analysis throughout this thesis.

A distribution function of these parameters is not well-constrained yet and would drastically increase the complexity of the system. With the fixed parameters describing a single AQN, one can infer the anti-AQN's number density by assuming the mass ratio relation from Equation 1.4. According to the mass ratio relation, a fraction of $3/5$ of the entire dark matter accounts for anti-AQNs. Since ionized gas in the ICM mainly consists of normal matter, the highest rate of annihilation processes – and hence visible interactions – will be expected from anti-AQNs. A third of the total AQN mass comes from the $N_{\text{DW}} = 1$ axion domain wall (Liang, 2022). Therefore – in order to account for the AQN number density n_{AQN} from the total ‘observable’ dark matter density ρ_{DM} – we would have to multiply a factor of $2/3$ by the DM-AQN ratio. We therefore obtain an AQN number density estimate of:

$$n_{\text{AQN}} = \frac{2}{3} \times \frac{3}{5} \times \frac{\rho_{\text{DM}}}{M_{\text{AQN}}}, \quad (1.13)$$

which typically scales in a galaxy cluster environment as $n_{\text{AQN}} \sim 10^{-29} \text{ cm}^{-3}$. It is because of the low number density that AQNs mostly preserve cold dark matter features – provided they are in a suitable environment, however, the occurring interactions can even yield different emission processes of AQNs. In the following, different interaction scenarios are listed:

- ① **Antimatter AQN interaction with electrons:** Electrons can interact with the electrosphere made up of positrons for antimatter AQNs. A direct emission line of 511 keV from e^+e^- annihilation can be expected (Oaknin and Zhitnitsky, 2005).
- ② **Antimatter AQN interaction with protons:** Free protons propagating through the electrosphere can collide with the antiquark core. Depending on the relative velocity of protons to AQNs and the collision angle, protons can either penetrate deeply into the core or stop close below the antiquark surface. If a proton annihilates with an antiquark in central regions of the core, quark-antiquark ($q\bar{q}$) annihilation can take place and a total reservoir of 2 GeV can be transferred to the AQN's interior via radiation that thermalizes the core. This heating process leads to thermal emission of the quark core in the form of blackbody radiation. If the proton annihilates close to the surface, non-thermal emission from the 2 GeV reservoir can immediately escape the system.
- ③ **Antimatter AQN annihilation with celestial bodies:** As it is discussed in detail by Liang (2022), antimatter AQNs can annihilate with more matter at the same time. When AQNs lose potential energy by the loss of mass from the core due to annihilation processes, axions residing off-shell in the domain wall can be emitted, as they are not in equilibrium anymore. In order to retain a minimum total energy of the system and therefore maintain stability of the AQN, axions will be emitted to lower the DW's mass.
- ④ **Matter AQN interaction with antimatter:** Technically, one could expect the same emission processes from ① and ② with matter AQNs with positrons and antiprotons. However, because of the low abundance of antimatter cosmic rays (e.g. (Hillas, 2006, Blum et al., 2017)) and the slightly lower abundance of matter AQNs over antimatter AQNs, it is expected that matter AQNs remain dark for most of the time and electromagnetic signals originating from matter AQNs can be neglected.
- ⑤ **Matter AQN-Antimatter AQN interaction:** Even though the electromagnetic outcome of matter-antimatter AQN interactions would result in an impressive electromagnetic signature, it is because of the low number density of $n_{\text{AQN}} \sim 10^{-29} \text{ cm}^{-3}$ that this interaction scenario can be entirely neglected (see comments on this for example in Zhitnitsky (2022a)). And in spite of the fact that both of the AQNs can have an attractive influence on each other if ionized, the higher effective cross-section would not drastically increase interaction rates.
- ⑥ **AQN-AQN interaction from same particle family:** Since AQNs from the same particle family would only collide by chance with no interaction enhancement by their ionization state, collisions are expected to be even rarer than in ④. An electromagnetic signature would at most be visible by thermalization of a heated AQN after collision.

As we will assume the ICM to consist of ionized hydrogen, this work will only focus on emission phenomena coming from proton-antimatter AQN interactions. Line emission from e^+e^- annihilation, axion emission by strong AQN emission and AQN-AQN self-interactions will be neglected in this study as thermal and non-thermal AQN emission from proton interactions is presumed to dominate the spectrum.

1.4 Observation Proposals and Mysterious Detections

In the following a few observational phenomena are listed that cannot be explained by conventional theories and propose the possibility to be attributed to direct outcomes of AQN signatures:

21 cm absorption line: Observations from the Experiment to Detect the Global EoR Signal (EDGES) (Feng and Holder, 2018) show strong absorption lines in the 21 cm signal. These detections might propose the possibility for a stronger than expected radio background at redshift $z > 12$. This study proposes that if only 0.1% of the today's radio background radiation would be present at early times a signal at a frequency of 90 MHz can be seen for 10% of the today's radio background at early times, a very large effect on the 21 cm signal can be expected. (Lawson and Zhitnitsky, 2019) have shown that 1% of AQN radiation from $z \sim 17$ is capable of explaining the findings from Feng and Holder (2018).

Diffuse UV Radiation: The diffuse ultraviolet background radiation was studied by Henry et al. (2015) in which he suggested that not only scattered star-light contributes to the background emission in ultraviolet frequencies. Based on data from the Galaxy Evolution Explorer (GALEX) (Martin et al., 2005), they proposed that a more exotic origin might additionally constitute to this background emission as simple dust scattering models cannot fully explain this excess. The authors further introduce the concept of an additional exotic component to be of galactic nature and suggest the exotic component to originate from dark matter. While exploring different dark matter models, Henry et al. (2015) could not find a reasonable mechanism to explain the shelf-like excess in a band-pass of $\nu \in [1350, 2800] \text{ \AA} \sim [4.4, 9.2] \text{ eV}$. According to Zhitnitsky (2022b), hot AQNs with a temperature of $T_{\text{AQN}} \sim 5 \text{ eV}$ are a possible source for this wide-band background emission. AQNs are indeed suitable candidates, as they naturally show a relative broad spectral emission feature.

511 keV line: Analysis from the spectrometer SPI on the INTEGRAL gamma-ray observatory, conducted by Knödlseeder et al. (2003) resulted in a constraint on the morphology of a 511 keV line emission coming from the galactic center. This study constrained the geometry of the bulge by this emission feature and provide estimates on the e^+e^- annihilation rate for a distance of 8.5 kpc to amount up to $(3.4 - 6.3) \times 10^{42} \text{ s}^{-1}$ with a flux of $9.9_{-2.1}^{+4.7} \times 10^{-4} \text{ photons cm}^{-2} \text{ s}^{-1}$. Oaknin and Zhitnitsky (2005) estimate AQNs to constitute to this line with a flux of $10^{-3}(10^{33}/B)^{1/3} \text{ photons cm}^{-2} \text{ s}^{-1}$ with the baryon charge B .⁴ However, they claim that they would expect a narrower distribution of 511 keV photons by assuming a galactic dark matter density profile of $\rho_{\text{DM}} \sim r^{-\gamma}$ with $\gamma \in [0.4, 0.8]$. In addition, estimates by Oaknin and Zhitnitsky (2005) are strongly model-dependent. Follow-up studies found that the 511 keV line must be narrow and is likely produced by the annihilation of positroniums (Jean et al., 2006, Weidenspointner et al., 2006). Zhitnitsky (2007) found that the mechanism of positronium annihilation would be feasible by the AQN model and estimated a similar line width as proposed by (Jean et al., 2006, Weidenspointner et al., 2006). More details on the 511 keV line in the AQN framework were additionally provided by (Forbes et al., 2010). Flambaum and Samsonov (2021) discard the idea of electrons annihilating in the positron cloud being able to explain the SPI/INTEGRAL observations and propose that more sophisticated proton-antiquark annihilations might provide a more suitable mechanism.

Chandra's diffuse $k_B T \approx 8 \text{ keV}$ emission: After subtraction of known X-ray sources, Chandra measurements from the galactic center show a diffuse emission that would correspond to a $k_B T \approx 8 \text{ keV}$ plasma (Muno et al., 2004). Explanations of this study ruled out radiating sources of $\geq 10^{31} \text{ erg s}^{-1}$ to be attributed to this diffuse emission and that sources either must be fainter or that heating mechanisms of the ISM are not sufficiently understood yet. McNeil Forbes and Zhitnitsky (2008a) predict that this diffuse X-ray emission can be attributed to the non-thermal emission of AQNs produced by interactions of protons with the anti-quark core of an AQN.

Comptol gamma ray photons in a 1 – 20 MeV energy range: Analyzed by Strong

⁴In fact, Oaknin and Zhitnitsky (2005) additionally proposed a flux that scales with $(10^{18}/B)^{1/3}$. However, since lower bound non-detection constraints require $\langle B \rangle \gtrsim 3 \times 10^{24}$ (Lawson et al., 2019), a baryon charge of 10^{18} can be discarded for AQNs. The other flux estimated by Oaknin and Zhitnitsky (2005) desires B to be 8 magnitudes larger than in Equation 1.5. As only lower bound non-detection constraints exist, $B \sim 10^{33}$ is a valid assumption.

et al. (2000), their model for diffuse galactic gamma rays struggles to explain an excess of photons in a range of 1 – 20 MeV observed by COMPTEL. Alongside by the 511 keV line, a high energetic emission of photons in a broader range of 1 – 20 MeV accompanied by the same mechanism. Lawson and Zhitnitsky (2008) attribute these processes to e^+e^- annihilations in the electrosphere, while Flambaum and Samsonov (2021) argue that the electric field of the AQN is responsible for a strong suppression in electron-positron interactions as anti-AQNs exhibit a repelling characteristic to negatively charged particles. Protons annihilating with antiquarks from the nugget core might be able to reproduce gamma ray photons as a trapped proton reduced the net electric charge, and positrons can deplete by an increase of internal AQN temperature and in order to maintain electric neutrality. The evaporated positrons are then free to interact with surrounding free electrons from the ISM.

Diffuse microwave excess: Thermalization of AQNs after proton-antiquark annihilation in the core is expected to be the source of low energy photons that are e.g. observed from the core of the Milky Way. McNeil Forbes and Zhitnitsky (2008b) suggest that this thermal AQN radiation can explain the observations that were discussed by Finkbeiner (2004a,b), Finkbeiner et al. (2004), Hooper et al. (2008), Dobler and Finkbeiner (2008) that pose a difficulty to attribute known physical sources to observations by the Wilkinson Microwave Anisotropy Probe (WMAP). The thermal AQN emission would be capable to contribute to a wide spectral range originating from annihilation-heated AQNs.

Solar corona, EUV and X-ray photons: Observations in extreme ultraviolet (EUV) and soft X-rays have been discussed in context with coronal heating by Testa et al. (2015). Additional contributions of coronal heating might be possible by nanoflares resulting from AQNs that collide with the sun. If such an event occurs, AQNs can fully annihilate and result in $L_{\text{AQN}} \simeq 4.8 \times 10^{27} \text{ erg s}^{-1}$ (Zhitnitsky, 2017). Large solar flares that are anticipated to be caused by magnetic reconnection events triggered by shock waves, which in return are established by supersonic AQNs in the solar atmosphere (Zhitnitsky, 2018). Further, detailed studies on explaining nanoflares via AQN annihilation in connection with coronal heating were presented in Raza et al. (2018) while occasional radio emission events were pointed out in Ge et al. (2020) detected by Mondal et al. (2020). Because multiband detections originate from the same event, transient radio signals must cross-correlate with EUV photons. Radio emissions are attributed to plasma instability that develop under the injection of electrons with a non-thermal, high energy component (Thejappa, 1991). Ge et al. (2020) argue that non-thermal electrons can be produced at the onset of annihilation once AQNs enter the solar corona.

Fast radio bursts: Since Fast Radio Bursts (FRBs) are typically not recurring events and there whereabouts have to be predicted, when and where one could expect a new event, these transients are still challenging to understand within our today’s physical understanding. It is believed that magnetars are very likely to host FRBs near the surface due to magnetic reconnection, as strong magnetic fields of the order of $\sim 10^{14} \text{ G}$ can be reached (see for example Kumar et al. (2017) and Lu and Kumar (2018)). An explanation for triggering magnetic reconnection events was provided by Van Waerbeke and Zhitnitsky (2019) utilizing the AQN model. A mechanism that initiates such cataclysmic events can be provided by AQNs that cause shock waves in the vicinity of the magnetar’s surface due to their high relative velocity. According to the author, these shock waves are responsible for triggering magnetic reconnection of preexisting magnetic fluxes. A process driving magnetic reconnection by shock waves was motivated by Tanuma et al. (2001) in a different physical environment.

Primordial lithium puzzle: A mystery addressing a long-lived cosmological problem is the primordial lithium puzzle, where fewer elements with metallicity of $Z \geq 3$ than expected were formed in the early universe. It was already mentioned in Section 1.1 that the quark core of AQNs will occupy very dense phases in a CS state that makes them passive in interactions and confers them the feature as a ‘dark matter’ particle. A far-reaching consequence is that

during the BBN, a strong suppression of $Z \geq 3$ elements is abundant. (Flambaum and Zhitnitsky, 2019) propose that the charge of elements with higher metallicity than helium itself has a strong impact on the cosmological abundance of heavier elements too. Elements with a charge $Z > 2$ are proposed to be captured by anti-AQNs and subsequently annihilated. Additionally, Flambaum and Zhitnitsky (2019) argue that helium and hydrogen nuclei are not affected by annihilation as strongly as heavier ones. The suppression factor for the synthesis of elements with $Z \geq 3$ comes from a similar expression as displayed in Equation 1.9, with the only difference being T_{gas} instead of T_{AQN} . This defines a radius where ionized AQNs are capable of capturing gas particles that do not exceed a thermal velocity, i.e. $\alpha Q > m_p v_p^2/2$ with the proton mass m_p . It is because of this capture radius that ions from lithium and beryllium are strongly attracted and subsequently annihilated by anti-AQNs.

Skyquarks: Budker et al. (2022) discuss the consequences of AQNs hitting the earth and point out that a series of events could accompany these collisions. According to this study, infrasound, acoustic and seismic waves can directly be attributed to AQN-earth encounters.

Seasonal X-ray variations: Seasonal variations in the X-ray background detected by XMM-Newton in the energy range of 2 – 6 keV were concluded by Fraser et al. (2014). Ge et al. (2022) propose that the AQN can explain these observations using the motion of the solar system around the galactic center. They claim that – as the sun passes through an approximately circular orbit – it would experience a relative constant dark matter wind of $v_{\text{DM}} \simeq 220 \text{ km s}^{-1}$. The motion of the earth would therefore experience season-dependent variations of the dark matter wind due to relative changes in the direction of the motion during one year. It has to be considered that directional dark matter wind influencing the sun and also being of the same orbital velocity of the sun around the galactic center is a strong assumption, as it presumes dark matter particles to be static with respect to the galactic rotation.

According to a study conducted by Lacroix et al. (2020), halo particles show to follow a rather isotropic motion. They used a cosmological zoom-in simulation and analyzed the halos of spiral galaxies. In Figure 6 of their study, one can see e.g. that, at a radial distance where the sun in the Milky Way is anticipated to be located of $r \sim 8 \text{ kpc}$, $\beta(r \leq 10 \text{ kpc})$ is relatively close to 0, which implies the motion of the halo to be isotropic. In addition, it is shown in Figure 11 (Lacroix et al., 2020) that in a radial distance bin of $r \in [7, 9] \text{ kpc}$ the velocity distribution of halo particles has a width of multiple $\sim 10^2 \text{ km s}^{-1}$. Changes in the distribution of AQN velocities would therefore intuitively be larger than seasonal dependent changes due to earth’s motion which is proposed to be of the order $\Delta v_{\text{earth}} = \cos(60^\circ) \times v_{\text{earth}} = 15 \text{ km s}^{-1}$ (Ge et al., 2022).

Multi-modal events detected by Horizon-T: Multi-Modal Events (MMEs), i.e. detections of particle showers with different energies in close succession were detected by the Horizon-T experiment (Beznosko et al., 2020). Zhitnitsky (2021b) argue that these MMEs can be explained in the AQN framework and the result of the AQN annihilation events must be distinct from the conventional cosmic ray air showers.

Exotic events by the Pierre Auger Observatory: Cosmic ray-like events related to thunderstorms were observed by the Pierre Auger Observatory (Colalillo, 2019). AQNs can induce lightning strikes and subsequent direct emission from AQNs as proposed by Zhitnitsky (2022a).

Shower-like events detected by the Telescope Array: Short time bursts were detected by the Telescope Array (TA) and documented in Abbasi et al. (2017) and Okuda (2019). AQN annihilations might resolve the mysteries regarding these observations (Zhitnitsky, 2021a, Liang and Zhitnitsky, 2022a).

Unexplained events by ANtarctic Impulse Transient Antenna: Observations by ANtarctic Impulse Transient Antenna (ANITA) propose the detection of anomalous events (Gorham et al., 2016, 2018, 2021). Non-inverted polarity is a feature that was observed for

two events that cannot be explained by conventional cosmic ray events. It was proposed by Liang and Zhitnitsky (2022b) that non-inverted polarity might be a feature that can be reproduced by AQNs.

3.57 keV excess in the spectra of galaxy clusters: As a final remark of this Section, a intriguing spectral feature in the X-ray regime of galaxy clusters was inferred by (Bulbul et al., 2014). They found an emission line in the stacked X-ray spectra of 73 galaxy clusters at $E = (3.55 - 3.57) \pm 0.03$ keV. While a decay line by sterile neutrinos was discussed amongst other possible sources for this excess, other dark matter candidates were not addressed. We would like to point out that it will come clear in the following sections that an excess in the high energy regime in the spectra of galaxy clusters produced by non-thermal AQN emission is not absurd. A cascade of discussions addressing alternative dark matter models regarding the findings from Bulbul et al. (2014) were published (see for example Bashkanov and Watts (2020), Kuksa and Beylin (2020), Belfatto et al. (2022), Nielsen and Froggatt (2023)). These studies refer to dark matter models that include quarks to some extent, with the dusty dark matter model by Nielsen and Froggatt (2023) coming close to the AQN model. However, none of these and other studies appearing in the citation list⁵ studied AQNs with regards to the 3.57 keV emission line discovered by Bulbul et al. (2014), and we will discuss the results of this work with respect to their findings as we focus on galaxy cluster emission in a full spectrum in a range of $\nu \in [10^{-8}, 10^8]/(2\pi)$ eV. Gonzalez Villalba (2024), on the other hand, point out that observed excesses can be of non-physical origin due to calibration issues. Calibration routines have to account for individual features in the effective areas in the 3 – 4 keV regime, and (if the signal-to-noise ratio is too high) unidentified line features can appear.

⁵See on the Astrophysics Data System (ADS): <https://ui.adsabs.harvard.edu/abs/2014ApJ...789...13B/citations>

Chapter 2

Methodology

2.1 Physical Description of AQNs

2.1.1 Internal AQN Temperatures Through Ambient Gas Interactions

Internal temperature of AQNs are influenced by annihilation processes of protons penetrating through a nugget with anti-quarks from the inner core. The internal temperature of a nugget can be estimated from the conservation of energy. More precisely, if a proton will be captured by an AQN, the injected energy must equal the radiative output. Protons can be captured more efficiently if the anti-quark nugget is ionized, but loses efficiency under certain conditions of the environment – we therefore have to introduce an effective cross-section σ_{eff} to model collision rates. The energy conversion efficiency during a collision depends on a proxy for the probability of quantum reflection for neutral gas called f , and the key contribution of photon production $g \simeq 0.1$. Because of the increased Coulomb potential in an ionized gas, the quantum reflection probability $\mathcal{P} = (1 - f)$ is highly suppressed, and we therefore obtain $f \sim 1$. The Coulomb potential causes the hydrogen ion to be trapped around an AQN until the final collision and therefore annihilation occurs. The injected energy per unit time can be estimated by:

$$\frac{dE}{dt} = \frac{\sigma_{\text{eff}}}{V} N_{\text{gas}} \Delta E \Delta v \quad (2.1)$$

$$= \sigma_{\text{eff}} n_{\text{gas}} \Delta E \Delta v. \quad (2.2)$$

ΔE is the energy which will be released by an annihilation event of a single proton amounting up to $\Delta E \sim 2m_p c^2 \approx 2 \text{ GeV}$ and $\Delta v = |v_{\text{AQN}} - v_{\text{gas}}|$ is the relative AQN-proton velocity. The radiative output is the luminosity of a nugget with radius R_{AQN} , i.e.:

$$L = 4\pi R_{\text{AQN}}^2 F \quad (2.3)$$

If we set $dE/dt = L$ and after reexpressing the effective cross-section $\sigma_{\text{eff}} = \kappa\pi R_{\text{AQN}}^2$ using the scaling parameter κ , we obtain the expression:

$$F = 2 \text{ GeV} \frac{\kappa}{4} n_{\text{gas}} \Delta v (1 - g) f \quad (2.4)$$

As a consequence of the internal temperature increase due to the annihilation process, the positrons in the electrosphere will be accelerated and emit Bremsstrahlung. In natural units, i.e. $c = \hbar = 1$ and $h = 2\pi$, the total surface emissivity of an AQN is calculated by [McNeil Forbes and Zhitnitsky \(2008b\)](#) and is given by:

$$F \approx \frac{16\alpha^{5/2}}{3\pi} T_{\text{AQN}}^4 \left(\frac{T_{\text{AQN}}}{m_e} \right)^{1/4}. \quad (2.5)$$

α is the fine-structure constant and T_{AQN} is the internal temperature of the AQN. After equating Equation 2.4 with Equation 2.5, one can solve for T_{AQN} and obtains:

$$T_{\text{AQN}} = \left(\frac{3\pi m_e^{1/4}}{32\alpha^{5/2}} \text{GeV} n_{\text{gas}} \Delta v (1-g) f \kappa \right)^{4/17}. \quad (2.6)$$

Equation 2.6 can be represented in a more intuitive way if we use scaling parameters of $n_{\text{gas}} \sim \text{cm}^{-3}$ and $\Delta v \sim 10^{-3}c$. It shall be noted that in galaxy cluster environments the number density of gas scales with $n_{\text{gas, cluster}} \sim 10^{-3} \text{cm}^{-3}$. However, we will use the higher density scaling parameter in order to maintain consistency with the results from the underlying literature. Utilizing the numerical conversion values displayed in Appendix D, we obtain:

$$T_{\text{AQN}} \sim \beta^{4/17} \text{eV} \left(\frac{n_{\text{gas}}}{\text{cm}^{-3}} \right)^{4/17} \left(\frac{\Delta v}{10^{-3}c} \right)^{4/17} \left(\frac{(1-g)f}{0.9} \right)^{4/17} \kappa^{4/17}, \quad (2.7)$$

with $\beta = 0.011963$. The numerical factor κ boosts the internal AQN temperature if the effective cross-section is larger than its geometrical cross-section. We therefore use the following condition for each AQN:

$$\kappa = \begin{cases} \left(\frac{R_{\text{eff}}}{R_{\text{AQN}}} \right)^2, & R_{\text{eff}} > R_{\text{AQN}} \\ 1, & R_{\text{eff}} \leq R_{\text{AQN}} \end{cases} \quad (2.8)$$

In order to find an expression for R_{eff} , two important contributions have to be taken into account. First, the charge of an AQN Q , which is a proxy for the ionization stage, and second, the temperature of the surrounding plasma. In galaxy clusters, the ICM consists of highly ionized gas with temperatures of $T_{\text{ICM}} \sim \text{keV}$. In an entirely ionized gas, Zhitnitsky (2023) shows that cross-section of AQNs can scale with R_{eff} instead of R_{AQN} , leading to a potential increase in the collision efficiency with the surrounding gas. It is important to note that geometrical radii of AQNs are of the order of $R_{\text{AQN}} \sim 10 \mu\text{m}$ and – given that the gas number density in galaxy clusters is of the order of $n_{\text{gas}} \sim 10^{-3} \text{cm}^{-3}$ – collision rates with surrounding particles can be quite low if $R_{\text{eff}} < R_{\text{AQN}}$. It is possible to derive R_{eff} from physical properties of the nugget and its environment.

In the following Zhitnitsky (2023) proposes that the potential energy of attraction for AQNs in an ionized gas scales with the thermal energy of the plasma in the environment, i.e.:

$$\frac{\alpha Q}{R_{\text{cap}}} \sim \frac{m_p v_p^2}{2} \sim T_{\text{gas}}, \quad (2.9)$$

with the fine-structure constant α , the charge Q , the proton mass m_p and proton velocity v_p . It is striking that Equation 2.9 differs from Equation 1.9, as r_* labels the radius at which an AQN is ionized by a factor of Q , which only depends on its internal temperature. Equation 2.9, on the other hand, shows at which radius an ionized AQN is able to capture protons from the gas with thermal velocities of $T_{\text{gas}} \sim m_p v_p^2$. What follows from this scaling relation is a capture radius which decreases for increasing gas temperatures. Zhitnitsky (2023) used the capture radius instead of the effective radius with $R_{\text{cap}} = \sqrt{\pi} R_{\text{eff}}$. In this thesis, however, we will adapt the convention of using R_{eff} instead of R_{cap} . After reexpressing Equation 2.9, we obtain the following relation:

$$R_{\text{eff}} = \frac{\alpha Q}{T_{\text{gas}} \sqrt{\pi}} \quad (2.10)$$

It is important to note that Q is in fact a function of T_{AQN} . The higher T_{AQN} , the higher the thermal motion of positrons in the electrosphere with positrons following a non-relativistic Boltzmann regime (McNeil Forbes and Zhitnitsky, 2008b). If kinetic positron

energies exceed the potential energy of the AQN, it is possible for positrons to deplete, leading to a negative charge for anti-AQNs. The positrons are rather weakly bound and the number of positrons Q which are likely to evaporate from the AQN can be estimated by using the mean field approximation (McNeil Forbes and Zhitnitsky, 2008b) of the local density of positrons $n(z, T_{\text{AQN}})$ at a distance z from the surface of an AQN. Following Zhitnitsky (2023), we obtain:

$$Q \approx 4\pi R_{\text{AQN}}^2 \int_0^\infty n(z, T_{\text{AQN}}) dz \sim \frac{4\pi R_{\text{AQN}}^2}{\sqrt{2\pi\alpha}} (m_e T_{\text{AQN}}) \left(\frac{T_{\text{AQN}}}{m_e}\right)^{1/4} \quad (2.11)$$

For reasons of consistency, m_e and units of cm from Equation 2.11 will be reexpressed in units of eV using natural units (i.e. $c = \hbar = 1$ and $h = 2\pi$). Unit conversions into eV are displayed in Appendix D. We thereby obtain:

$$Q \simeq 1.46 \times 10^6 \left(\frac{T_{\text{AQN}}}{\text{eV}}\right)^{5/4} \left(\frac{R}{2.25 \cdot 10^{-5} \text{ cm}}\right)^2 \quad (2.12)$$

Now, we can insert Equation 2.12 into Equation 2.10 and find:

$$R_{\text{eff}} = \frac{21.03}{\sqrt{\pi}} \times 10^{-2} \text{ cm} \left(\frac{1 \text{ eV}}{T_{\text{gas}}}\right) \left(\frac{T_{\text{AQN}}}{1 \text{ eV}}\right)^{5/4} \left(\frac{R}{2.25 \cdot 10^{-5} \text{ cm}}\right)^2 \quad (2.13)$$

Now, it is possible to insert Equation 2.6 into Equation 2.13 and use $\kappa = (R_{\text{eff}}/R_{\text{AQN}})^2$ to solve for R_{eff} . We then obtain:

$$R_{\text{eff}} \simeq 1043.64 \text{ cm} \left(\frac{n_{\text{gas}}}{\text{cm}^{-3}}\right)^{5/7} \left(\frac{\Delta v}{10^{-3} c}\right)^{5/7} \left(\frac{R}{2.25 \cdot 10^{-5} \text{ cm}}\right)^{24/7} \left(\frac{1 \text{ eV}}{T_{\text{gas}}}\right)^{17/7}. \quad (2.14)$$

κ in the case of $R_{\text{eff}} > R_{\text{AQN}}$ can then be reexpressed as:

$$\kappa \sim \left(\frac{1043.64 \text{ cm}}{2.25 \cdot 10^{-5} \text{ cm}}\right)^2 \left(\frac{n_{\text{gas}}}{\text{cm}^{-3}}\right)^{10/7} \left(\frac{\Delta v}{10^{-3} c}\right)^{10/7} \left(\frac{R}{2.25 \cdot 10^{-5} \text{ cm}}\right)^{34/7} \left(\frac{1 \text{ eV}}{T_{\text{gas}}}\right)^{34/7}. \quad (2.15)$$

It is thereby possible to insert Equation 2.15 in Equation 2.7 to find:

$$T_{\text{AQN}} = 1430.31 \text{ eV} \left(\frac{n_{\text{gas}}}{\text{cm}^{-3}}\right)^{4/7} \left(\frac{\Delta v}{10^{-3} c}\right)^{4/7} \left(\frac{R}{2.25 \cdot 10^{-5} \text{ cm}}\right)^{8/7} \left(\frac{1 \text{ eV}}{T_{\text{gas}}}\right)^{8/7}. \quad (2.16)$$

It is important to keep in mind that in cluster regimes, high gas temperatures usually lead to $\kappa \approx 1$. This can be shown when using the case distinction from Equation 2.8 and Equation 2.15 to check at which gas temperature $\kappa = 1$. It is shown in Figure 2.1 that if extremely high relative velocities can be reached, $\kappa > 1$ in regions where the ICM is no hotter than $527.59 \text{ eV} \approx 6.12 \times 10^6 \text{ K}$. AQNs with relative velocities of $\Delta v \sim 10^8 \text{ cm s}^{-1}$, on the other hand, are more likely, but require ICM temperatures of $T_{\text{gas}} \lesssim 268.04 \text{ eV} \approx 3.11 \times 10^6 \text{ K}$ to gain factors of $\kappa > 1$. Since typical ICM temperatures are in the range of $T_{\text{ICM}} \sim 10^7 - 10^8 \text{ K}$ (e.g. Sarazin (1986), Navarro et al. (1995), Mohr et al. (1999)), it is rather unlikely that many AQNs in central regions of galaxy clusters will obtain $R_{\text{eff}} \gg R_{\text{AQN}}$. With $\kappa = 1$ and taking the expression from Equation 2.7, T_{AQN} obey the following scaling after inserting suitable cluster parameters:

$$T_{\text{AQN}} \sim 6.95 \cdot 10^{-2} \text{ eV} \left(\frac{n_{\text{gas}}}{10^{-3} \text{ cm}^{-3}}\right)^{4/17} \left(\frac{\Delta v}{10^{-3} c}\right)^{4/17} \left(\frac{(1-g)f}{0.9}\right)^{4/17} \quad (2.17)$$

It might be possible to find regions of sufficiently low temperatures where the infalling substructures still can reach high Δv . For galaxies moving along the filaments and falling towards the central potential of the cluster chances would be increased. A high initial velocity in the filament would help to reach the desired velocity of the galactic halo with respect to the ICM. It is subject to [Subsection 3.1.3](#) to provide further details on the radial velocity profiles.

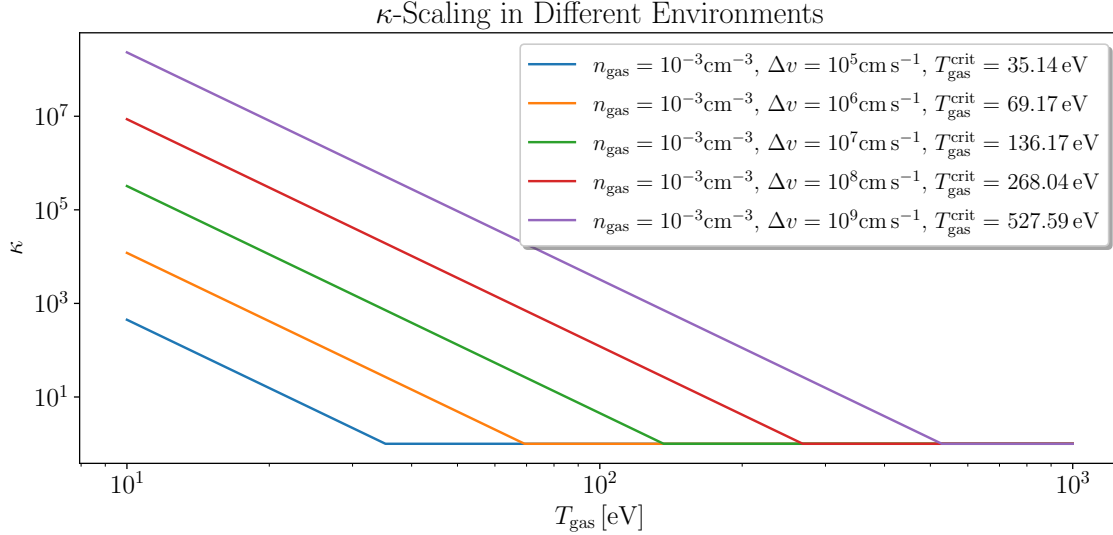


Figure 2.1: Transitions from $\kappa \geq 1$ to $\kappa = 1$ for different environmental properties of n_{gas} and Δv . The critical temperatures $T_{\text{gas}}^{\text{crit}}$ mark the transitional gas temperature of $\kappa \neq 1$ to $\kappa = 1$.

2.1.2 Radiation Processes of AQNs

AQNs can emit both thermal and non-thermal radiation. The key process is the annihilation of protons with anti-quarks in the core and – depending on how far a proton originating from the ionized gas can penetrate through the core – annihilation emission of the energy 2 GeV can either occur close to the surface or far in the centre of the quark core. The total surface emissivity was already introduced in [Equation 2.5](#) which was derived by [McNeil Forbes and Zhitnitsky \(2008b\)](#). It is the integral F of the spectral surface emissivity $dF/d\omega$ obtained by integrating the emissivity $\mathcal{E}(z) = dE/dt/dV$ of a Boltzmann gas of positrons for the cross-section of two positrons emitting a photon in the Boltzmann regime. The emissivity of the positrons in the electrosphere depends on the positrons' number density $n(z, T_{\text{AQN}})$, which in return depends on the radial distance z from the surface of the quark core (cf. [Section 1.2](#)) and the internal AQN temperature. It is explained in detail in [McNeil Forbes and Zhitnitsky \(2008b\)](#) that in these regions the emissivity will have the following form:

$$\frac{d\mathcal{E}}{d\omega} = \frac{8\alpha}{15} \left(\frac{\alpha}{m_e} \right)^2 n^2(z, T_{\text{AQN}}) \sqrt{\frac{2T_{\text{AQN}}}{m_e \pi}} \left(1 + \frac{\omega}{T_{\text{AQN}}} \right) e^{-\omega/T_{\text{AQN}}} h \left(\frac{\omega}{T_{\text{AQN}}} \right) \quad (2.18)$$

$$= \frac{8\alpha}{15} \left(\frac{\alpha}{m_e} \right)^2 \left(\frac{T_{\text{AQN}}}{2\pi\alpha} (z + \bar{z})^{-2} \right)^2 \sqrt{\frac{2T_{\text{AQN}}}{m_e \pi}} \left(1 + \frac{\omega}{T_{\text{AQN}}} \right) e^{-\omega/T_{\text{AQN}}} h \left(\frac{\omega}{T_{\text{AQN}}} \right) \quad (2.19)$$

$$(2.20)$$

Here, \bar{z} is an integration constant. After integrating, [McNeil Forbes and Zhitnitsky \(2008b\)](#) obtained the following expression:

$$\frac{dF}{d\nu} \simeq \frac{1}{2} \int_0^\infty \frac{d\mathcal{E}(\nu, z)}{d\omega} dz \quad (2.21)$$

$$\sim \frac{8}{45} \alpha^{5/2} T_{\text{AQN}}^3 \left(\frac{T_{\text{AQN}}}{m_e} \right)^{1/4} \cdot f(x) \quad (2.22)$$

With $f(x)$ being:

$$f(x) = (1+x)e^{-x} \begin{cases} (17 - 12 \ln(x/2)), & x < 1 \\ (17 + 12 \ln(2)), & x \geq 1 \end{cases} \quad (2.23)$$

and $x = 2\pi\nu/T_{\text{AQN}}$. Majidi et al. (in prep.) rewrote Equation 2.21 in physical units. This also changes x to $\tilde{x} = 2\pi\hbar\nu/(k_B T_{\text{AQN}})$, such that we get:

$$\frac{dF(\nu)}{d\nu} = \frac{8}{45} \frac{\alpha^{5/2} k_B^3 T_{\text{AQN}}^3}{\hbar^2 c^2} \left(\frac{k_B T_{\text{AQN}}}{m_e c^2} \right)^{1/4} \cdot f(\tilde{x}) \quad (2.24)$$

The definition in Equation 2.24 provides that T_{AQN} must be given in units of K. Figure 2.2 shows a plot of $dF(\nu)/d\nu$ for a set of internal AQN temperatures for $\nu \in [1.59 \times 10^{-9}, 10^5]$ eV. Temperatures which fall into the cluster regime are mostly abundant in the radio- and microwave bands.

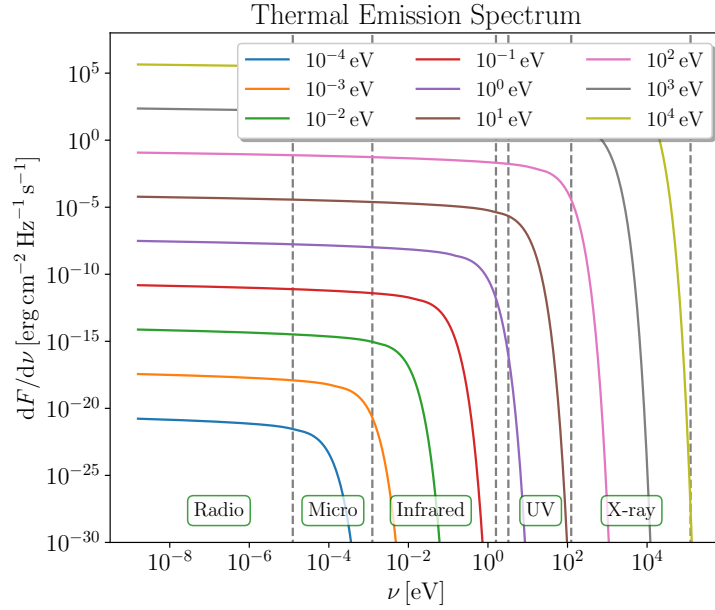


Figure 2.2: Spectral range for thermal emission from AQNs. The magnitude and width of a thermal spectrum increases for increasing T_{AQN} and can reach from radio to X-ray frequencies for extraordinary hot AQNs.

In the case of an annihilation process taking place at the surface of an AQN, one would expect non-thermal radiation to dominate, because energy can immediately escape as photons without being scattered in the core and hence no heating process will take place. Without providing a rigorous physical motivation, McNeil Forbes and Zhitnitsky (2008a) proposed the non-thermal emission per frequency to scale with:

$$\frac{dF(\nu)}{d\nu} = \frac{\nu}{\nu_c} \int_{\nu/\nu_c}^\infty K_{3/5}(x) dx \quad (2.25)$$

$K_{3/5}(x)$ is the second modified Bessel function. The critical frequency $\nu_c = \omega_c/(2\pi)$ was approximated by [McNeil Forbes and Zhitnitsky \(2008a\)](#) to be of the order of 30 keV following:

$$\omega_c \sim \sqrt{\frac{2\alpha}{3\pi}} \left(\frac{z_0}{z + z_0} \right)^2 \frac{\mu_0^2}{\epsilon_0 + \mu_0}, \quad (2.26)$$

with z_0 being the characteristic radial distance from the quark core surface, where the mean field approximation in the relativistic regime plays a dominant role. For a positron's chemical potential of $\mu_0 \sim 10$ MeV, the characteristic distance would be $z_0 \simeq 1.29 \times 10^{-11}$ cm. z can be any radial distance greater than z_0 that was not specified in their estimation. ϵ_0 is the positron's energy and is of the order of 5 MeV. Since no precise numerical value for ω_c can be established, we adapt the conventional value of $\omega_c = 30$ keV throughout this thesis. For the expression of the synchrotron function

$$\mathcal{F}(x) = x \int_x^\infty K_{3/5}(x') dx' \quad (2.27)$$

various approximations can be estimated by different approaches and integration methods (see for example [Crusius and Schlickeiser \(1986\)](#), [Rybicki and Lightman \(1986\)](#), [Weniger and Cížek \(1990\)](#), [Seidel \(2003\)](#), [Fouka and Ouichaoui \(2013, 2014\)](#), [Yang and Chu \(2017\)](#), [Palade and Pomârjanschi \(2023\)](#)). [Majidi et al. \(in prep.\)](#) provided an analytical function to approximate [Equation 2.27](#) provided that the synchrotron radiation is from a highly correlated beam:

$$\mathcal{F}(x) \approx 1.81x^\beta e^{-x} \equiv 1.81x^{1/3} e^{-x}. \quad (2.28)$$

It is important to note that β is usually not a fixed number and can vary depending on the energy distribution of positrons. Additionally, the exponent depends on the emission mechanism at the nugget's surface, which can be free-free emission rather than synchrotron. This would result in $\beta = 0$. It has been discussed to set β as a free parameter until further studies will provide better constraints. In order to obtain a rough understanding on the cosmological impact of the non-thermal emission on cluster environments, we follow the convention to adapt the numerical value of $\beta \equiv 1/3$ in our work, but have to keep in mind that the non-thermal AQN spectrum is not constrained well enough to propose definite predictions. With this in mind the non-thermal AQN emission has to be understood with caution. Nevertheless, the total surface emissivity of the non-thermal component can then be calculated by first, integrating over the whole spectrum:

$$F_{\text{X-ray}}(\nu) = \int_0^\infty \mathcal{F}(\nu) d\nu \quad (2.29)$$

$$= \frac{1.81}{\nu_c^{1/3}} \int_0^\infty \nu^{1/3} e^{-\nu/\nu_c} d\nu \quad (2.30)$$

After substituting ν/ν_c in the exponent of the integrand, we will find the following expression:

$$F_{\text{X-ray}}(\nu) = 1.81\nu_c \int_0^\infty u^{1/3} e^{-u} du \quad (2.31)$$

This integral can be solved by the integral form of the Γ -function:

$$\Gamma(n) = \int_0^\infty x^{n-1} e^{-x} dx. \quad (2.32)$$

Which gives us for the emission integrated over all frequencies:

$$F_{\text{X-ray}}(\nu) = 1.81\nu_c \Gamma\left(\frac{4}{3}\right) \quad (2.33)$$

After solving [Equation 2.33](#) for 1.81 and inserting it in:

$$\frac{dF(\nu)}{d\nu} = 1.81 \left(\frac{\nu}{\nu_c}\right)^{1/3} e^{-\nu/\nu_c}, \quad (2.34)$$

one finds the following expression:

$$F_{\text{X-ray}}(\nu) = \nu_c \Gamma\left(\frac{4}{3}\right) \frac{dF(\nu)}{d\nu} \left(\left(\frac{\nu}{\nu_c}\right)^{1/3} e^{-\nu/\nu_c} \right)^{-1} \quad (2.35)$$

Commencing with [Equation 2.3](#), the luminosity being radiated by an AQN after the collision of ionized particles is:

$$\frac{dE}{dt} = 4\pi R^2 F \quad (2.36)$$

with the total energy which is injected after one collision:

$$\frac{dE_{\text{X-ray}}}{dt} = 2\text{GeV} fg \sigma_{\text{eff}} \Delta v n_{\text{gas}} \quad (2.37)$$

Which is almost the same expression as [Equation 2.4](#) with the main difference being the factor fg instead of $(1-g)f$. This is because now – instead of thermalizing in the nugget with the fraction $(1-g)$ – we consider the fraction g that is radiated non-thermally after annihilation. The two equations lead to the expression:

$$F_{\text{X-ray}}(\nu) = \frac{2\text{GeV}}{4\pi R^2} fg \sigma_{\text{eff}} \Delta v n_{\text{gas}} \quad (2.38)$$

After setting [Equation 2.35](#) equal to [Equation 2.38](#), one obtains:

$$\frac{dF(\nu)}{d\nu} = \frac{2\text{GeV} fg n_{\text{gas}} \Delta v}{4\Gamma(4/3) \nu_c} \left(\frac{R_{\text{eff}}}{R}\right)^2 \left(\frac{\nu}{\nu_c}\right)^{1/3} e^{-\nu/\nu_c} \quad (2.39)$$

Here, $\sigma_{\text{eff}} = \pi R_{\text{eff}}^2$ was used. As a second option we try to physically motivate the approximate solution of the synchrotron function as an alternative expression to [Equation 2.28](#). It is important to account for random emission directions and one has to consequently compute the angle averaged spectral emission. [Crusius and Schlickeiser \(1986\)](#) carried this out for a mono-energetic isotropic electron distribution. Further, it should not matter whether we are considering positrons or electrons. We therefore present the approximate analytical solution provided by [Enßlin et al. \(1999\)](#):

$$\tilde{\mathcal{F}}(x) = x \int_0^{\pi/2} d\theta \sin \theta \int_{x/\sin \theta}^{\infty} dx' K_{3/5}(x') \quad (2.40)$$

$$= \frac{2^{2/3}}{\Gamma(11/6)} \left(\frac{\pi}{3}\right)^{3/2} x^{1/3} \exp\left(-\frac{11}{8} x^{7/8}\right) \quad (2.41)$$

After following the same steps for the integration, the non-thermal X-ray radiation can be expressed using [Equation 2.40](#):

$$\frac{dF(\nu)}{d\nu} = \frac{2\text{GeV} fg}{4 \frac{64}{77} \left(\frac{8}{11}\right)^{11/21} \Gamma(32/21)} \frac{n_{\text{gas}} \Delta v}{\nu_c} \left(\frac{R_{\text{eff}}}{R}\right)^2 \left(\frac{\nu}{\nu_c}\right)^{1/3} \exp\left(-\frac{11}{8} \left(\frac{\nu}{\nu_c}\right)^{7/8}\right) \quad (2.42)$$

The function modelling the non-thermal spectrum peaks at a frequency related to the critical frequency. It is important to note that the critical frequency of $\nu_c = 30 \text{ keV}/(2\pi)$, whose numerical value is set to 30 for conventional reasons, is not strictly constrained. The peak of the non-thermal emission shifts with the choice of ν_c . Here we will briefly present the peak frequency as a function of the critical frequency. First, a simpler form of Equation 2.42 can be defined by:

$$\tilde{F}_\nu = \left(\frac{\nu}{\nu_c}\right)^{1/3} \exp\left(-\varphi\left(\frac{\nu}{\nu_c}\right)^\gamma\right) \quad (2.43)$$

By taking the derivative of Equation 2.43, the maximum can be found at a frequency of:

$$\nu_{\max} = \frac{\nu_c}{(3\varphi\gamma)^{1/\gamma}}. \quad (2.44)$$

In the case of Equation 2.42, the parameters of Equation 2.44 become $\varphi = 11/8$ and $\gamma = 7/8$, which yields $\nu_{\max} \approx 1.10 \text{ keV}$. A plot of the non-thermal spectrum for typical R_{eff} , $n_{\text{gas}} = 10^{-3} \text{ cm}^{-3}$ and $\Delta v = 10^7 \text{ cm s}^{-1}$ in a galaxy clusters is shown in Figure 2.3. In most cases, $R_{\text{eff}} = R_{\text{AQN}}$, and when comparing this to Figure 2.2 for typical AQN temperatures in galaxy clusters ($T_{\text{AQN}} \in [10^{-2}, 10^{-1}] \text{ eV}$), it can be seen that the non-thermal emission is expected to be a few orders of magnitude lower than the thermal emission.

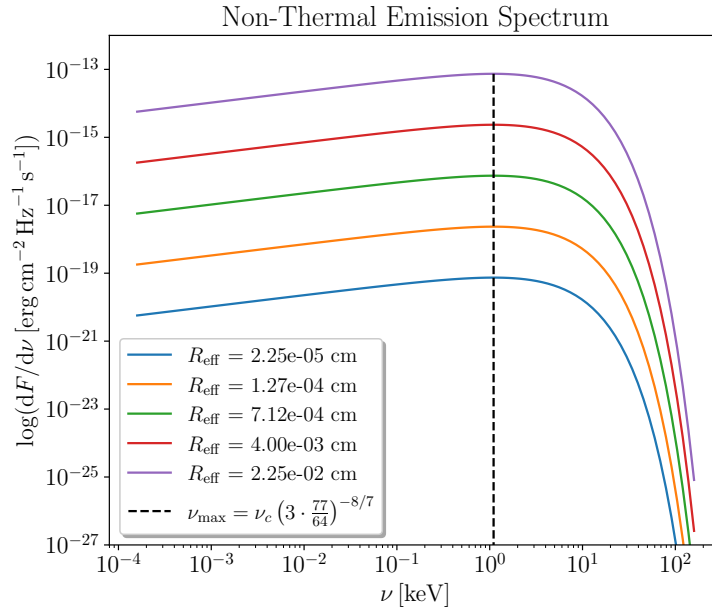


Figure 2.3: Non-thermal AQN emission spectrum for different R_{eff} . The position of the peak frequency is independent of the size of R_{eff} .

As a final remark, it has been discussed by other groups that the synchrotron function for modeling the non-thermal emission leading to a $1/3$ exponent in $(\nu/\nu_c)^{1/3}$ of Equation 2.42 might not be suitable, and larger exponents can be expected. It is therefore likely that this exponent will be left as a free parameter and that $1/3$ will be discarded in future studies.

In a system of multiple AQNs a more appropriate representation of radiation is the emissivity j_ν , which depends on the number density of AQNs n_{AQN} , and it is therefore crucial to evaluate the local number densities at each AQN instead of assuming a single n_{AQN} (the denser the environment, the more emission we can expect). A more detailed description how local properties in a particle simulations are inferred will be presented in Subsection 2.2.1. We will adapt Equation 1.13 for describing the number density, while we have to keep in mind

that $\rho_{\text{DM},i}$ should be evaluated at the i th AQN tracer particle. The emissivity is represented by:

$$j_\nu = 4\pi R_{\text{AQN}}^2 n_{\text{AQN}} \frac{dF(\nu)}{d\nu}. \quad (2.45)$$

2.2 Emission of Simulated Particles

2.2.1 Mapping AQN Properties onto Halo Tracer Particles

Cosmological simulations in the SPH formalism use tracer particles to represent environmental properties in a specific region. Depending on the resolution in our simulation a tracer has a mass of $M_{\text{part}} \sim 10^9 - 10^{10} h^{-1} M_\odot$. In the underlying AQN model, a particle will represent properties of temperature, density and its velocity relative to the environment within the region it exists in. In our analysis of the simulation, particle families are split into gas and halo tracer particles. The motion of halo tracer particles is only defined by their gravitational interactions with their surroundings. It is because of this property that halo tracer particles will serve as tracers for AQNs in this analysis. As proposed in [Equation 2.16](#), physical properties of AQNs rely on the cluster environment – more specifically, on the underlying gas properties of the ICM. It is not trivial that gas properties of SPH tracer particles can be mapped onto a single halo tracer particle and it will therefore be described in more detail how the mapping process was numerically implemented.

Tree Construction

Initially, the number of neighbouring gas particles that can influence the AQN properties was defined to be $N_{\text{neigh}} = 200$. Due to the sheer amount of hundreds of millions of particles within a single snapshot, it can be a tricky task to collect all neighbouring gas particles surrounding individual AQN particles. Sophisticated sorting algorithms that can provide a well-ordered data structure on the basis of the desired circumstances are therefore required to reduce the computational effort. In addition, structuring the gas particles by an algorithm that easily provides access to the metrics is also necessary. The package [NearestNeighbors.jl](#) ([Carlsson et al., 2022](#)) is a useful tool providing a built-in function to sort particles by the k -d tree algorithm.

A k -d tree generally splits points recursively into groups – in k dimensions, hyper-planes are responsible for splitting the sectors. In [Figure 2.4](#), a distribution of gas particles (red circles) is shown in a simplified setting for $k = 2$ dimensions. The algorithm starts to bisect the particles alongside an initial orientation which can arbitrarily be chosen, depending on the implementation on how the partition rules are set. In this example the initial orientation was set to be the x -axis with the x -position of the particle being closest to the median x -value of all particles in the underlying sector setting the intersection that divides the space in two (see line [①](#)). ‘A’ is therefore the root of the tree. Since the space is now separated in a left and right portion, particle position of the median y -position in each sector are computed and taken for the horizontal lines to separate the two halves (see lines [②](#) and [③](#)). This goes on until particles remain as leaves on the tree structure after intersecting the initial space in a maximum amount of subspaces. In this example ‘E’ and ‘F’ represent leaves of the tree.

Nearest Neighbour Localisation

Given a metric-constrained structure in the particle distribution it is now significantly easier to find nearest neighbours to a particle that is not part of the tree from the initial particle distribution. [Figure 2.5](#) shows that only a few relations have to be considered to find the corresponding nearest neighbour to the AQN particle that is visualized in a simplified manner

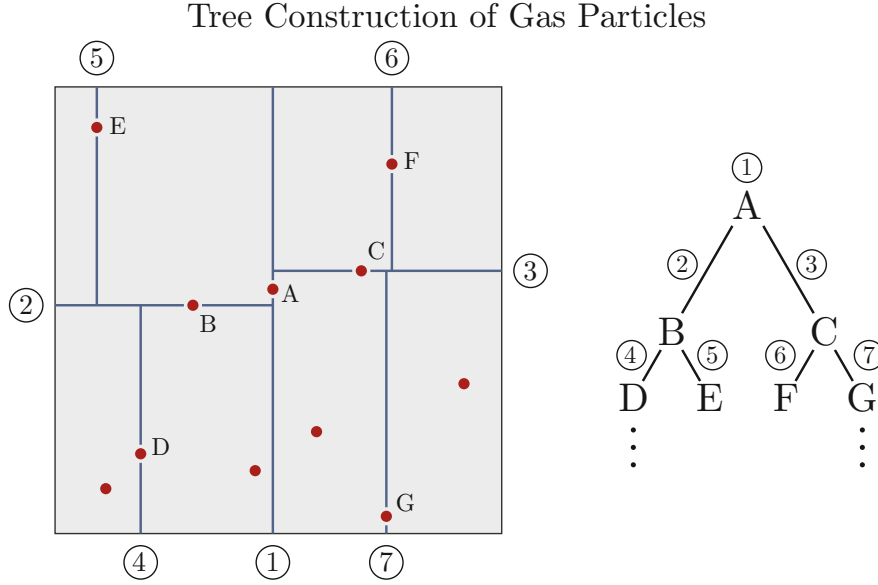


Figure 2.4: Schematic construction of a k -d tree starting from particle ‘A’.

in this sketch. This algorithm can recursively be carried out until the desired number of neighbours to the specific AQN were found.

Property Mapping

Now that for each AQN all gas particles were localized, the relative velocities in each of the x , y and z -coordinates to all neighbouring gas particle were calculated to infer the absolute relative velocity which is then saved in an array. Depending on their distance relative to the gas particles, AQNs are characterized by different weights \mathcal{W} for each neighbouring gas particle. Kernel weights are usually a function of the corresponding kernel function k_K , the AQN distance to the j th gas particle $d_{i,j}$ and the smoothing length $h_{\text{AQN},i} = \max(d)$ if $d \neq 0$ of an AQN with respect to the j th gas particle, i.e. $\mathcal{W}_{\text{AQN}}(k_K, d_{i,j}, h_{\text{AQN},i})$ and can be calculated by using the package `SPHkernels.jl` (Böss, 2023). A 3-dimensional Wendland C2 kernel was chosen for AQNs and a 3-dimensional Wendland C4 for gas particles (see Dehnen and Aly (2012) for choosing kernels). When considering the i th AQN particle any arbitrary SPH property A_j of the j th gas particle can be calculated according to Dolag et al. (2008) via:

$$\langle A_i \rangle = \sum_{j=1}^{N_{\text{neigh}}} \frac{m_{\text{gas},j}}{\rho_{\text{gas},j}} A_j \mathcal{W}_{\text{AQN}}(k_{C2}, d_{i,j}, h_{\text{AQN},i}) \quad (2.46)$$

In this case, this is how $\langle \Delta v_i \rangle$ was calculated. However, in order to properly infer gas properties at positions of AQN particles relative to their environment it is crucial to define a kernel that only computes weights from the given HSML property and their corresponding distances to the AQN. For the gas properties, we will therefore obtain the mapped gas particle SPH property onto the AQN via:

$$\langle A_i \rangle = \sum_{j=1}^{N_{\text{neigh}}} \frac{m_{\text{gas},j}}{\rho_{\text{gas},j}} A_j \mathcal{W}_{\text{AQN}}(k_{C4}, d_{i,j}, h_{\text{gas},j}) \quad (2.47)$$

This will finally give us the following set of equations that has to be solved numerically:

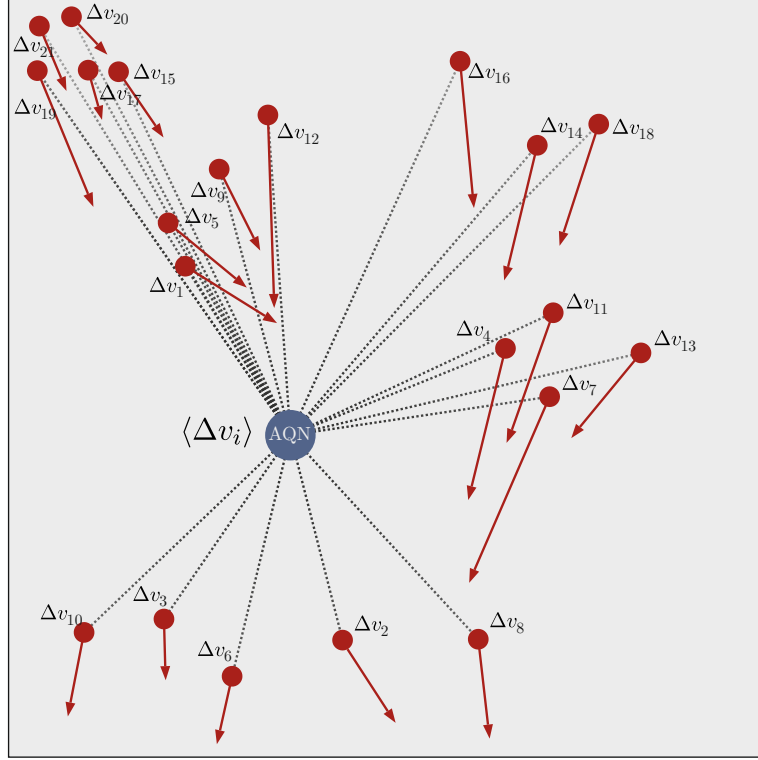


Figure 2.6: Schematic illustration of the SPH mapping process for Δv in an environment where a single AQN is surrounded by gas particles. Directions of velocity vectors are neglected since absolute relative velocities will be calculated as scalars.

2.2.2 ICM Bremsstrahlung

It is important to compare the AQN emission to gas emission in order to infer AQN excesses and to identify potential emission windows. Amongst other sources of radiation in the X-ray continuum, Bremsstrahlung coming from the hot ICM is the most dominant emission process (Felten et al. (1969), and Sarazin (1986) for an overview). Following Section 2.2.1, two different SPH gas properties are accessible: the gas properties at each AQN position and the gas properties at each gas particle. For gas emission, the latter will be chosen, since the spacial distribution of gas particles differs from the ones of halo tracer particles. It is specifically important to analyze different regions where gas emission is more prominent and where AQN positions might differ. The X-ray emissivity was calculated by utilizing the `x_ray_emissivity()` function taken from the `SPHtoGrid.jl` package (Böss, 2023). The X-ray emissivity $j_{\text{X-ray},\nu}$ depends on the hydrogen mass fraction X_H , the gas temperature T_{gas} , the gas density ρ_{gas} , on the gaunt factor $g(\nu, T_{\text{gas}})$ and the frequency ν . It has the following form:

$$j_{\text{X-ray}} = 4C_j g(\nu, T_{\text{gas}}) (1 + X_H)^2 \left(\frac{\tilde{n}}{\tilde{f} m_p} \right)^2 \rho_{\text{gas}}^2 [\text{g cm}^{-3}] \sqrt{T_{\text{gas}} [\text{keV}]} \\ \times \left(\exp \left(-\frac{h\nu_0 [\text{keV}]}{T_{\text{gas}} [\text{keV}]} \right) - \exp \left(-\frac{h\nu_1 [\text{keV}]}{T_{\text{gas}} [\text{keV}]} \right) \right) \text{erg cm}^{-3} \text{s}^{-1} \quad (2.54)$$

with

$$\tilde{n} = \frac{X_H + 0.5(1 - X_H)}{2X_H + 0.75(1 - X_H)} \quad (2.55)$$

and

$$\tilde{f} = \frac{4}{5X_H + 3} \quad (2.56)$$

$C_j = 2.42 \times 10^{-24}$ is a numerical factor provided by Bartelmann and Steinmetz (1996). Since a detailed comparison of the AQN and gas spectra requires the emissivity per unit frequency and Equation 2.54 only provides the emissivity in an integrated form, we will have to take the derivative per frequency bin in order to obtain the units $\text{erg cm}^{-3}\text{Hz}^{-1}\text{s}^{-1}$. In the numerical implementation a frequency array of 1000 elements was defined in the frequency range of $\nu \in [10^{-8}, 10^8]$ eV given in log-space. Each consecutive element has an increased factor of $a = \nu_{i+1}/\nu_i$, which is constant for any i . For the factor a , we can therefore choose $i = 0$ for simplification, i.e. the first element in the frequency array. The i th frequency band is then calculated by:

$$\Delta\nu_i = a\nu_i - \nu_i \quad (2.57)$$

A sufficient approximation of the derivation is then:

$$j_{\text{X-ray},\nu} = \frac{j_{\text{X-ray}}}{\Delta\nu_i} \quad (2.58)$$

2.2.3 Radiation Through Cosmic Rays

The package `SpectralCRsUtility.jl`¹ contains a function for calculating the synchrotron emissivity by adapting the model from Donnert et al. (2016) for a time-dependent spectral Cosmic Ray (CR) distribution $f(\hat{p}, t)$ with the CR momenta \hat{p} . The source code provides the analytical function for inferring the synchrotron emissivity following Böss et al. (2023a):

$$j_{\text{synch},\nu} = \frac{\sqrt{3}e^3}{m_e^2 c^3} B(t) \sum_{i=0}^{N_{\text{bins}}} \int_0^{\pi/2} d\theta \sin^2\theta \int_{\hat{p}_i}^{\hat{p}_{i+1}} d\hat{p} 4\pi\hat{p}^2 f(\hat{p}, t) K(x) \text{ erg cm}^{-3}\text{Hz}^{-1}\text{s}^{-1} \quad (2.59)$$

Here, $K(x)$ is the synchrotron kernel which is the integral of the Bessel function $K_{3/5}$ and $B(t)$ is the homogeneous time-dependent magnetic field.

As a result of hadronic interactions of CR protons in the ICM, they can lose energy through coulomb interactions. As a side effect pions will be produced and, when decaying, highly energetic γ -rays will be emitted. The same `SpectralCRsUtility.jl` package additionally contains the function `gamma_emissivity_pions()`, that estimates the γ -ray emissivity of CR protons by adapting the model from Werhahn et al. (2021).

2.2.4 SPH to Grid Mapping

When visualizing simulated tracer particles, it is important to include their corresponding properties with respect to their environment (i.e. smoothing length, mass and density of each particle). We would lose this information if we would only display the tracer particles in a scatter plot and the visualization would not be physically sensible. It is therefore crucial to adapt a method that maps SPH particle properties onto a two-dimensional grid. `SPHtoGrid.jl` (Böss, 2023) perfectly provides the necessary tools to map arbitrary particle properties of both gas and AQNs onto a grid. To generate SPH maps we first have to define mapping parameters that include information such as the physical size and the desired resolution in units of pixels that the generated image should have. Throughout this study a pixel size of $N_p = 2048$ was

¹<https://github.com/LudwigBoess/SpectralCRsUtility.jl/tree/master>

chosen. In order to map particle properties, a kernel function has to be chosen and can be as easily implemented as already described in [Section 2.2.1](#). Afterwards a physical weighting function has to be called to generate arrays in units of cm/px that include pixel side length in terms of the physical size kpc in units of cm per pixel in each element. With the given parameters and weights, the `sphMapping()` function can be called. With the respective particle positions, smoothing lengths, particle masses, densities, weights, mapping parameters, kernel and the desired mapping quantity, SPH maps will be generated and written as `fits` files. For emission quantities it is important to disable `reduce_image`, as this is only important if one is interested in obtaining the mean quantity along the line of sight, which is not the case for emissivity.

2.3 The Constrained Simulation of the Local Universe ‘SLOW’

The underlying simulation is a constrained cosmological simulation of the local universe, called ‘Simulating the LOcal Web (SLOW)’ ([Dolag et al., 2023](#)). Derived from the CosmicFlows-2 catalog ([Tully et al., 2013](#)), the peculiar velocity field can help to constrain initial conditions for a simulation of our local universe, when tracing back the trajectories up to a defined redshift. Tracers, like velocity and density fields are direct proxies for the underlying gravitational fields which are important for the initial conditions of the simulation. This study uses the constrained cosmological simulated simulation, covering a volume of $(500 h^{-1} \text{Mpc})^3$ and including 3072^3 gas and dark matter particles. It assumes a cosmology based on Planck measurements ([Planck Collaboration et al., 2014](#)), which are displayed in [Table 2.1](#). This simulation is non-radiative including magneto-hydrodynamics with a CR component [Böss et al. \(2023b\)](#). The CR component is required for the emission sources discussed in [Subsection 2.2.3](#), which can be accessed by reading in the blocks `CRpC`, `CRpN`, `CRpS` for the CR proton spectrum and `CReC`, `CReN`, `CReS` for the CR electron spectrum. The endings in the individual block names are the parameters that define the spectrum (see [Böss et al. \(2023b\)](#) for more details). Here, `C`, `N` and `S` refer to ‘cutoff’, ‘normalization’ and ‘slope’, respectively.

H_0 [km s ⁻¹ Mpc]	Ω_M	Ω_Λ	Ω_B	σ_8	n
67.77	0.307115	0.692885	0.0480217	0.829	0.961

Table 2.1: Table of the cosmological parameters adapted from [Planck Collaboration et al. \(2014\)](#) utilized in the SLOW simulation. From the left to right, the columns correspond to the Hubble constant H_0 , the total matter density Ω_M , the cosmological constant Ω_Λ , the baryon fraction Ω_B , the normalization of the power spectrum σ_8 and the slope of the primordial fluctuation spectra n as it was described in [Dolag et al. \(2023\)](#).

2.3.1 The Sample

In this work we tested the spectral emission of AQN quantitatively for a large sample and qualitatively for a small sample. A large sample of 150 galaxy clusters (which we call ‘sample \mathcal{A} ’) ordered in 5 corresponding mass bins was used to test scaling relations and mass dependencies for the search of emission excesses in the spectra. Each mass bin was defined to contain 30 galaxy clusters with bin sizes of $M_{\text{vir},1} \in [0.8, 0.9] \times 10^{14} M_\odot$, $M_{\text{vir},2} \in [1.1, 2.0] \times 10^{14} M_\odot$, $M_{\text{vir},3} \in [4.0, 5.0] \times 10^{14} M_\odot$, $M_{\text{vir},4} \in [7.0, 7.9] \times 10^{14} M_\odot$ and $M_{\text{vir},5} \in [10.7, 31.7] \times 10^{14} M_\odot$. Mass bins were arbitrarily chosen with the aim to maintain a relatively equal mass distribution and conserving a well-distributed population of virial masses. The lowest mass range was chosen to be $0.8 \times 10^{14} M_\odot$ due to the fact that it becomes tricky at lower masses to separate galaxy clusters from galaxy groups. As an upper mass range, the $31.7 \times 10^{14} M_\odot$ were obtained by taking the most massive galaxy clusters above the boundary of $10^{14} M_\odot$.

We used the subfind algorithm (Springel et al., 2001, Dolag et al., 2009) implemented into the `GadgetIO.jl` package (Böss and Valenzuela, 2023) to receive the necessary halo IDs in order to read out the halo and gas tracer particles within a certain box. Clusters from sample \mathcal{A} were selected by their virial mass while their corresponding particles were read out from a volume of $V_{\text{cluster},r_{200}} = (2 \times b \times r_{200})^3$ with $b = 1.5$ being the multiplier of how many r_{200} the cube is extending its side lengths.

‘Sample \mathcal{B} ’ consists of 11 out of 45 cross-identified galaxy clusters (Hernández-Martínez et al., 2024) that resemble digital twins to their real counterparts, which was then utilized to identify the most promising galaxy cluster candidates that exhibit AQN signatures. According to Hernández-Martínez et al. (2024), galaxy clusters from observations were cross-identified with simulated galaxy clusters by comparing their mass, X-ray luminosity, temperature and Compton- y signal. A probability of the cross-identification can be established by comparing these features to a random selection. By computing the significance, the authors could assess how well the cross-identified clusters are associated with each other. The most massive galaxy cluster from the digital twin-sample is Coma ($M_{\text{vir}} = 18.82 \times 10^{14} M_{\odot}$) and the least massive is Fornax ($M_{\text{vir}} = 0.61 \times 10^{14} M_{\odot}$). In sample \mathcal{B} , we selected particles from the volume $V_{\text{cluster},r_{\text{vir}}} = (2 \times b \times r_{\text{vir}})^3$.

Chapter 3

Results

Amongst physical AQN properties, emissivities like, for instance, thermal AQN, non-thermal AQN, thermal gas, and non-thermal CR processes have been calculated for a total of 167 galaxy clusters, split into two samples \mathcal{A} and \mathcal{B} . In order to get a first glance at the parameters that physically describe AQN properties and how they are influenced by their environment, several scaling relations will be presented in the following section. We furthermore study the distribution of the physical properties with respect to their host cluster masses.

3.1 Environmental Impact onto Physical Properties of AQNs

3.1.1 Scaling Relations

An important question to be answered is to what extent the mass of a galaxy cluster influences the strength of an AQN emission signature. This will be one of the intriguing problems to be tackled, and it is not always unambiguous which specific cluster property has a positive or negative impact on the final detectability of AQN signals. In the simplest terms, we seek galaxy clusters that mostly exhibit low ICM temperatures, high gas densities, and high relative velocities of gas with respect to halo substructures. However, it will become clear in the following sections that not all criteria must or can be fulfilled simultaneously.

Sample \mathcal{A} consists of $N_{\text{GC}} = 150$ galaxy clusters, each containing $N_{\text{part,DM}} \in [3.2, 94.3] \times 10^5$ particles, each characterized by their own properties. In addition to AQN properties such as T_{AQN} , n_{AQN} , R_{eff} , and Δv , but also gas properties, like for instance T_{gas} and n_{gas} will be stored for each halo tracer particle (as described in [Section 2.2.1](#)), resulting in a total of $N_{\text{prop}} = 6$ properties. Therefore, we need to store approximately $N_{\text{tot}} = N_{\text{part}} \times N_{\text{prop}} \times N_{\text{GC}} \in [2.9, 84.9] \times 10^8$ parameters to describe our full sample. Storing and analyzing this data efficiently is resource-intensive, and we will explore more efficient methods in the following sections.

Starting with the physical parameters, we calculate the median property values over all particles in a galaxy cluster, in order to grasp an initial physical understanding how median AQN properties scale with the surrounding gas. It is sensible to use median values instead of the mean, since single outliers in the parameter might not properly follow the overall distribution. Additionally, the parameter distributions are not always symmetric and not normal distributed. The median therefore provides a more robust representation of the central tendency.

When considering M_{vir} , we find that higher cluster masses will result in an increase of the median T_{AQN} , because the relative velocities increase for higher cluster masses. In particular, it can be seen in [Figure 3.1](#) (i) that high relative velocities of infalling substructures towards the central potential of the galaxy cluster are a dominant factor for contributing to an increasing T_{AQN} , since a deeper potential of massive clusters cause higher velocities of infalling

substructures (see for example Sarazin (1986), Bryan and Norman (1998), Sheth and Diaferio (2001) and Binney and Tremaine (1987)). On the other hand, it is still remarkable that AQN temperatures of $T_{\text{AQN}} > 4 \times 10^{-2} \text{eV}$ can be reached with low relative velocities even for the lowest M_{vir} . These outliers show the degree of degeneracy of the internal temperature model of AQNs. And it is specifically shown in Figure 3.1 (ii) that low T_{gas} are one of the dominating contributions for low cluster masses to obtain high internal AQN temperatures. It is easily explainable when keeping in mind that $T_{\text{AQN}} \propto T_{\text{gas}}^{-8/7}$. As it is shown in Figure 2.1, depending on the environment and relative velocities, critical gas temperatures of $T_{\text{gas}}^{\text{crit}} \sim \mathcal{O}(10^2 \text{eV})$ can be possible where $\kappa > 1$ – specifically in low galaxy cluster masses, gas temperatures are approximately in the same range. It is therefore more likely that galaxy clusters with low M_{vir} exhibit conditions where $\kappa > 1$, which is embedded in the scatter of relatively high T_{AQN} for low cluster masses in Figure 3.1 (ii).

On the other hand, it is important to point out that high Δv come with high T_{gas} , when comparing both subfigures in Figure 3.1. Galaxy clusters that show high median Δv (which are simultaneously relatively cold) are therefore hard to find. However, this is where the approach to analyze median values only reaches its limits, as relative velocities are local features of substructures falling through the central potential. Local high Δv features might therefore be hidden in the median Δv values.

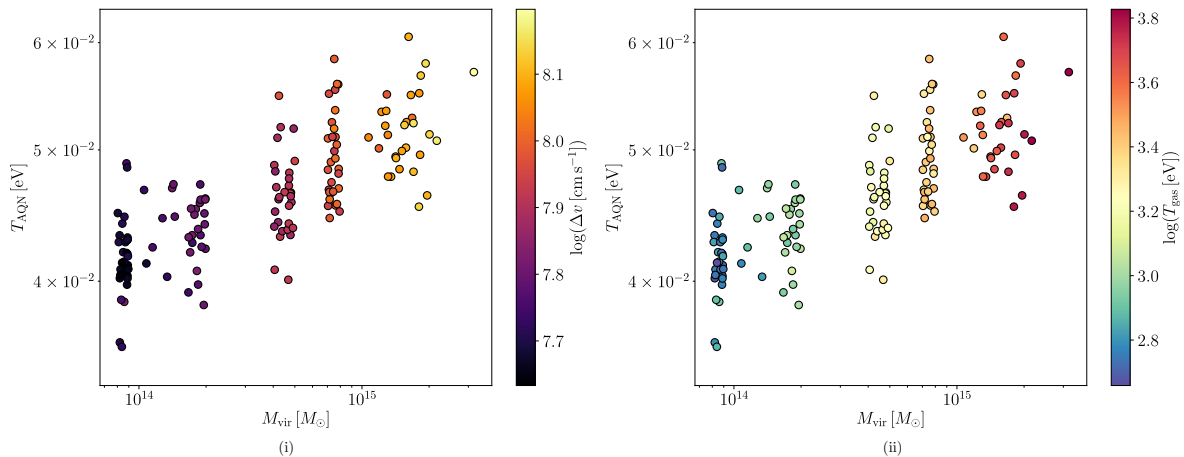


Figure 3.1: (i) & (ii) M_{vir} versus median T_{AQN} for all particles in each of the 150 galaxy clusters. (i) Δv in the colormap increase for increasing cluster masses. AQNs in low M_{vir} with low Δv are still capable of obtaining high T_{AQN} . (ii) T_{gas} increases for increasing M_{vir} . High T_{AQN} in low M_{vir} can be reached because gas with low median T_{gas} resides in these environments. A value of $\kappa > 1$ therefore becomes more likely, which can positively contribute to a rise in T_{AQN} .

Furthermore, it is displayed in Figure 3.2 (i) that clusters with the highest T_{AQN} also host gas with the highest T_{gas} . At a first glance this might appear counterintuitive because of Equation 2.16. We have to keep in mind that this equation does not hold true in all environments as κ will be set to 1 at a certain threshold of the gas temperature – otherwise, R_{eff} would be smaller than R_{AQN} , which is physically not realistic. Therefore, at some point the ICM temperature will not play a crucial role anymore, because relative velocities and gas number densities will dominate (cf. Equation 2.17). This consequence is visible in Figure 3.2 (ii), where high T_{AQN} will be reached with a combination of high Δv and n_{gas} . Galaxy clusters that show similar Δv clearly stand out with a higher median T_{AQN} when their overall n_{gas} is larger.

3.1.2 Histograms

Given the indication that high relative velocities scale with the cluster mass (see Figure 3.1 (i)), it is important to study its parameter distribution alongside other physical AQN parameters.

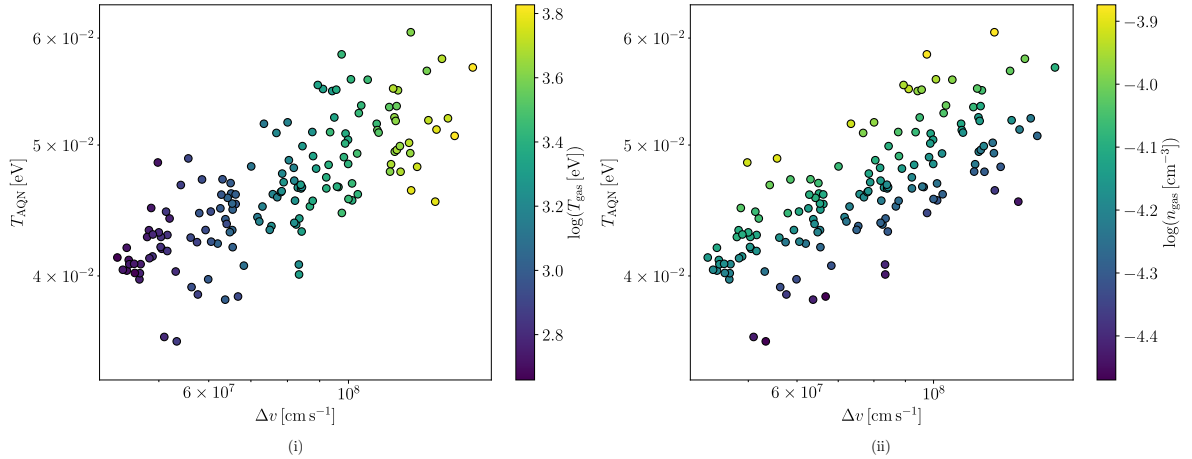


Figure 3.2: Scaling relations of Δv versus T_{AQN} color-coded by (i) T_{gas} and (ii) n_{gas} . High T_{AQN} can still be reached for high T_{gas} , because $\kappa = 1$. In these regimes only Δv and n_{gas} will contribute to the internal temperature of AQNs.

As mentioned before, values from Figure 3.1 and Figure 3.2 only represent the median out of a full distribution of $\sim 10^6$ particles per galaxy cluster. Since the median is less sensitive to outliers and will only provide information on central tendencies, it is crucial to have an understanding whether only minor individual or a wide distribution of properties contribute the most to the median value.

Histograms in Figure 3.3 show the distribution of T_{AQN} , Δv , n_{AQN} , R_{eff} , n_{gas} and T_{gas} , respectively. Out of the distributions of all 150 galaxy clusters, the median distribution in each mass bin, i.e. for 30 galaxy clusters each, was taken and plotted. It can be seen that – the larger the range gets – all properties show a relatively wide distribution with fewer outliers. Since the cluster mass directly scales with the particle numbers, a general trend of increased total counts can be seen in all histograms – however it is interesting to see how the shape of the histograms changes for increasing mass bins.

- **Internal AQN temperature:** The T_{AQN} -histogram is heavily weighted for values of $T_{\text{AQN}} \in [10^{-2}, 10^{-1}]$ eV and occasionally high $T_{\text{AQN}} \gtrsim 1$ eV can be possible for massive clusters. Peaks in the distribution shift from approximately 4×10^{-2} eV to 6×10^{-2} eV for increasing cluster masses. Here, Δv is likely to play the dominating factor (as discussed before).
- **Relative velocity:** In the Δv -histogram, most of the particles are distributed towards $\Delta v \sim 10^8 \text{ cm s}^{-1} \sim 0.3\%c$. Intriguingly, an additional low velocity population component of $\Delta v \lesssim 10^6 \text{ cm s}^{-1}$ seems to be present especially in massive galaxy clusters. A Δv peak shift towards higher velocities for larger cluster masses can be observed as well.
- **AQN number density:** Following Equation 1.13, values in the n_{AQN} -histogram are generally low, since AQNs are large and massive compared to elementary particles. Therefore, a smaller abundance of AQN is required, which results in low n_{AQN} .
- **Effective AQN radius:** The R_{eff} -histogram directly shows that most of the R_{eff} are set to $R_{\text{AQN}} = 2.25 \times 10^{-5} \text{ cm}$, since $\kappa = 1$ in most environments. Depending on the cluster mass, the general shape of the R_{eff} distribution does not change. However, the more AQNs can reach effective radii of $R_{\text{eff}} \gtrsim 10^{-2} \text{ cm}$ at maximum. This is an interesting outcome, since more massive clusters are typically characterized by a hotter ICM, which attenuates the value of R_{eff} (cf. Equation 2.13), but the peak shift in Δv towards higher velocities can be occasionally responsible for a stronger influence on R_{eff} than T_{gas} .

- **Gas number density:** n_{gas} shows a reasonable distribution with a heavier weight in number densities of $n_{\text{gas}} < 10^{-3} \text{cm}^{-3}$, because particles were read from a box of $2 \times 1.5 \times r_{200}$ side length and especially in the outskirts one would expect lower values of n_{gas} .
- **Gas temperature:** For increasing M_{vir} in galaxy clusters the peak in the T_{gas} -histograms shifts to larger values. Higher gas temperatures for heavier galaxy clusters can be expected due to a steeper potential that in return attracts more substructures. A constant infall of new galaxies continuously heats up the ICM and provides a general increase in T_{gas} (see Sarazin (1986), for a review).

3.1.3 Radial Profiles

A better understanding on the spatial distribution of AQN properties in galaxy clusters can be obtained when considering their radial profiles. Figure 3.4 shows how SPH properties, for instance T_{AQN} , Δv , n_{AQN} , R_{eff} , n_{gas} and T_{gas} , mapped onto the position of AQNs scale with increasing distances from the cluster's center of mass. Radial profiles were taken from each galaxy cluster in sample \mathcal{A} and the median radial profile was taken for each mass bin. SPH properties were inferred according to the proposed methodology in Subsection 2.2.1.

Generally speaking, T_{AQN} , Δv and T_{gas} increase with the mass of the galaxy cluster. A scaling relation of M_{vir} and the aforementioned properties was already identified in Subsection 3.1.2. T_{gas} and infall velocities have already been discussed in various studies and therefore does not require further comments (Sarazin (1986) and Binney and Tremaine (1987) for a collection of scaling relations). On the other hand, the properties n_{AQN} , R_{eff} and n_{gas} appear to radially scale independently with respect to the mass.

- **Internal AQN temperature:** T_{AQN} are most likely increasing for different masses with higher Δv . For larger radii and in all mass bins, T_{AQN} seems to converge towards a single radially normalized value. Given the underlying AQN model, it is assumed that T_{AQN} will artificially rise for radii $r \gg 1.5 r_{200}$, because $R_{\text{eff}} \rightarrow \infty$ for $T_{\text{gas}} \rightarrow 0 \text{K}$ (more details in the R_{eff} bullet point). Moreover, this means that at a certain relative distance, T_{AQN} will mainly be influenced by properties of filaments and voids.
- **Relative velocity:** An interesting outcome of the radial Δv profiles are that for the most massive galaxy clusters the profile increases towards normalized distances of $r/r_{200} \sim 0.1$ and decreases at larger distances. Relatively flat radial profiles until $r/r_{200} \sim 0.3$ can be seen for intermediate mass bins, i.e. $M_{\text{vir}} \in [7.0, 8.0] \times 10^{14} M_{\odot}$ and $M_{\text{vir}} \in [4.0, 5.0] \times 10^{14} M_{\odot}$ and $M_{\text{vir}} \in [1.0, 2.0] \times 10^{14} M_{\odot}$. In the smallest mass bin, a steady decrease towards larger radii can be observed.
- **AQN number density:** The radial shape of n_{AQN} follows the normal dark matter distribution by definition of Equation 1.13 $n_{\text{AQN}}(r) \sim \rho_{\text{DM}}(r)$. The profile is constantly offset to smaller values since a lower total number of AQNs is required to enclose the same mass a cluster halo contains.
- **Effective AQN radius:** R_{eff} represents an intriguing property of AQNs since (due to the high ICM temperature in the central regions) the gas properties do not permit effective radii to be larger than R_{AQN} . At larger distances, individual regional properties enable small increases in R_{eff} that highly depend on the degenerate AQN properties present in the surrounding gas. Single substructures might be capable to obtain large effective radii, and it is subject to Section 3.3 to identify these regions in spatially resolved maps of individual galaxy clusters to properly infer their physical properties. It is important to note that a slight trend of increasing R_{eff} can already be observed at

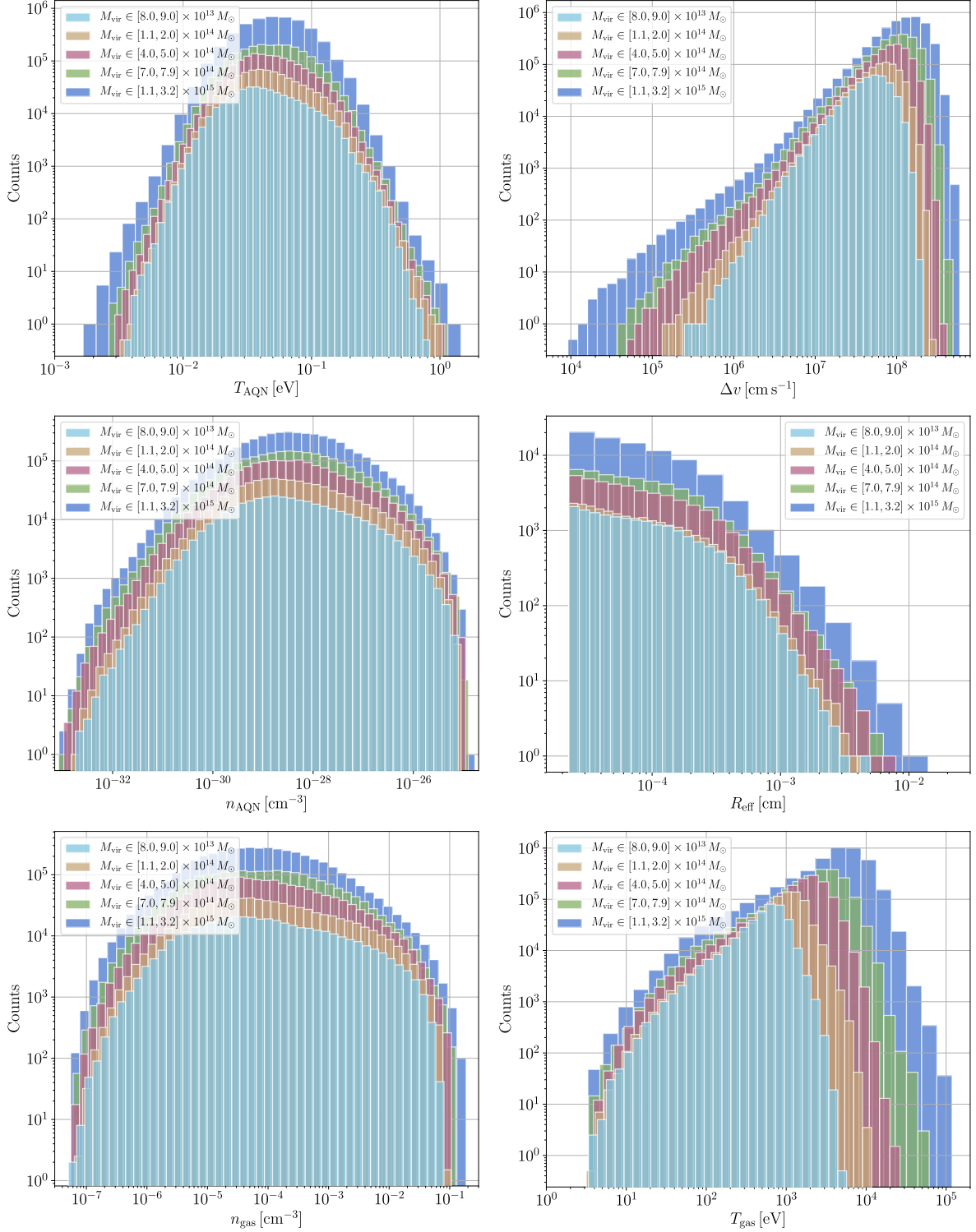


Figure 3.3: Histograms of of physical properties relevant to the AQN emission. Median values were taken for each mass bin, i.e. for 30 galaxy clusters, respectively.

$r \leq 1.5 r_{200}$. Even though the increase is almost negligible with a maximum increase of R_{eff} hosted by the lowest cluster mass bin of $\Delta R_{\text{eff}} \simeq 8.08 \times 10^{-7}$ cm (i.e. an increase of $\sim 3.6\%$), the phenomenon of higher R_{eff} in the peripheries becomes more significant the further the distance is. This is a feature of the underlying AQN model that was anticipated for this thesis, since AQNs are expected to be surrounded by a fully ionized gas. In regions of $r \gg 1.5 r_{200}$, smaller T_{gas} values consequently yield large R_{eff} , as

ionized particles can be captured over larger distances if the thermal motion of the ions is sufficiently low. This will lead to a runaway effect for increasing R_{eff} that is not physically meaningful. It is therefore crucial to constrain the sample to galaxy cluster regions with an extent of approximately $r_{\text{max}} \sim 1.5 r_{200}$ (or $r_{\text{max}} \sim 1.5 r_{\text{vir}}$ in the case of sample \mathcal{B}) at maximum for the underlying AQN model.

- **Gas number density:** No radial tendency can be observed in the different mass bins for n_{gas} and no outstanding spatial features can be observed in the radial profiles. As expected, number densities decrease from $\sim 10^{-3} \text{cm}^{-3}$ to lower values from the center towards the cluster's peripheries.
- **Gas temperature:** All mass bins show relatively flat temperature profiles and only the lowest mass bin exhibits temperatures $T_{\text{gas}} < 10^2 \text{eV}$. The more massive the cluster, the steeper the slope at $r \gtrsim 0.3 r_{200}$.

3.2 Spectral Profiles

A spectral energy distribution can be obtained by using Equation 2.24, Equation 2.42, Equation 2.54 and Equation 2.59 for thermal and non-thermal AQN emission, thermal Bremsstrahlung emission from the ICM and CR emission, respectively. It shall be noted that we have to apply Equation 2.45 to Equation 2.24 and Equation 2.42, in order to obtain an emissivity in units of $\text{erg cm}^{-3} \text{Hz}^{-1} \text{s}^{-1}$. The emissivity is then calculated for each particle in each frequency in a range of $\nu \in [10^{-8}, 10^8] / (2\pi) \text{eV}$ with a spectral resolution of 10^3 bins for AQN and gas. For the CR synchrotron emission and the CR pion decay emission frequency ranges of $\nu_{\text{synch}} \in [10^{-8}, 10^{-1}] / (2\pi) \text{eV}$ and $\nu_{\gamma} \in [10^{-3}, 10^1] \text{GeV}$ were chosen respectively in a spectral resolution of 100 bins. Figure 3.5 displays the spectral energy distribution of the five mass bins from sample \mathcal{A} : Here, the median for each frequency in each mass bin was taken out of the 30 respective galaxy clusters. AQN thermal emission, non-thermal emission, ICM Bremsstrahlung, CR synchrotron emission and pion decay emission are represented by solid, dash-dot-dotted, dashed, dash-dotted and dotted lines, respectively.

It is noticeable that higher cluster masses result in an increment of the general spectral energy. In this figure, the reader's attention shall be drawn towards the regions where both of the AQN emission become comparable to the ICM Bremsstrahlung emission in the low and high energy regime, as it is possible to obtain small frequency windows where AQN emission would overtake the ICM Bremsstrahlung. In the low energy regime of $\nu_{\text{low}} \lesssim 10^{-3} \text{eV}$, AQN and ICM emission roughly increase equally for higher M_{vir} . This opens the possibility that thermal AQN radiation has a potential to outshine ICM Bremsstrahlung independently of cluster masses.

It becomes a bit more tricky when comparing non-thermal AQN emission to the high energy Bremsstrahlung regime in frequencies of $\nu_{\text{high}} \gtrsim 10 \text{keV}$. Non-thermal AQN emission will increment not as strongly as X-ray emission of the hot cluster gas. Since $j_{\text{X-ray}} \sim \rho_{\text{gas}}^2 T_{\text{gas}}^{1/2}$ (see Equation 2.54) and T_{gas} increases with M_{vir} (see Figure 3.3), $j_{\text{X-ray}, \nu}$ will especially increase drastically for increasing M_{vir} in the high energy regime, leading to the circumstance that non-thermal AQN is expected to only be visible in sufficiently low cluster masses.

The CR contributions embedded in synchrotron and pion decay emission in Figure 3.5 are increasing for higher M_{vir} because of resolution constraints in the simulation. Galaxy clusters that are too low in mass cannot resolve CR populations sufficiently and will therefore yield lower synchrotron and pion decay emission. In the most extreme cases it is even possible that CR SPH particle abundance is below 10 in an entire galaxy cluster. Emission from pion decay does not interfere with the AQN spectrum because the decay of pions results in higher photon energies as non-thermal AQN could possibly produce. Synchrotron emission, on the other

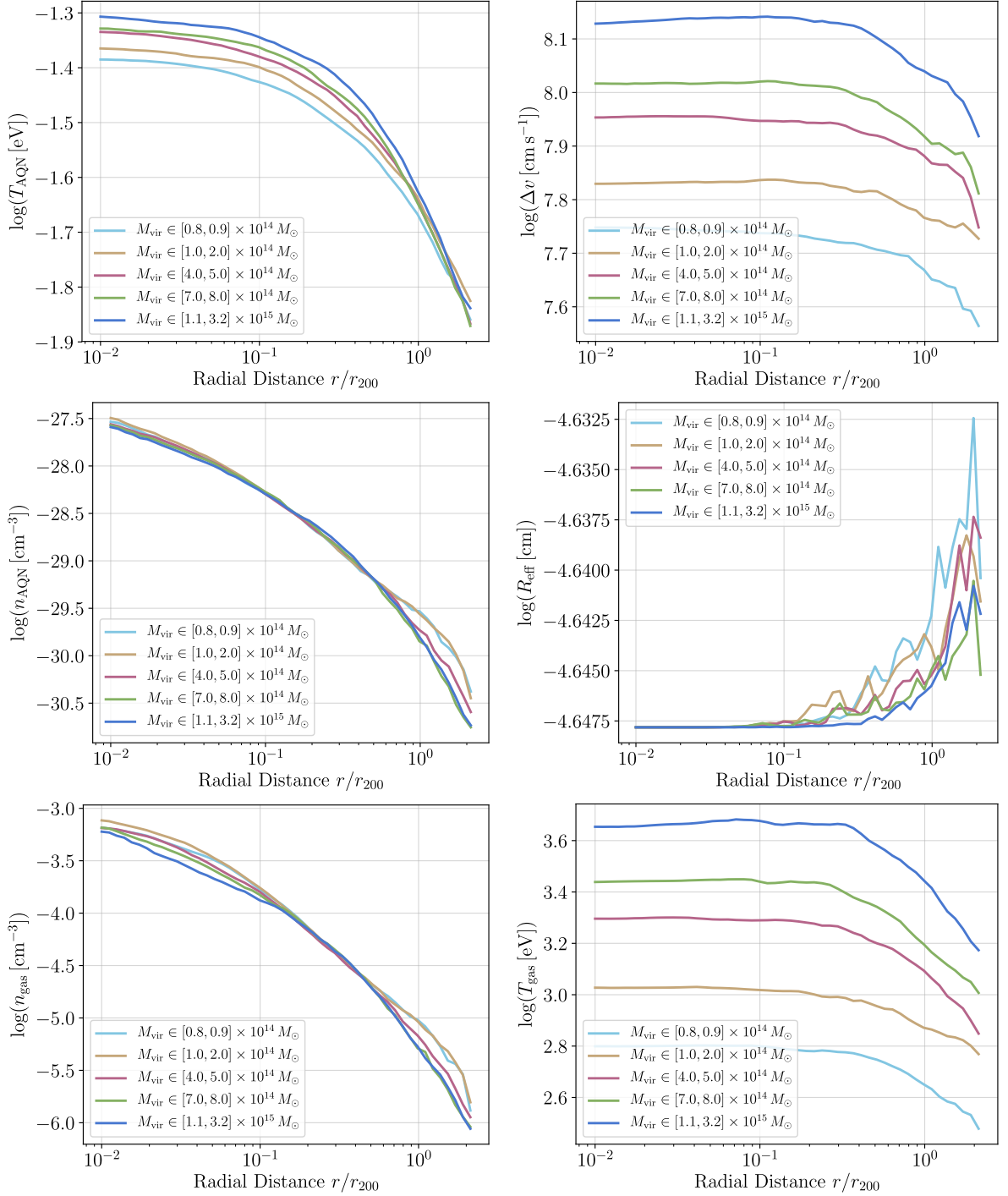


Figure 3.4: Radial profiles of T_{AQN} , Δv , n_{AQN} , R_{eff} , n_{gas} and T_{gas} mapped onto AQN tracer particles. The median radial profile was taken for each mass bin (i.e. 30 galaxy clusters each) and compared to other mass bins in a region of $r \in [0, 1.5] r_{200}$.

hand is likely to interfere with the thermal AQN emission, especially in the regions where thermal AQN emission would dominate the ICM Bremsstrahlung emission. It is therefore worth noting that one has to account for synchrotron emission and ICM Bremsstrahlung in the low energy regime when searching for an optimal frequency window for thermal AQN emission.

In the following paragraphs we will focus on the promising frequency bands where AQN emission is expected to dominate. First, in order to measure how strongly AQN emission

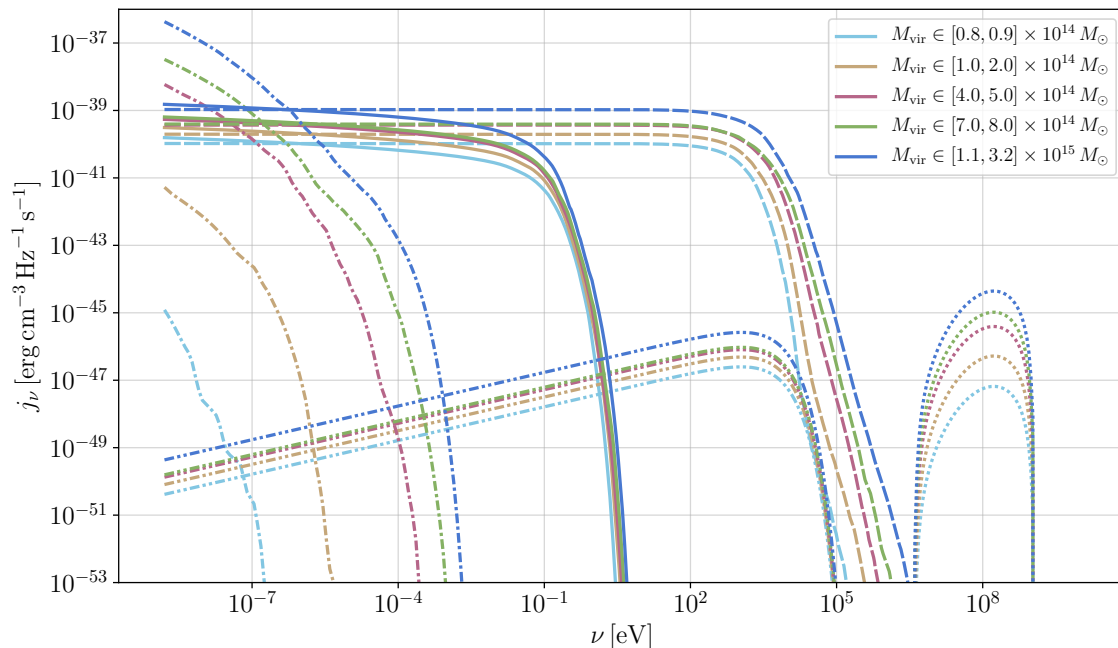


Figure 3.5: Median cluster spectrum with lines for each mass bin out of sample \mathcal{A} over a frequency range of $\nu \in [10^{-8}, 10^8]/(2\pi)$ eV. The solid, dash-dot-dotted, dashed, dash-dotted and dotted lines represent AQN thermal emission, non-thermal emission, ICM Bremsstrahlung, CR synchrotron emission and pion decay emission, respectively.

outshines the background emission a metric has to be defined that includes the frequency and the magnitude of the increment in emission. Depending on mass and other physical properties of the galaxy cluster, thermal and non-thermal AQN emission will distinctively be higher or lower in individual frequencies for different galaxy clusters. Therefore, a transition frequency ν_T has to be defined, where the absolute $j_{\text{AQN},\nu}$ value transitions from higher to lower values compared to the background emission $j_{\text{background},\nu}$. Both emissivities for AQN and background will be integrated from a minimum frequency ν_{min} to the transition frequency. In the simulation, the numerical integration is conducted by applying the trapezoidal rule which is implemented in the `NumericalIntegration.jl` package.¹

3.2.1 Low Frequency Regime

For the low energy regime, we define ν_{min} to be the lowest possible frequency that was used to calculate the spectra, i.e. $\nu_{\text{min}} = 10^{-8}/(2\pi)$ eV. As it is shown in a general sketch in Figure 3.6, the emissivities will be integrated and the background flux will be subtracted from the AQN flux in the frequency range of ν_{min} to ν_T . We will hereby obtain the integrated spectral difference $\Delta j(\nu_{\text{min}}, \nu_T)$:

$$\Delta j(\nu_{\text{min}}, \nu_T) = \int_{\nu_{\text{min}}}^{\nu_T} j_{\nu, \text{AQN}} d\nu - \int_{\nu_{\text{min}}}^{\nu_T} j_{\nu, \text{background}} d\nu. \quad (3.1)$$

In the following, the $\Delta j(\nu_{\text{min}}, \nu_T)$ was determined in both the low and high energy regimes for sample \mathcal{A} and sample \mathcal{B} . After applying the condition that thermal AQN emission has to be higher than thermal gas emission at frequencies below ν_T , one obtains a slightly reduced sample of 91.3% out of 150 galaxy clusters from sample \mathcal{A} . Figure 3.7 shows the integrated spectral difference in dependence of the transition frequency. Due to the integration itself, a

¹<https://github.com/dextorious/NumericalIntegration.jl>

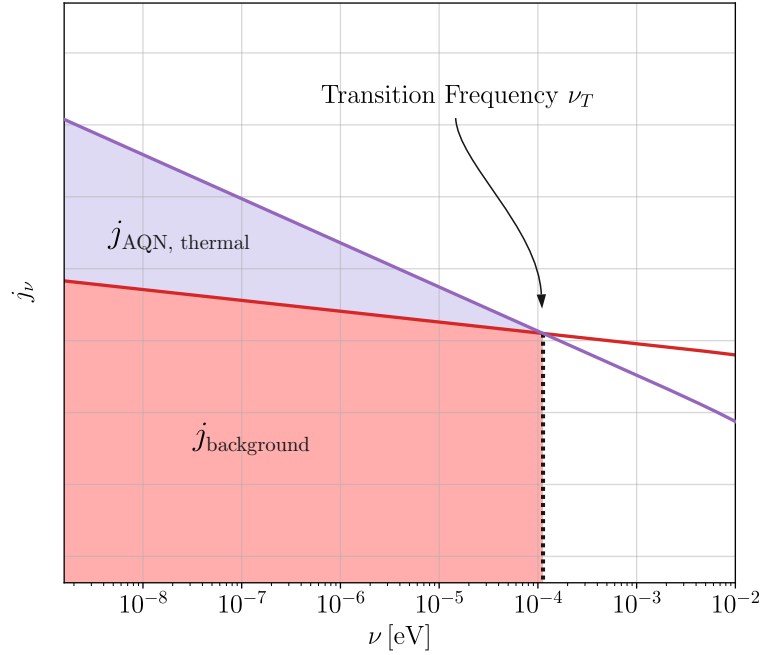


Figure 3.6: General spectral sketch for an arbitrary galaxy cluster exhibiting thermal AQN emission that outshines the background emission in a certain frequency band. The transition frequency ν_T is defined where $j_{\text{AQN,thermal},\nu} < j_{\text{background},\nu}$ with $\nu_{\text{min}} < \nu_T$ and ν_{min} being the minimum possible frequency where $j_{\text{AQN,thermal},\nu} > j_{\text{background},\nu}$.

larger surface area of the offset of AQN versus background emission can be observed for higher ν_T . An important outcome is that galaxy clusters with relatively low M_{vir} are still capable of reaching high $\Delta j(\nu_{\text{min}}, \nu_T)$ and follow relatively well-constrained tangents indicated by the colormap for different cluster masses (see Figure 3.7 (i)). The same trend can be seen in colormaps showing the ICM Bremsstrahlung emission integrated over the full frequency range of $\nu_0 = 10^{-8}/(2\pi)$ eV to $\nu_1 = 10^8/(2\pi)$ eV, because thermal emission of the ICM scales with the gas temperature and therefore with the galaxy cluster mass (see Figure 3.7 (ii)).

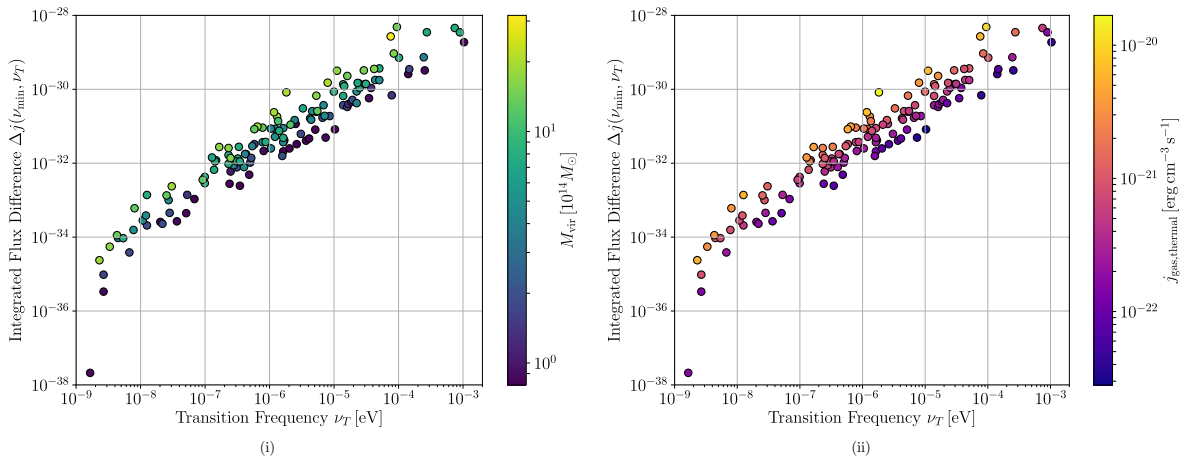


Figure 3.7: Transition frequency-integrated spectral difference relation color-coded by (i) M_{vir} and (ii) $j_{\text{gas,thermal}}$. The slope of the ν_T - $\Delta j(\nu_{\text{min}}, \nu_T)$ relation highly depends on the total thermal gas emission and the cluster mass.

These scatter plots show how strongly the AQN emission depends on the physical properties of the galaxy clusters and that their radiation offset is highly dictated by parameters in dependence to the corresponding transition frequency that are important to describe gas

emission and AQN emission. The population dependency of M_{vir} and $j_{\text{gas,thermal}}$ in the scatter plots of $\Delta j(\nu_{\text{min}}, \nu_T)$ is visible due to different scales of $j_{\text{AQN,thermal},\nu}$ and $j_{\text{gas},\nu}$. When assuming $R_{\text{eff}} = R_{\text{AQN}}$ and following Equation 2.21 with Equation 2.45 we find that

$$j_{\text{AQN,thermal},\nu} \sim n_{\text{AQN}} T_{\text{AQN}}^{17/4} \sim n_{\text{AQN}} n_{\text{gas}} \Delta v, \quad (3.2)$$

provided that $f(x)$ from Equation 2.23 does not strongly change. Thermal emission from the ICM on the other hand scales according to Equation 2.54 with:

$$j_{\text{gas},\nu} \sim n_{\text{gas}}^2 \sqrt{T_{\text{gas}}} \quad (3.3)$$

It was already seen in Figure 3.3 and Figure 3.4 that n_{gas} and n_{AQN} do not change with cluster mass. Therefore, in Figure 3.7, $j_{\text{AQN,thermal},\nu} \sim \Delta v$ and $j_{\text{gas},\nu} \sim \sqrt{T_{\text{gas}}}$ for increasing cluster masses when galaxy clusters populate the same ν_T . A constant shift of $\Delta j(\nu_{\text{min}}, \nu_T)$ for fixed ν_T comes from a stronger general increment of Δv over $\sqrt{T_{\text{gas}}}$ for increasing cluster masses, and we therefore expect that the integrated spectral difference is at fixed ν_T in fact a function of Δv and T_{gas} . This trend can be seen in Figure 3.8 (i).

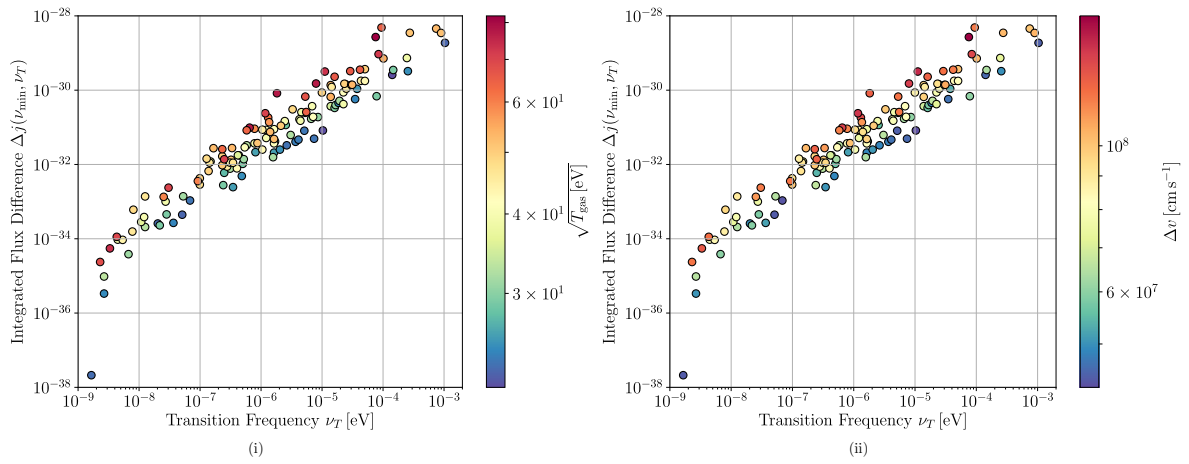


Figure 3.8: Transition frequency-integrated spectral difference relation color-coded by (i) $\sqrt{T_{\text{gas}}}$ and (ii) Δv .

It is important to find out how cross-correlated galaxy clusters populate in this relation in order to identify promising real-world cluster candidates. It is therefore shown in Figure 3.9 how sample \mathcal{B} is distributed in the ν_T - $\Delta j(\nu_{\text{min}}, \nu_T)$ diagram. In Figure 3.9, it can be seen that Fornax and Virgo appear to be the best candidates for the strongest AQN emission offset with respect to the background gas emission while extending to the highest ν_T . Coma cluster, on the other hand, is interestingly enough the least promising candidate for a significant thermal AQN emission excess. Coma is the most massive galaxy cluster out of sample \mathcal{B} and does not show a strong signature in AQN emission, most likely because T_{gas} and Δv cause an equilibration in the AQN and gas emission.

For Figure 3.8 and Figure 3.9, it is important to note that this comparison did not account for background synchrotron emission anticipated to play an important role for more massive galaxy clusters in the simulation, which will be subject to the following paragraphs.

When including synchrotron emission, Equation 3.1 has to be completed with:

$$\Delta j(\nu_{\text{min}}, \nu_T) = \int_{\nu_{\text{min}}}^{\nu_T} j_{\nu,\text{AQN}} d\nu - \int_{\nu_{\text{min}}}^{\nu_T} j_{\text{gas,thermal}} d\nu - \int_{\nu_{\text{min}}}^{\nu_T} j_{\text{synch},\nu} d\nu. \quad (3.4)$$

In cases of $\Delta j(\nu_{\text{min}}, \nu_T) < 0$ thermal AQN emission would not be detectable. Here, ν_T is still defined as the frequency where AQN emission intersects with the gas emission. This frequency range was adapted for the synchrotron emission integral, where either the

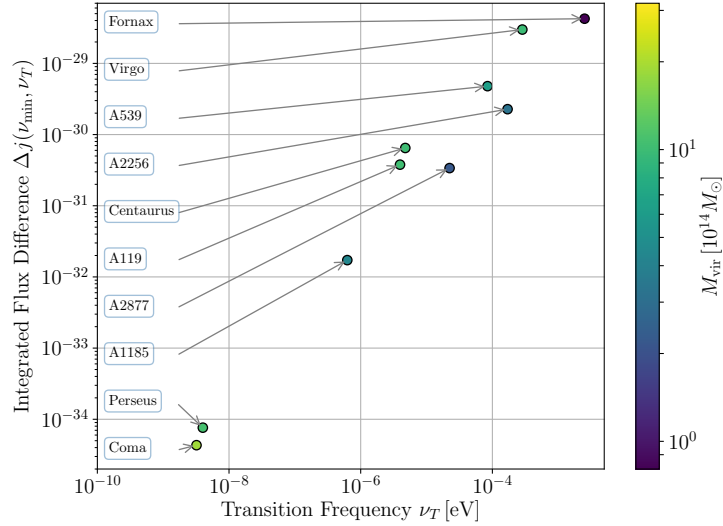


Figure 3.9: ν_T - $\Delta j(\nu_{\min}, \nu_T)$ relation for cross-correlated galaxy clusters in the simulation.

contribution can be negligible, or strong and will result in a negative $\Delta j(\nu_{\min}, \nu_T)$. For many massive galaxy clusters it is the case that $\Delta j(\nu_{\min}, \nu_T)$ will become negative after synchrotron emission was included, therefore reducing the sample down to 48.0% of the original number in sample \mathcal{A} . As it is displayed in Figure 3.10 (i), approximately one half of the clusters in sample \mathcal{A} disappeared. The remaining galaxy clusters are the ones with low M_{vir} , because their synchrotron emission is too low to eliminate the thermal AQN excess – it remains to be unanswered if this is due to a limited resolution or a physical background. For instance, it can be seen in Figure 3.10 (ii) that Fornax still remains to be the cluster with the largest $\Delta j(\nu_{\min}, \nu_T)$, however, Fornax might be less promising than expected, because it exhibits a relatively low number of CR particles and therefore does not fully reliable represent the actual real-world synchrotron emission. A safer potential candidate regarding this metric would therefore be Virgo, which is a relatively massive galaxy cluster exhibiting the second largest $\Delta j(\nu_{\min}, \nu_T)$.

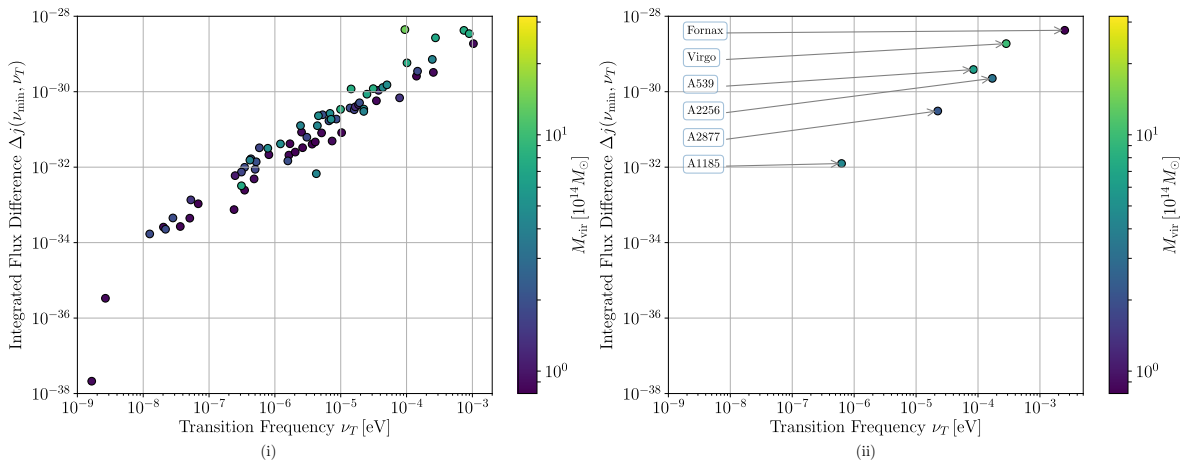


Figure 3.10: ν_T - $\Delta j(\nu_{\min}, \nu_T)$ relation including synchrotron radiation with thermal gas emission as background contamination. (i) sample \mathcal{A} and (ii) sample \mathcal{B} , both color-coded by M_{vir} . The y -range and colormap in (ii) are adapted to ranges of sample \mathcal{A} .

Cluster Name	M_{vir} [$10^{14} M_{\odot}$]	ν_T [eV]	$\Delta j_{\text{no synch}}$ [$\text{erg cm}^{-3} \text{s}^{-1}$]	$\Delta j_{\text{with synch}}$ [$\text{erg cm}^{-3} \text{s}^{-1}$]
Coma	18.82	3.21×10^{-9}	4.32×10^{-35}	X
Virgo	9.91	2.85×10^{-4}	2.99×10^{-29}	1.88×10^{-29}
Perseus	10.75	4.00×10^{-9}	7.62×10^{-35}	X
Centaurus	10.18	4.76×10^{-6}	6.48×10^{-31}	X
A119	10.21	3.96×10^{-6}	3.78×10^{-31}	X
A539	6.34	8.44×10^{-5}	4.79×10^{-30}	3.87×10^{-30}
A1185	4.42	6.26×10^{-7}	1.72×10^{-32}	1.25×10^{-32}
A2256	3.27	1.70×10^{-4}	2.27×10^{-30}	2.26×10^{-30}
A2877	2.22	2.24×10^{-5}	3.38×10^{-31}	3.08×10^{-31}
Norma	0.79	X	X	X
Fornax	0.61	2.51×10^{-3}	4.25×10^{-29}	4.25×10^{-29}

Table 3.1: Table of the cross-correlated galaxy clusters with physical properties from the simulation and their ability to show AQN signatures with and without synchrotron radiation in the background ($\Delta j_{\text{no synch}}$, $\Delta j_{\text{with synch}}$) at a transition frequency ν_T .

3.2.2 High Frequency Regime

Since non-thermal AQN emission is expected to show two intersections in the high energy regime, one has to define ν_{min} to be the first transition frequency where $j_{\text{AQN,nonthermal},\nu} > j_{\text{background},\nu}$ and ν_T is again where $j_{\text{AQN,nonthermal},\nu} < j_{\text{background},\nu}$ with the condition that $\nu_{\text{min}} < \nu_T$. Non-thermal AQN emission causing an excess over the background emission in the high energy regime is mostly dictated by the individual X-ray brightness of a galaxy cluster. Figure 3.5 shows that emission from the pion decay does not contaminate the background gas emission and the AQN emission, and AQN signatures can therefore be directly identified by strictly comparing gas emission versus the non-thermal AQN emission.

Figure 3.11 shows the only mass bin hosting galaxy clusters that exhibit an excess in the high energy regime due to non-thermal AQN emission.² In this image, dashed lines represent the Bremsstrahlung emission from the ICM and dash-dot-dotted lines are the non-thermal AQN emission. If there is an excess occurring, the signature is only very subtle and many low mass galaxy clusters are still too bright in X-rays in order to permit a window for non-thermal AQN emission to dominate.

In the following, the condition that non-thermal emission will be considered if any of the fluxes in the frequency bin is larger than the thermal Bremsstrahlung emission of the ICM. If that is the case, ν_T will then be saved for each galaxy cluster respectively again. After applying this condition, a ratio of 10% of remaining galaxy clusters proposes detections of non-thermal AQN signatures to be more challenging in galaxy clusters. Only 14 out of 15 points are visible in Figure 3.12, because two clusters with similar $\Delta j(\nu_{\text{min}}, \nu_T)$ were obtained at the same ν_T . This can happen, since the frequency resolution is 1000 bins and therefore different clusters with the same ν_T can populate similar integrated spectral differences.

As already indicated in Figure 3.11, galaxy clusters that exhibit an AQN excess reside on the lower side of the mass spectrum and it is therefore no surprise that the integrated thermal gas emission is also described by low values (Figure 3.12 (i)). Similar to thermal radiation, non-thermal AQN radiation scales according to Equation 2.43 and Equation 2.45 with

$$j_{\text{AQN,nonthermal},\nu} \sim n_{\text{AQN}} n_{\text{gas}} \Delta v, \quad (3.5)$$

for $R_{\text{eff}} = R_{\text{AQN}}$. In general, non-thermal AQN emission is weaker than thermal AQN

²High energy window spectra for other mass bins are displayed in Figure A.1.

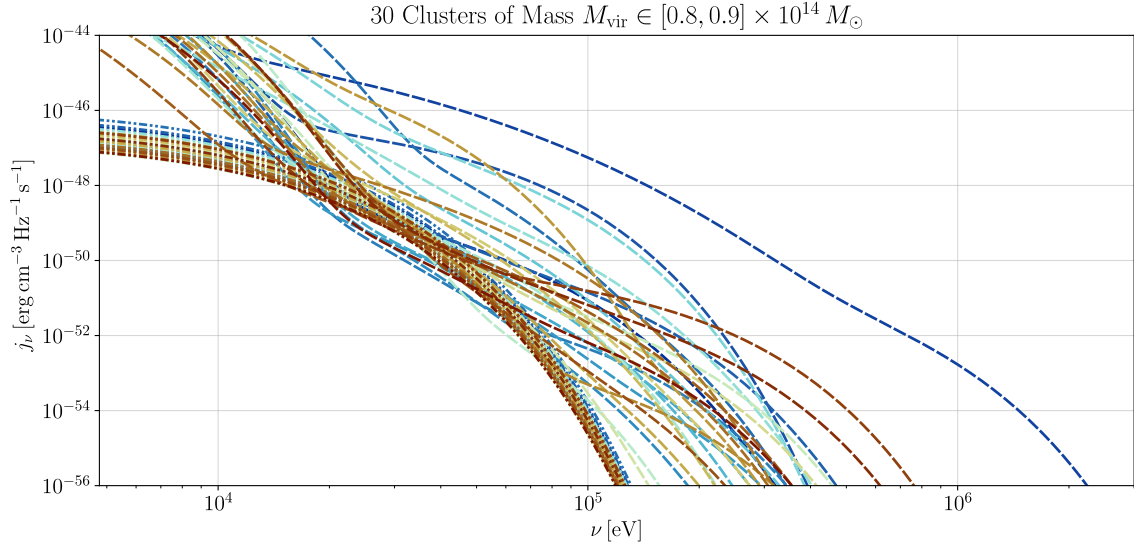


Figure 3.11: Spectral plot for non-thermal AQN emission and thermal Bremsstrahlung emission of the hot ICM. A small fraction of galaxy clusters shows small regions where AQN emission dominates gas emission.

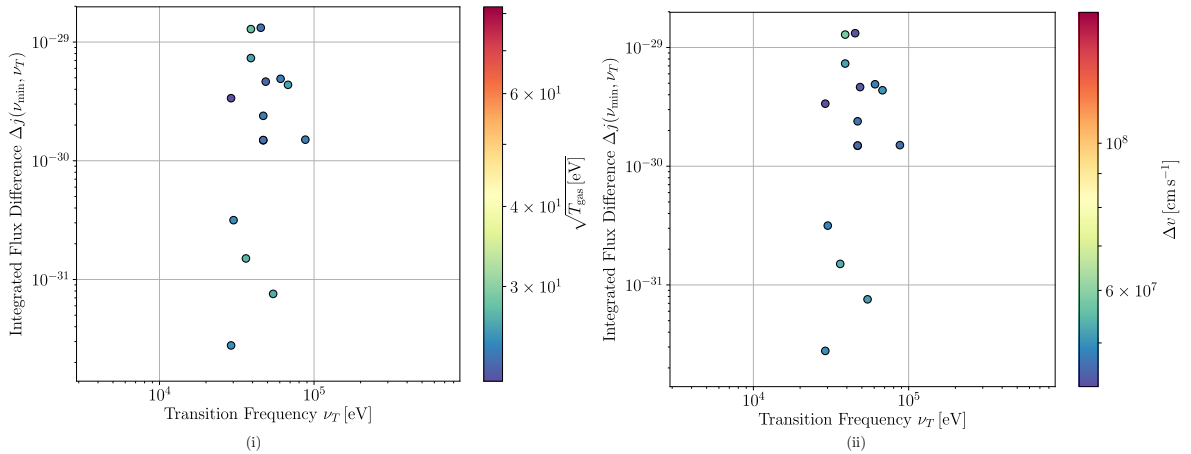


Figure 3.12: $\nu_T - \Delta j(\nu_{\min}, \nu_T)$ relation of galaxy clusters that fulfilled the conditions desired to identify an AQN signature in the high energy regime taken from sample \mathcal{A} , color-coded by (i) $\sqrt{T_{\text{gas}}}$ [eV] and (ii) Δv . Both plots show that galaxy clusters are populated in the lower parameter range.

emission (cf. Figure 3.5) – therefore, fewer clusters dominate in AQN over gas emission. Figure 3.12 shows that an excess is only possible for clusters with low T_{gas} . Δv appears to reside on lower values, but we have to keep in mind that we are considering the lowest mass bin and if we consider Figure 3.3, the intermediate values in Figure 3.12 are of the order of $\Delta v \sim 5 \times 10^7 \text{ cm s}^{-1}$. These relative velocities correspond to higher Δv in the respective lowest mass bin. It can therefore be concluded that an AQN excess is only caused by low brightness in the gas emission which comes from low cluster masses in a higher dynamical state of dark matter particles with respect to the surrounding gas particles. When applying the same methodology to sample \mathcal{B} , no cross-correlated counterpart can be found that showed an excess of AQNs in the high energy regime.

In conclusion, it shall be noted that the non-thermal emission model is not developed in great robustness yet and therefore cannot provide predictions with the same sturdiness as the thermal emission model of the AQNs. In future studies, the exponent of $1/3$ in Equation 2.42 for the frequency, will most likely be replaced by a free parameter β allowing to be adaptive.

The exponent of $1/3$ is an approximate solution to solve the synchrotron function (cf. [Equation 2.27](#)). It is crucial to note that particular solutions for the synchrotron function to model the non-thermal spectrum have to be motivated in greater detail and new precise models should aim for a more detailed physical implementation. In addition, the critical frequency as proposed in [Subsection 2.1.2](#) is set to 30 keV by convention and should be understood in an ‘order of magnitude estimate’ ([McNeil Forbes and Zhitnitsky, 2008a](#)). These estimates do not provide robust reference values as they suffer from an insufficiently refined theory of the non-thermal physics in the structure of AQNs due to an approximate treatment in the mean-field of the Maxwell equations. It is therefore not safe to discard the possibility to detect AQN signatures in the high energy regime immediately and a final conclusion shall be made once a better non-thermal AQN model is developed.

3.3 Cluster Maps

It is important to note that one loses information when only considering spectral features. Since AQNs spatially follow the halo distribution, positions of dark matter with respect to gas might slightly differ from each other. Extremely low emissions do not contribute to the spectrum, because j_ν was summed over all particles in the corresponding frequency bin, so spatial regions of low emission are not resolved in a spectrum. It is especially important for the gas emission to identify regions of low emissivity where AQN emission would be proficient to outshine thermal gas emission. It can even be possible to find an AQN excess in small regions in spatially resolved maps where one did not expect an excess only by considering the spectrum. On the other hand, it is not possible to look for excess features in all 167 galaxy clusters by finding their individual optimal region where AQN features dominate over the background emission, when scanning through a spectral resolution of 1000 frequency bins. We therefore stick to the methodology presented in [Equation 3.4](#) to analyze cluster regions, where AQN radiation certainly dominates in the spectrum by inferring the emission offset and only consider promising candidates of cross-correlated galaxy clusters.

Given this reasoning, in this section, SPH maps of gas and AQNs are represented using their most contributing physical properties and fluxes integrated over an adaptive best possible frequency range. [Figure 3.13](#) and [Figure 3.14](#) display the Fornax and Virgo cluster in ① AQN emission, integrated from ν_{\min} to ν_T , ② gas emission, integrated over the same frequency range, ③ difference images of AQN subtracted from the gas emission, ④ synchrotron emission, integrated from ν_{\min} to ν_T , ⑤ relative pressure, ⑥ AQN number density, ⑦ internal AQN temperature, ⑧ relative velocities of AQNs with respect to their surrounding gas environment and ⑨ the effective radius of AQNs, respectively. Relative pressure maps were obtained by generating SPH maps by utilizing the ideal gas relation $p_{\text{gas}} \sim n_{\text{gas}} T_{\text{gas}}$. Hence, the product of n_{gas} and T_{gas} will represent the scaling of the pressure in the gas particles and SPH maps were constructed this way. With the obtained pressure map, a Gaussian filter was applied to the projected bitmap of the galaxy cluster with $\sigma = 5$ in the Gaussian kernel. The relative pressure change is therefore obtained via:

$$\delta p = \frac{p_{\text{original}} - p_{\text{gaussian}}}{p_{\text{gaussian}}} \quad (3.6)$$

In Fornax (see [Figure 3.13](#)), less filamentary structures with strong emission are visible in thermal AQN emission compared to thermal gas emission, because dark matter is not affected by environmental friction effects that would perturb the particle distribution. Only small distinct regions with a strong AQN excess can be seen in the difference image and it is interesting to note that these regions are visible in the R_{eff} map as well.

Prominent regions of $R_{\text{eff}} > R_{\text{AQN}}$ are only possible if the gas environment provides the necessary parameter combination. Compared to other cross-correlated galaxy clusters (with

their SPH maps displayed in the appendix from [Figure A.2](#) to [Figure A.9](#)), it is quite rare to see large regions high R_{eff} values. The effective radius increments with increasing n_{gas} and Δv and decrements for increasing T_{gas} . T_{gas} scales with the largest exponent and therefore shows the strongest influence on R_{eff} . Radial profiles showed that especially in the central regions high gas temperatures can be reached. Fornax is a relatively small cluster with a comparable low thermal gas emission coming from a low T_{gas} . R_{eff} can therefore reach values of $R_{\text{eff}} > R_{\text{AQN}}$ in central regions, too. However, when comparing R_{eff} maps in Fornax to other cross-correlated clusters one can see that $R_{\text{eff}} > R_{\text{AQN}}$ values are more likely to find in the peripheries of galaxy clusters.

An intriguing physical property is that regions of $R_{\text{eff}} > 10^{-4}$ cm are typically not abundant in relative velocity maps, and it is especially in these regions where Δv seem to be lower compared to their nearest surroundings. Following $R_{\text{eff}} \sim n_{\text{gas}}^{5/7} \Delta v^{5/7} T_{\text{gas}}^{-17/7}$ (cf. [Equation 2.14](#)), gas overdensities in conjunction with low T_{gas} yield higher R_{eff} . In the case of Fornax, the prominent $R_{\text{eff}} > R_{\text{AQN}}$ -region is too close to the cluster center and will therefore be hotter than in the outskirts. In this case, n_{gas} would be the only free parameter that could directly influence R_{eff} .

Regions of high T_{AQN} do not necessarily follow the n_{AQN} distribution, since T_{AQN} is also influenced by the surrounding gas. Shocked regions are not significantly embedded in the AQN emission map and vice versa. A further interesting feature is that the AQN emission does not seem to show an significantly stronger abundance at extended regions. This is not trivial since dark matter particles do not suffer from friction and are not interacting other than with gravity in the simulation. Therefore, it would have been sensible to expect additional emission contributions in the periphery of Fornax that are not strongly present in the gas emission maps.

The Virgo cluster (see [Figure 3.14](#)) differs strongly from Fornax as it is more massive, hotter and in a more relaxed state. No signs of a current major merger are visible in the relative pressure maps (other than visible in Fornax with its prominent northern bow shock). And yet, both of these clusters independently show the strongest AQN excess. It is not obvious that shock features are no tracers for AQN emission as shocked regions are always accompanied by significant offsets in thermodynamic properties (such as for instance density or temperature). It was therefore expected that at least shocked regions will play a diminishing or reinforcing role on the AQN emission – in neither of the galaxy clusters this can be directly confirmed, and shock maps of other cross-correlated galaxy clusters do not show signs of shock signatures in the AQN maps either (see [Section A.2](#)).

In the difference image of the Virgo cluster one can see that regions of infalling substructures prominent in the gas maps are carved out and only regions without overdensities of galaxies are visible. This proposes the reasonable idea to look for AQN signatures where no galaxies are located when searching for signatures outside the center of the galaxy cluster – otherwise, it becomes apparent that the strongest offset of AQN signatures is located in its center (counterintuitively, this happens where the ICM shows the highest temperatures). Certainly, one of the reasons for a stronger excess in the central regions is given by the high relative velocity of AQN particles with respect to the gas. Interestingly enough, the n_{AQN} distribution shows a similar lenticular distribution as it is observed in the difference image. Since Virgo is more massive and more SPH particles are abundant, a higher CR resolution can be obtained leading to a non-negligible synchrotron radiation contribution one has to take into account.

In all cross-correlated galaxy clusters one can see that high Δv can be reached in the cluster's peripheries, too. The distribution of strong Δv appears to be anisotropic and AQN emission does not necessarily follow the distribution of high relative velocities on large scales.

In order to learn how AQN signatures evolve in bands of higher energies, individual energy ranges of five different instruments were taken. AQN and gas emission were integrated within

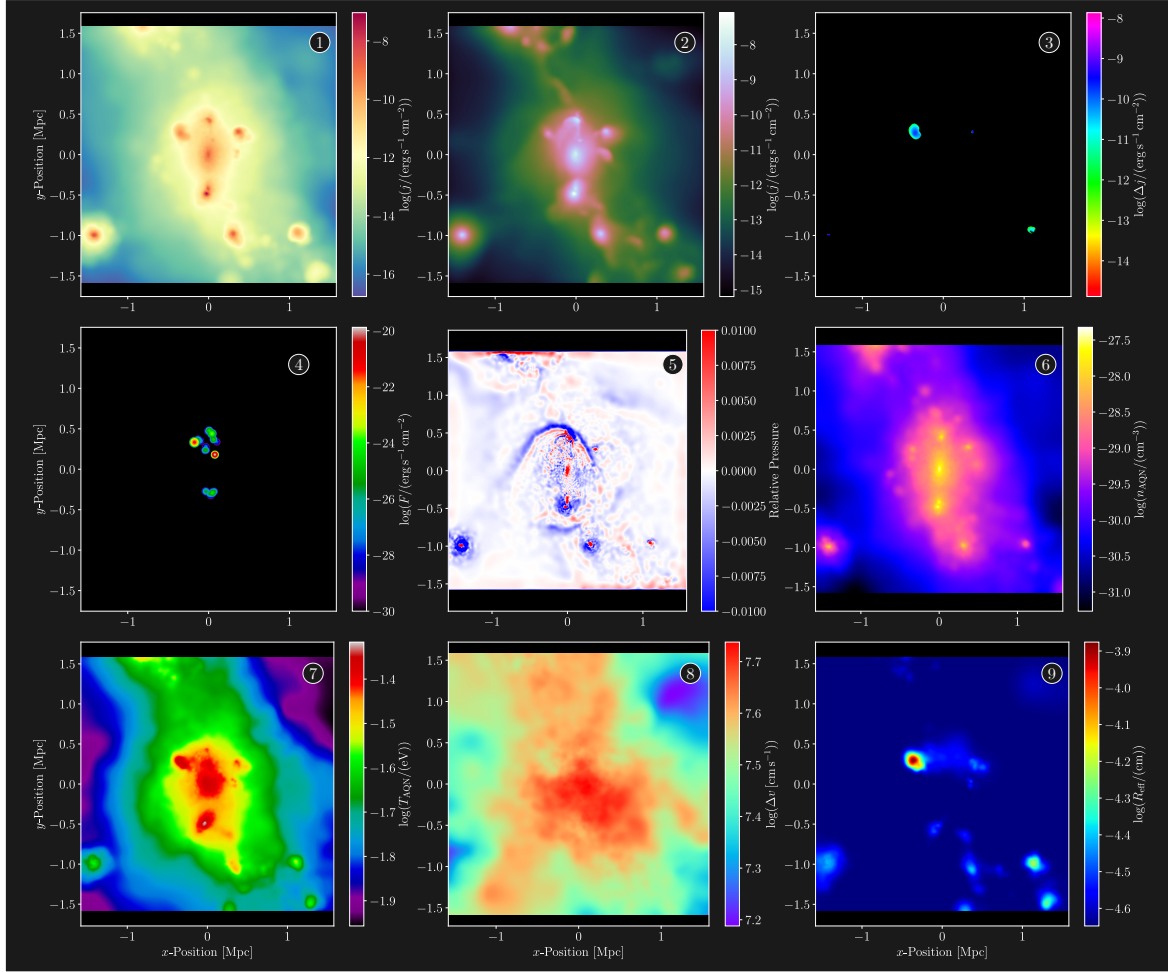


Figure 3.13: Cross-correlated Fornax cluster in all maps; (i) AQN Thermal emission from ν_{\min} to ν_T ; (ii) Thermal gas emission from ν_{\min} to ν_T ; (iii) Difference image from AQN and gas emission; (iv) Synchrotron emission from ν_{\min} to ν_T ; (v) Relative pressure of the ICM; (vi) AQN number density; (vii) Internal AQN temperature; (viii) Relative AQN-gas velocity; (ix) Effective AQN radius.

the respective energy ranges and AQN emission was superimposed by its thermal and non-thermal component. For the sake of a versatile energy coverage, the instruments LOFAR (van Haarlem et al., 2013), WMAP (Bennett et al., 2013), Planck (Tauber et al., 2010), Euclid (Laureijs et al., 2011) and XRISM (Mori et al., 2022) were considered. Table 3.2 shows the corresponding maximum energy range with upper and lower limits denoted by ν_{\min} and ν_{\max} for each instrument in units of eV.

	LOFAR	WMAP	Planck	Euclid	XRISM
ν_{\min} [eV]	4.14×10^{-8}	9.38×10^{-5}	1.24×10^{-4}	6.20×10^{-1}	4×10^2
ν_{\max} [eV]	9.93×10^{-7}	3.85×10^{-4}	3.54×10^{-3}	2.25	1.3×10^4

Table 3.2: Band-passes for LOFAR (van Haarlem et al., 2013), WMAP (Bennett et al., 2013), Planck (Tauber et al., 2010), Euclid (Laureijs et al., 2011) and XRISM (Mori et al., 2022) in units of eV.

In the following the two most promising galaxy clusters, determined by Figure 3.10 were selected for a multiband analysis. Figure 3.15 and Figure 3.16 show the gas and AQN emission with the corresponding difference image in the selected bands. In order to compare how the brightness of the emission evolves, all frames in their corresponding emission feature share the same colorbar limits. In each feature the minimum and maximum j was selected from all

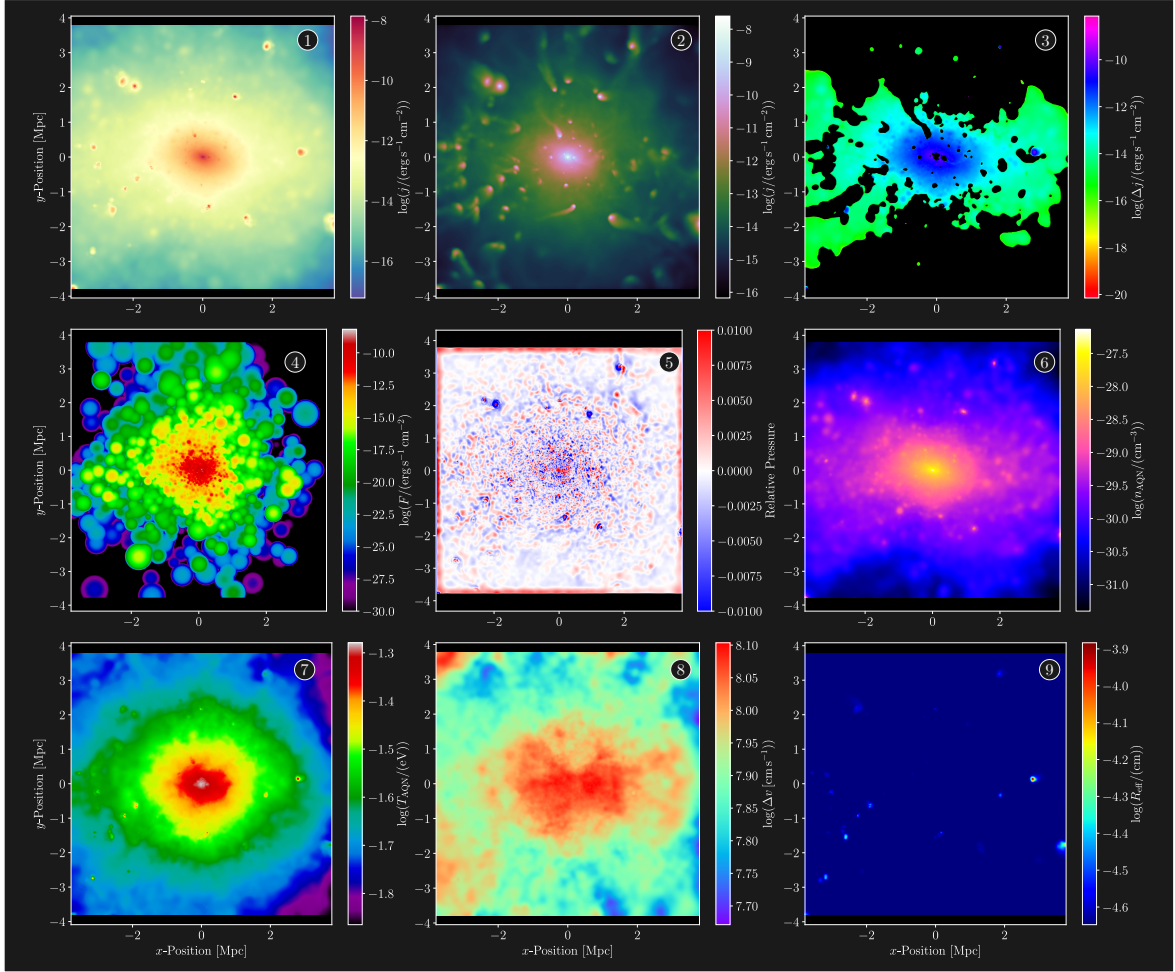


Figure 3.14: Cross-correlated Virgo cluster in all maps; (i) AQN Thermal emission from ν_{\min} to ν_T ; (ii) Thermal gas emission from ν_{\min} to ν_T ; (iii) Difference image from AQN and gas emission; (iv) Synchrotron emission from ν_{\min} to ν_T ; (v) Relative pressure of the ICM; (vi) AQN number density; (vii) Internal AQN temperature; (viii) Relative AQN-gas velocity; (ix) Effective AQN radius.

bands.

While the gas emission shows a continuing brightening for increasing band-energies, the AQN signatures shows a significant decrease in brightness in the Euclid band. This decrement originates from the spectral feature that thermal AQN emission transitions into the non-thermal regime. Euclid operates in the energy range, where the thermal emission experiences its cutoff (cf. Figure 3.5). Even though AQN signatures show a rebrightening once the non-thermal regime takes over, AQN emission cannot compete with the thermal gas emission in the X-ray regime. It is visible in the difference images in the third row that AQN emission would only be able to dominate in the low energy regime. In the difference images of LOFAR, WMAP, and Planck, an interesting feature emerges: the surface area of positive values decreases with increasing energies across the frequency range; however, smaller regions exhibit larger offsets of Δj .

It can be concluded that Euclid and XRISM are the least promising instruments for a potential AQN signature detection as the gas outshines the AQN emission in this energy range. LOFAR, WMAP, and Planck, exhibit AQN signatures in the difference images, even when synchrotron emission is included. Due to a limited CR resolution, almost no synchrotron emission seems to impact the difference image in the Fornax cluster, whereas minimal tracers of synchrotron emission can be seen in the difference image for Virgo. No clear spatial trend can be pinpointed, where AQNs are most likely to dominate the background emission.

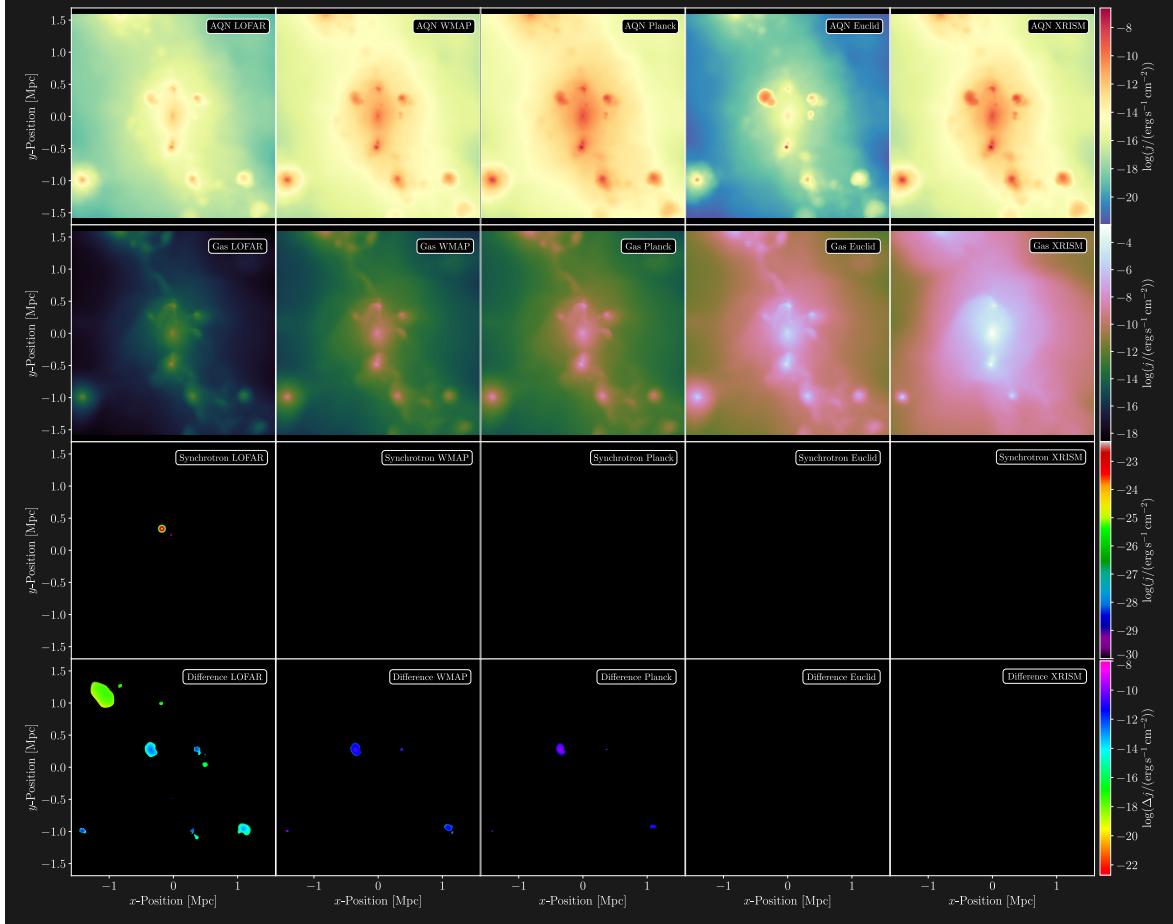


Figure 3.15: Fornax cluster AQN, gas and synchrotron emission generated from LOFAR, WMAP, Planck, Euclid and XRISM energy ranges. Only minimal synchrotron emission is abundant in LOFAR bands, which results in almost no impact on the difference images. Higher energies than in the LOFAR range show no synchrotron emission. Gas completely outshines AQN emission in Euclid and XRISM energies.

3.4 Observational Feasibility of Promising Cluster Candidates

It came clear in [Section 3.3](#) that spatial features of strong AQN signatures are hard to identify and differ from cluster to cluster. Even though AQN emission excess is abundant in galaxy clusters, it becomes challenging to pinpoint regions of clusters that are expected to be the most promising.

In observations, galaxy cluster emissions are typically analyzed by radial profiles in a given frequency band. This approach enables to identify important spatial features that are dependent on distance and the corresponding frequency band. In this section radial profiles will be shown for the cross-correlated galaxy clusters that show an excess signature of thermal AQN emission integrated over their individual frequency bands from ν_{\min} to ν_T . Radial profiles in 50 bins were taken for each individual emission property and a final radial profile was calculated after summing the AQN, gas and synchrotron maps.

[Figure 3.17](#) shows how the cross-correlated galaxy clusters evolve in emission over a radius of $r \in [10^{-2}, 1.5] r_{200}$. Averaged over a radial profile, the gas emission mostly shows larger values of j compared to the thermal AQN emission. In all galaxy clusters strong variations of synchrotron emissions can be seen due to their different masses. The AQN and gas emission profiles similarly decrease for increasing radii while sharing multiple morphological features in the radial profiles. Similar radial emission profiles of AQN and gas are observed due

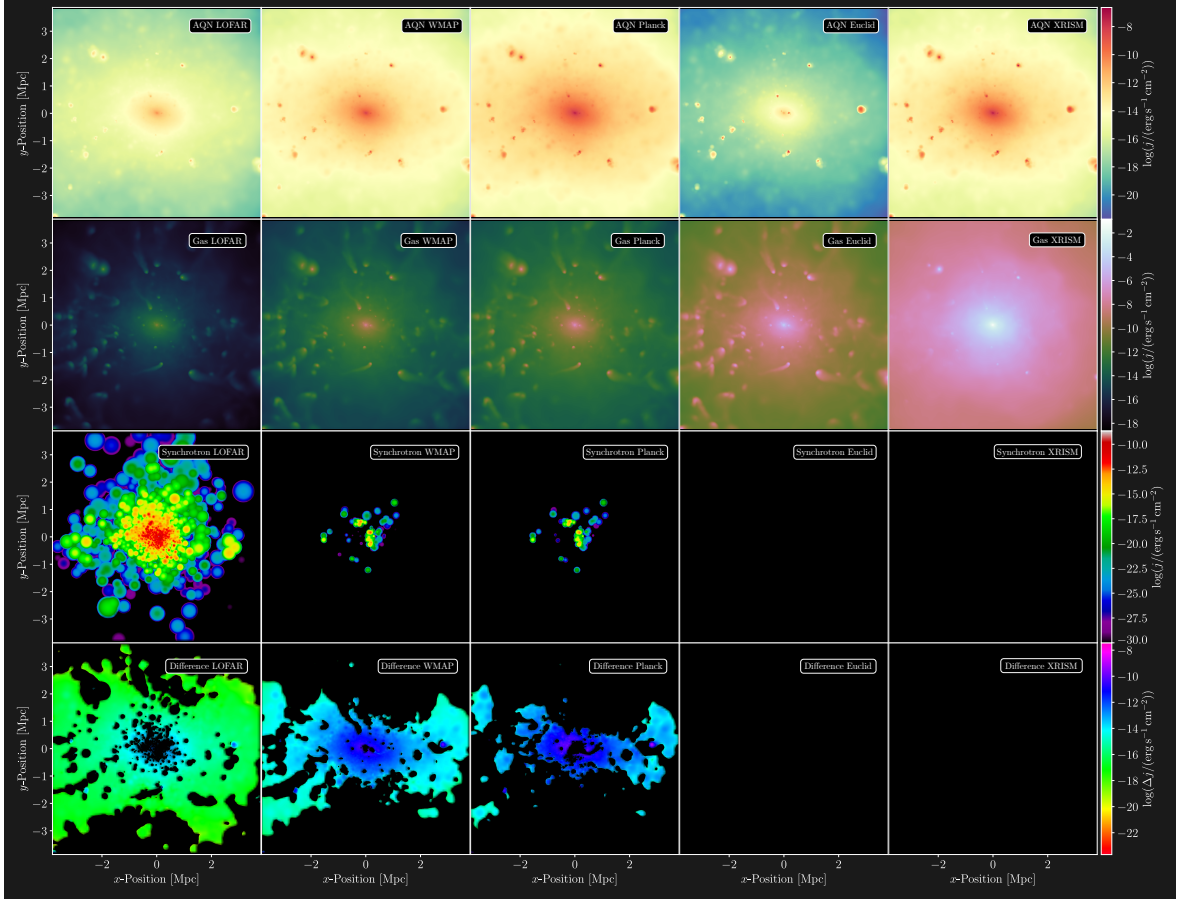


Figure 3.16: Virgo cluster AQN, gas and synchrotron emission generated from LOFAR, WMAP, Planck, Euclid and XRISM energy ranges. Synchrotron emission is abundant in LOFAR, WMAP and Planck bands, which in return shows a slight impact on the difference images. Higher energies than in the Planck range show no synchrotron emission. Gas completely outshines AQN emission in Euclid and XRISM energies.

to the fact that AQNs are predominantly characterized by gas features. Despite the strong radial similarity of AQN and gas, no specific trend that can be attributed to AQNs only. Furthermore, no strong radial excesses in the AQN emission can be determined in all the cross-correlated galaxy clusters.

Even though the overlaid radial profile shows an increment due to AQN emission, it is not possible to predict where to look for AQN signatures in the radial profiles of real observations. It appears that a general increment of the total emission of a galaxy cluster can be attributed to AQN properties. However, the constant radially independent shift towards marginal higher emissions will not permit a possible detection of AQNs in the radial profiles, even though their existence might be reasonable and a signal might be abundant.

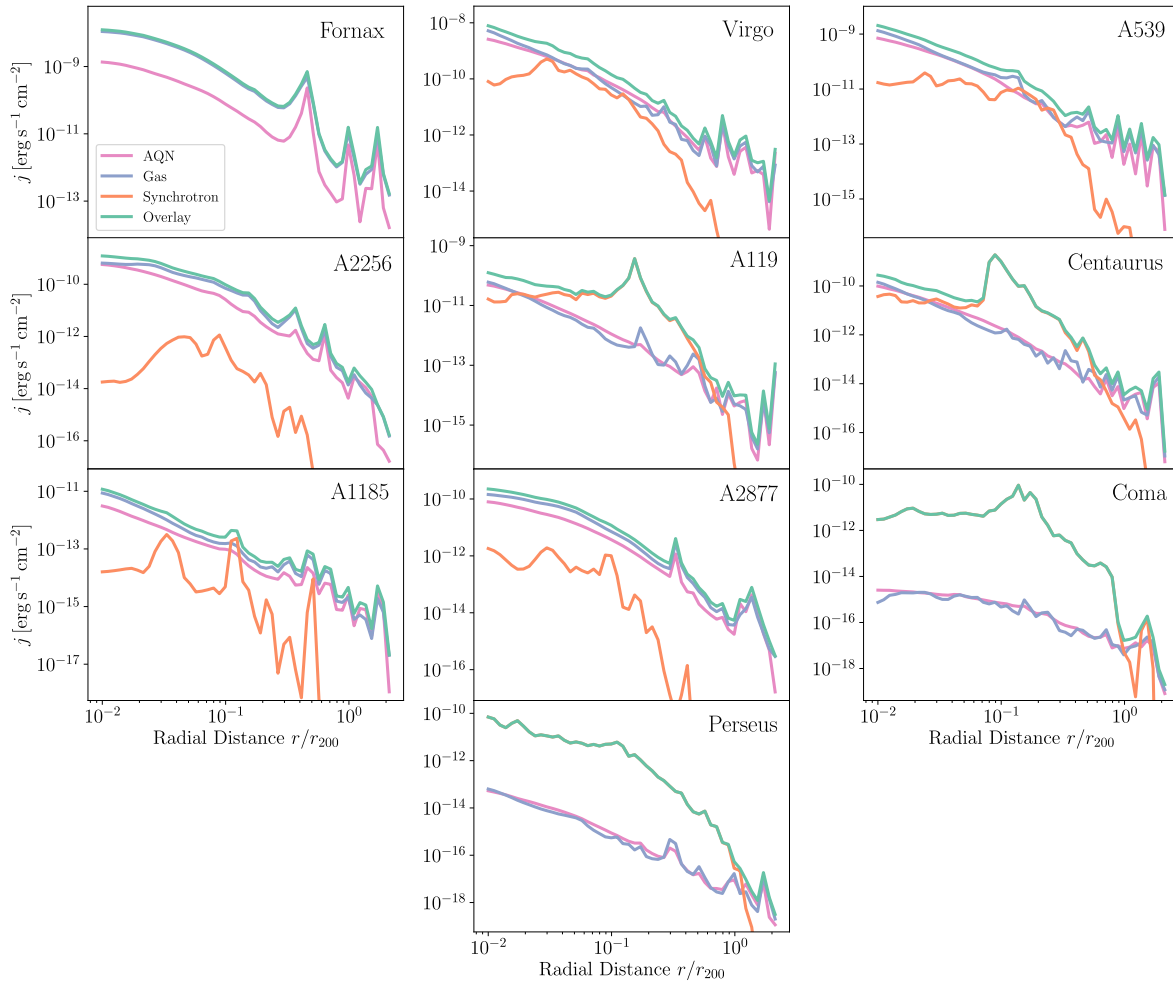


Figure 3.17: Radial profiles for cross-correlated galaxy clusters that showed a thermal AQN emission excess in spectral features. AQN emission was compared to gas, synchrotron and a superimposed, overlaid emission of gas and synchrotron obtained after integrating from ν_{\min} to the individual ν_T .

Chapter 4

Discussion

4.1 Comments on Observationally Motivated Phenomena

Numerical analysis of AQNs in galaxy clusters in a cosmological simulation have shown that direct signatures of this new dark matter model can be challenging to pinpoint. To assess it on the whole, the most important outcomes of this study will be emphasized. In [Section 1.4](#), tracers of AQN signatures and further unexplained observational phenomena were pointed out that were analyzed by various studies, which will be discussed in the following paragraphs in consideration of the underlying results of this thesis.

First we address the possible source for a strong signal in the 21 cm absorption line: they claim that at a redshift of $z = 17$ during the early universe, AQN emission could be responsible for a signal at 90 MHz (see [Lawson and Zhitnitsky \(2019\)](#)). Clusters of galaxies did not form at this time yet and early protoclusters – observationally confirmed to be progenitors of present-day galaxy clusters – are detected at $z \sim 6 - 7$ ([Harikane et al., 2019](#)). We therefore cannot assume the same conditions for the AQN increment which was obtained in the framework of this thesis. However, it is worth mentioning that protoclusters at $z \sim 7$ could be capable to influence the radio background, if the AQN signal would be similarly significant as in galaxy clusters at present-time. The total emission increment in the radial profiles of cross-correlated galaxy clusters at $z = 0$ can be attributed to $\Delta j_{\text{tot}} \approx 21.24\%$ thermal AQN emission only, when calculating:

$$\Delta j_{\text{tot}} = \frac{1}{N_{\text{clusters}}} \sum_{i=1}^{N_{\text{clusters}}} \frac{\sum_{k=1}^{N_{\text{bins}}} j_{\text{AQN},k}^i}{\sum_{k=1}^{N_{\text{bins}}} j_{\text{AQN},k}^i + \sum_{k=1}^{N_{\text{bins}}} j_{\text{gas},k}^i + \sum_{k=1}^{N_{\text{bins}}} j_{\text{synch},k}^i}. \quad (4.1)$$

It is however important to mention that early clusters possess different physical properties ([Chiang et al., 2013](#), [Overzier, 2016](#)), which would likely yield different AQN signatures. Results from this study only provided information of AQN signatures from cluster properties at $z = 0$. It would be sensible to implement AQN features already in snapshots at higher redshift and implement a dynamical AQN-treatment, in order to grasp a full evolution of AQN signatures from early to present-time galaxy clusters that could contribute to the background radio emission.

The study by [Zhitnitsky \(2022b\)](#) analyzed the diffuse galactic UV radiation and suggested that hot AQNs with $T_{\text{AQN}} \sim 5 \text{ eV}$ could reproduce such observations – however, since our study focuses on scales of galaxy clusters and not galactic scales, we cannot verify these predictions. The same argumentation is applied to the proposal to the contribution of Chandra’s diffuse 8 keV emission by AQNs ([McNeil Forbes and Zhitnitsky, 2008a](#)). However, it is worth commenting that in a galaxy cluster it is rather unlikely to find AQNs with temperatures of 5 eV because of the suppression of capturing protons in the hot ICM. Galactic environments differ strongly from galaxy cluster environments with different T_{gas} , n_{gas} , n_{DM} and Δv as the ISM is cooler and denser as the ICM. In addition, galaxies exhibit a significantly lower gas

emission and especially non-thermal AQN emission in the high energy regime might indeed be capable of dominating highly energetic galactic background emission.

It is not possible to comment predictions on the 511 keV as predicted by Oaknin and Zhitnitsky (2005), Zhitnitsky (2007), Forbes et al. (2010), Flambaum and Samsonov (2021) as we did not consider e^+e^- annihilation lines in our approach.

In Section 3.3, AQN emission was studied for different instruments in their corresponding bands. While this thesis focused on AQN properties in galaxy cluster environments rather than properties within the Milky Way, a direct comparison to McNeil Forbes and Zhitnitsky (2008b) cannot be conducted. Nevertheless, it is striking to observe the abundance of AQN signatures in the WMAP maps depicted in Figure 3.15 and Figure 3.16. A positive AQN signature in the WMAP band-pass can be identified even after including synchrotron background emission from the CRs as it can be seen in the difference images. While it is important to interpret the results with caution given the significant differences between cluster and galactic properties, the possibility of an excess in microwaves in the galactic core due to AQN emission may not be entirely unfounded.

Even though it is not the scope of this work to verify the predictions regarding seasonal X-ray variations (see Ge et al. (2022)), we would like to provide a brief comment on the relative velocities of gas to dark matter particles that are an integral assumption for the study by Ge et al. (2022). As it can be seen for example in Figure 3.13 and Figure 3.14, Δv can vary in region. It is not the aim of this work to question their assumptions, but it is important that relative velocities on large scales can differ in direction and magnitude and it is rather unlikely that Δv would follow a well-ordered pattern on galactic scales.

An excess in the \sim keV regime of galaxy clusters, as it was proposed by Bulbul et al. (2014) might indeed be a possibility to consider. However, given the fact that the physics non-thermal emission processes of AQNs are not sufficiently developed yet, it would not be sensible to trust the excess obtained in the high energy regime in this underlying work. In addition, Gonzalez Villalba (2024) pointed out that calibration issues can yield an excess of nonphysical origin. The effective areas of XMM and Chandra have ‘ripples’ in the 3 – 4 keV regime. If calibration routines did not account for these ripples properly, observations can show unidentified line features if the signal-to-noise ratio is too high. The discrepancy in CCD-based telescopes can even be seen in temperature measurements of galaxy clusters (Migkas et al., 2024).

Chapter 5

Outlook

In this outlook the most important key results are summarized, followed suggestions on possible follow-up studies starting with the recommendations that would directly improve the outcomes of this work and closing this chapter with a less conservative speculation on possible outcomes of an enhanced magnetized AQN model.

5.1 Key Results

- ① As it was pointed out numerous times throughout this work, ω_c and β have to be refined in order to properly model non-thermal emission processes in AQNs.
- ② Even though more massive galaxy clusters typically exhibit higher ICM temperatures, the largest population of high R_{eff} can be observed for the most massive mass bin in sample \mathcal{A} as Δv scales with cluster mass as well. This is an interesting feature, since T_{AQN} directly scales with R_{eff} and the AQN emission highly depends on T_{AQN} . Consequently, strong AQN emission can be expected for massive galaxy clusters. The increased AQN emission, however, is always accompanied by high cluster gas emission, as thermal gas emission of the ICM scales with cluster gas temperatures as well. To some degree, relative emission domination is therefore equilibrated for higher cluster masses.
- ③ Median AQN properties for each galaxy cluster show a strong mass dependence. While median Δv and T_{gas} equally increase with cluster mass, T_{gas} will become less important for T_{AQN} since it only plays a role in environments where $\kappa > 1$. The highest median T_{AQN} were reached in sample \mathcal{A} for densest galaxy clusters that showed relatively similar Δv .
- ④ A strong AQN emission offset does not scale with the mass of a galaxy cluster in the low energy regime. For a fixed ν_T , however, T_{gas} and Δv are the most dominant factors of influence for strong $\Delta j(\nu_{\text{min}}, \nu_T)$ for different galaxy cluster masses.
- ⑤ On the other hand, a strong AQN emission offset does scale with the mass of a galaxy cluster in the high energy regime. Only the smallest galaxy clusters showed a small excess of non-thermal AQN emission.
- ⑥ A strong reduction of galaxy clusters with nonzero $\Delta j(\nu_{\text{min}}, \nu_T)$ from 91.3% to 48.0% is observed when synchrotron emission from CRs is included. Given this inclusion, galaxy clusters only survive when the synchrotron emission is sufficiently low. However, it is not possible to predict if the remaining 48.0% are of physical nature or due to limited CR tracer particle resolution. It was pointed out that the remaining galaxy clusters can

be assigned to low mass galaxy clusters, making the presence for nonzero $\Delta j(\nu_{\min}, \nu_T)$ presumably of numerical nature.

- ⑦ With a small amount of galaxy clusters exhibiting large values of ν_T enable to conduct follow-up observations in a wider range of possible surveys. Fornax hosts an environment that is responsible for an extremely high transition frequency of $\nu_T = 2.51 \times 10^{-3}$ eV, which ranges almost up to infrared frequencies. In order to make use of this feature that is naturally embedded in the thermal emission property of AQNs, improvements on pinpointing regions in galaxy clusters that can only be attributed to an AQN emission excess are required.
- ⑧ Shock features are no tracers for regions of strong AQN emission.
- ⑨ The spatial distribution of Δv in the SPH maps is not strongly correlated with AQN emission signatures.
- ⑩ A suitable compromise for the Virgo cluster seems to lie within a frequency range where synchrotron emission is not overly dominant, yet a significant excess attributed to AQN emission is evident. This range corresponds to $\nu \in [9.38 \times 10^{-5}, 3.85 \times 10^{-4}]$ eV, which aligns with the band-pass of WMAP. Within this range, AQN signatures are observable in both central and peripheral regions of the cluster. The Virgo cluster was chosen for analysis due to its notable $\Delta j(\nu_{\min}, \nu_T)$, ranking second highest among background gas and synchrotron emission, while maintaining adequate resolution for CR particle detection.
- ⑪ Even though a general increase of emission in the radial profiles can be attributed to AQN signatures, it is hard to identify specific regions that only trace AQN signatures, since radial AQN emission profiles share a similar morphology as gas emission profiles. We assumed the model to be true and showed that AQN emission affects the spectrum and is visible in the emission maps. The AQN-background emission offset, however, is so small that it is not possible to verify or discard this dark matter model observationally, even though it might be one of the most promising ones.
- ⑫ An additional important insight that was aimed to be achieved was to identify promising galaxy cluster, where a detection of AQN signatures might be possible. Here we propose Virgo as a suitable candidate as it is the cluster with the second largest $\Delta j(\nu_{\min}, \nu_T)$ in the low energy regime with a high CR tracer particle resolution. It is therefore rather unlikely that synchrotron emission would outshine a possible AQN signature in this cluster. It is still important to mention that even for the most promising candidate no special features could be pointed out that would definitely hint towards a distinctive trace of AQNs.

These key findings show that this exotic model to explain dark matter cannot be discarded and simultaneously proposes many new different opportunities to test and verify the predicted outcomes of AQNs. Even though the signal is minimal, the best outcomes of a strong AQN excess resulted in the Virgo cluster in a frequency range of $\nu \in [1.45, 5.92] \times 10^{-5}$ eV. The results of this work are by no means definite, as the theory of AQNs is under ongoing evolution and improvements for robustness. As final remarks we would like to propose additional AQN features that would improve the physics and the pertaining feasibility to discover signatures in the following chapter.

5.2 Future Work

First of all, our study was constrained to regions enclosing a radius of $1.5 r_{200}$ for sample \mathcal{A} and $1.5 r_{\text{vir}}$ for sample \mathcal{B} . This provides first valuable insights on expectable AQN signatures from the innermost regions. However, it is expected that especially in the peripheries of galaxy clusters – more specifically in the warm-hot intergalactic medium – the environmental gas temperature of $T_{\text{gas}} \in [10^5, 10^7]$ K (Davé et al., 2001) may permit a better detection of AQN signatures. Lower gas temperatures and number densities would yield a lower thermal emission. On the other hand, a lower number density of gas and AQNs would play a decremting role in peripheral AQN excess detections. In general, AQN signals are expected to be weaker in the outskirts of galaxy clusters as it was already pointed out in the radial profiles of this thesis. Simultaneously, the background emission polluting the AQN signature would decrease as well and both of the emissions will probably fall below the detection limit. However, it is still important to study outskirts of galaxy clusters for tracers of AQNs, for example in simulations, in order to confirm or discard possible non-detection predictions. In order to improve the robustness of synchrotron emission from CRs, it is highly advised to increase the resolution, which can be conducted, for example, in zoom-in simulations.

Furthermore, we did not use a mass and size distribution for AQNs throughout this study and set every AQN to a size of $R_{\text{AQN}} = 2.25 \times 10^{-5}$ cm and a mass of $M_{\text{AQN}} = 16.7$ g. Of course, this is a simplification that is not expected in the real world (see for example Ge et al. (2019)). It is reasonable to assume the utilized R_{AQN} and M_{AQN} as a rough reference value in an analysis conducted for a single snapshot at $z = 0$ from the cosmological simulation. However, it would also be sensible to implement an on-the-fly model for AQNs directly evolving in a cosmological simulation. This would imply different halo distributions due to dynamical friction of differently massive AQN particles, leading to a segregation of more massive AQNs in the central regions of galaxy clusters and probably influencing the radial dark matter density profiles, too. Consequently, not only density profiles would be altered by a constant influence of AQNs on the cluster environment throughout time. Annihilation and heating processes of AQNs would result in feedback mechanisms that act directly on the ICM. Therefore, temperature profiles in galaxy clusters would be influenced too, if the AQN model in the simulation would be treated dynamically. An additional consequence would be that the heated ICM will become visible as tail-like traces behind substructures that fall towards the center of the galaxy cluster. Tails of galaxies are already detected in radio observations (Vallee, 1988, Sun et al., 2005, Terni de Gregory et al., 2017, Chen et al., 2020, de Vos et al., 2021, Hu et al., 2021, Müller et al., 2021, Pal and Kumari, 2023) and are mostly attributed to AGN feedback mechanisms and ram-pressure stripping. Constant gas interactions with an infalling subhalo would cause similar effects that are recommended to be verified in a dynamical AQN treatment in the simulation. A suitable AQNs mass distribution would therefore be reasonable if on-the-fly AQN models are implemented in the simulations.

Throughout this thesis, the similarity between AQNs and neutron stars was pointed out multiple times, as both objects are expected to host cores in a CS state – the same connection can be drawn with respect to magnetars. It is assumed that strong magnetic fields of magnetized neutron stars can be established if the core is ferromagnetic with nuclear density. We therefore propose the following question: why should quark nuggets not be ferromagnetic too?¹ A solid foundation of the model for magnetized quark nuggets (MQNs) and predictions were developed over the years in for example VanDevender et al. (2020a,b, 2021b), Sloan et al. (2021), VanDevender et al. (2021a, 2024). Following these studies, an MQN is a ferromagnetic liquid of nuclear density. The system itself will generate a magnetic dipole of with a field strength of $B_0 \simeq 1.65 \pm 0.35 \times 10^{12}$ T = $1.65 \pm 0.35 \times 10^{16}$ G (VanDevender et al., 2021b,

¹A pioneer on magnetized quark nuggets is J. Pace VanDevender who described his idea in a short video on <https://mqncollaboration.com/>.

2024). These studies anticipate that the strong magnetic field is what makes MQNs stable over cosmic time.

If MQNs exist, interesting implications on features for galaxy clusters and observations would follow from their properties. First, MQNs would propose an additional source for magnetic fields in galaxy clusters as multiple MQNs could possibly form – when aligned – a large magnetic field, and MQNs as additional magnetic field sources are not far-fetched. Various sources can contribute to magnetic fields in galaxy clusters, with some reasonable magnetic field sources in the ICM being for instance normal galaxies, starburst galaxies, active galactic nuclei and primordial magnetic fields generated prior to recombination (Grasso and Rubinstein, 2001, Carilli and Taylor, 2002, Govoni and Feretti, 2004). Second, if MQNs propagated through the ICM, electrons will be accelerated by their strong magnetic fields due to an additional Lorentz force component. Since MQNs could be aligned to form large scale magnetic fields, they could further act as a Faraday rotating medium of polarised synchrotron emission from the ICM. Since no studies were found addressing these large scale implications of MQNs, these features are purely of speculative nature, and it is important to verify if these implications hold true or not by conducting analysis from simulations and observations.

The physical effects of a magnetisation in quark composites serving as dark matter is that their effective radius would be influenced by the surrounding magnetic field. Furthermore, studies show that the strong magnetic field in MQNs influences the interaction with the surrounding plasma as each MQN would develop a magnetopause that causes them to lose kinetic energy while moving through the plasma (VanDevender et al., 2017, 2020a). This would have the effect that dark matter halos of substructures in galaxy clusters would experience a frictional component. By estimating an on-the-fly stopping power effect for a dark matter halo, it would be possible to observe a change in the radial dark matter profiles. On the other hand, the aforementioned studies focused on magnetized quark nuggets with a different composition in the quark core and slightly different properties than axion quark nuggets. Santillán and Sempé (2020) studied magnetic effects specifically for quark nuggets that contain an axion domain wall in their structure and suggest that once an axion domain wall is present, a ferromagnetic state cannot be established. They concluded, however, that this state might be possible for ordinary matter nuggets.

In conclusion, the general theory of AQNs and similar derivations of this model yield physically interesting outcomes. It is remarkable that the AQN model was initially introduced as a consequence of a solution for the \mathcal{CP} problem. Long-lived cosmological problems are in return naturally resolved by this model. Observable features propose predictions that can be validated by numerical methods as we showed throughout this study. This work serves as a first foundation to show that observable AQN features can be studied in cluster environments using cosmological simulations. Many outcomes that were summarized in the discussion, and it was proposed that AQN signatures might not be impossible to find. Can AQN signatures be expected using the underlying thermal and non-thermal AQN emission model in cluster environments? Yes and no. They might be abundant and could positively contribute to the emission spectrum of galaxy clusters. However, incorporating our approach, it is not possible to disentangle pure AQN contributions from the radiation background in galaxy clusters and we need improved strategies and more sophisticated models to learn more about possible AQN signatures. Until further improvements on the model of axion quark nuggets and their dynamical implementation in cosmological simulations are established, the mysterious dark matter will remain to be dark.

Bibliography

- Abbasi, R.U. et al. The bursts of high energy events observed by the telescope array surface detector. *Physics Letters A*, 381(32):2565–2572, August 2017. doi: 10.1016/j.physleta.2017.06.022.
- Abbott, L.F. and Sikivie, P. A cosmological bound on the invisible axion. *Physics Letters B*, 120(1-3):133–136, January 1983. doi: 10.1016/0370-2693(83)90638-X.
- Afshordi, N., McDonald, P. and Spergel, D.N. Primordial Black Holes as Dark Matter: The Power Spectrum and Evaporation of Early Structures. *Astrophysical Journal, Letters*, 594(2):L71–L74, September 2003. doi: 10.1086/378763.
- Alcock, C. et al. Possible gravitational microlensing of a star in the Large Magellanic Cloud. *Nature*, 365(6447):621–623, October 1993. doi: 10.1038/365621a0.
- Alcock, C. et al. EROS and MACHO Combined Limits on Planetary-Mass Dark Matter in the Galactic Halo. *Astrophysical Journal, Letters*, 499(1):L9–L12, May 1998. doi: 10.1086/311355.
- Alford, M.G. et al. Color superconductivity in dense quark matter. *Reviews of Modern Physics*, 80(4):1455–1515, October 2008. doi: 10.1103/RevModPhys.80.1455.
- Bartelmann, M. and Steinmetz, M. A Comparison of X-ray and Strong Lensing Properties of Simulated X-ray Clusters. *Monthly Notices of the RAS*, 283(2):431–446, November 1996. doi: 10.1093/mnras/283.2.431.
- Bashkanov, M. and Watts, D.P. A new possibility for light-quark dark matter. *Journal of Physics G Nuclear Physics*, 47(3):03LT01, February 2020. doi: 10.1088/1361-6471/ab67e8.
- Belfatto, B. et al. Dark Matter abundance via thermal decays and leptoquark mediators. *Journal of High Energy Physics*, 2022(6):84, June 2022. doi: 10.1007/JHEP06(2022)084.
- Bennett, C.L. et al. Nine-year Wilkinson Microwave Anisotropy Probe (WMAP) Observations: Final Maps and Results. *Astrophysical Journal, Supplement*, 208(2):20, October 2013. doi: 10.1088/0067-0049/208/2/20.
- Beznosko, D. et al. Horizon-T experiment and detection of Extensive air showers with unusual structure. In *Journal of Physics Conference Series*, volume 1342 of *Journal of Physics Conference Series*, page 012007, January 2020. doi: 10.1088/1742-6596/1342/1/012007.
- Binney, J. and Tremaine, S. *Galactic dynamics*. 1987.
- Blum, K., Sato, R. and Waxman, E. Cosmic-ray Antimatter. *arXiv e-prints*, art. arXiv:1709.06507, September 2017. doi: 10.48550/arXiv.1709.06507.
- Böss, L.M. LudwigBoess/SPHtoGrid.jl: v0.4.5, August 2023.
- Böss, L.M. and Valenzuela, L.M. LudwigBoess/GadgetIO.jl: v0.7.12, November 2023.

- Böss, L.M., Steinwandel, U.P. and Dolag, K. A Formation Mechanism for “Wrong Way” Radio Relics. *Astrophysical Journal, Letters*, 957(2):L16, November 2023a. doi: 10.3847/2041-8213/ad03f7.
- Böss, L.M. et al. CRESCENDO: an on-the-fly Fokker-Planck solver for spectral cosmic rays in cosmological simulations. *Monthly Notices of the RAS*, 519(1):548–572, February 2023b. doi: 10.1093/mnras/stac3584.
- Boyarisky, A. et al. Constraints on sterile neutrinos as dark matter candidates from the diffuse X-ray background. *Monthly Notices of the RAS*, 370(1):213–218, July 2006. doi: 10.1111/j.1365-2966.2006.10458.x.
- Bryan, G.L. and Norman, M.L. Statistical Properties of X-Ray Clusters: Analytic and Numerical Comparisons. *Astrophysical Journal*, 495(1):80–99, March 1998. doi: 10.1086/305262.
- Budker, D., Flambaum, V.V. and Zhitnitsky, A. Infrasonic, Acoustic and Seismic Waves Produced by the Axion Quark Nuggets. *Symmetry*, 14(3):459, February 2022. doi: 10.3390/sym14030459.
- Bulbul, E. et al. Detection of an Unidentified Emission Line in the Stacked X-Ray Spectrum of Galaxy Clusters. *Astrophysical Journal*, 789(1):13, July 2014. doi: 10.1088/0004-637X/789/1/13.
- Carilli, C.L. and Taylor, G.B. Cluster Magnetic Fields. *Annual Review of Astron and Astrophys*, 40:319–348, January 2002. doi: 10.1146/annurev.astro.40.060401.093852.
- Carlsson, K. et al. KristofferC/NearestNeighbors.jl: v0.4.13, December 2022.
- Carr, B., Kühnel, F. and Sandstad, M. Primordial black holes as dark matter. *Physical Review D*, 94(8):083504, October 2016. doi: 10.1103/PhysRevD.94.083504.
- Carroll, B.W. and Ostlie, D.A. *An Introduction to Modern Astrophysics*. Cambridge University Press, 2 edition, 2017.
- Chang, S., Haggmann, C. and Sikivie, P. Studies of the motion and decay of axion walls bounded by strings. *Physical Review D*, 59(2):023505, December 1998. doi: 10.1103/PhysRevD.59.023505.
- Chen, H. et al. The ram pressure stripped radio tails of galaxies in the Coma cluster. *Monthly Notices of the RAS*, 496(4):4654–4673, August 2020. doi: 10.1093/mnras/staa1868.
- Chiang, Y.K., Overzier, R. and Gebhardt, K. Ancient Light from Young Cosmic Cities: Physical and Observational Signatures of Galaxy Proto-clusters. *Astrophysical Journal*, 779(2):127, December 2013. doi: 10.1088/0004-637X/779/2/127.
- Colalillo, R. The observation of lightning-related events with the Surface Detector of the Pierre Auger Observatory. In *European Physical Journal Web of Conferences*, volume 197 of *European Physical Journal Web of Conferences*, page 03003, September 2019. doi: 10.1051/epjconf/201919703003.
- Crusius, A. and Schlickeiser, R. Synchrotron radiation in random magnetic fields. *Astronomy and Astrophysics*, 164(2):L16–L18, August 1986.
- Davé, R. et al. Baryons in the Warm-Hot Intergalactic Medium. *Astrophysical Journal*, 552(2):473–483, May 2001. doi: 10.1086/320548.
- de Rujula, A. and Glashow, S.L. Nuclearites—a novel form of cosmic radiation. *Nature*, 312(5996):734–737, December 1984. doi: 10.1038/312734a0.

- de Vos, K. et al. Clusters' far-reaching influence on narrow-angle tail radio galaxies. *Monthly Notices of the RAS*, 506(1):L55–L58, September 2021. doi: 10.1093/mnrasl/slab075.
- Dehnen, W. and Aly, H. Improving convergence in smoothed particle hydrodynamics simulations without pairing instability. *Monthly Notices of the RAS*, 425(2):1068–1082, September 2012. doi: 10.1111/j.1365-2966.2012.21439.x.
- Dimopoulos, S. and Susskind, L. Baryon number of the universe. *Physical Review D*, 18(12):4500–4509, December 1978. doi: 10.1103/PhysRevD.18.4500.
- Dine, M. and Fischler, W. The not-so-harmless axion. *Physics Letters B*, 120(1-3):137–141, January 1983. doi: 10.1016/0370-2693(83)90639-1.
- Dine, M., Fischler, W. and Srednicki, M. A simple solution to the strong CP problem with a harmless axion. *Physics Letters B*, 104(3):199–202, August 1981. doi: 10.1016/0370-2693(81)90590-6.
- Dobler, G. and Finkbeiner, D.P. Extended Anomalous Foreground Emission in the WMAP Three-Year Data. *Astrophysical Journal*, 680(2):1222–1234, June 2008. doi: 10.1086/587862.
- Dolag, K. et al. Simulation Techniques for Cosmological Simulations. *Space Science Reviews*, 134(1-4):229–268, February 2008. doi: 10.1007/s11214-008-9316-5.
- Dolag, K. et al. Substructures in hydrodynamical cluster simulations. *Monthly Notices of the RAS*, 399(2):497–514, October 2009. doi: 10.1111/j.1365-2966.2009.15034.x.
- Dolag, K. et al. Simulating the LOcal Web (SLOW). I. Anomalies in the local density field. *Astronomy and Astrophysics*, 677:A169, September 2023. doi: 10.1051/0004-6361/202346213.
- Donnert, J.M.F. et al. Magnetic field evolution in giant radio relics using the example of CIZA J2242.8+5301. *Monthly Notices of the RAS*, 462(2):2014–2032, October 2016. doi: 10.1093/mnras/stw1792.
- Enßlin, T.A., Lieu, R. and Biermann, P.L. Non-thermal origin of the EUV and HEX excess emission of the Coma cluster - the nature of the energetic electrons. *Astronomy and Astrophysics*, 344:409–420, April 1999. doi: 10.48550/arXiv.astro-ph/9808139.
- Farhi, E. and Jaffe, R.L. Strange matter. *Physical Review D*, 30(11):2379–2390, December 1984. doi: 10.1103/PhysRevD.30.2379.
- Felten, J.E. et al. X-rays from the Coma Cluster of Galaxies. In *Quasars and high-energy astronomy*, page 279, January 1969.
- Feng, C. and Holder, G. Enhanced Global Signal of Neutral Hydrogen Due to Excess Radiation at Cosmic Dawn. *Astrophysical Journal, Letters*, 858(2):L17, May 2018. doi: 10.3847/2041-8213/aac0fe.
- Finkbeiner, D.P. WMAP Microwave Emission Interpreted as Dark Matter Annihilation in the Inner Galaxy. *arXiv e-prints*, art. astro-ph/0409027, September 2004a. doi: 10.48550/arXiv.astro-ph/0409027.
- Finkbeiner, D.P. Microwave Interstellar Medium Emission Observed by the Wilkinson Microwave Anisotropy Probe. *Astrophysical Journal*, 614(1):186–193, October 2004b. doi: 10.1086/423482.

- Finkbeiner, D.P., Langston, G.I. and Minter, A.H. Microwave Interstellar Medium Emission in the Green Bank Galactic Plane Survey: Evidence for Spinning Dust. *Astrophysical Journal*, 617(1):350–359, December 2004. doi: 10.1086/425165.
- Flambaum, V.V. and Samsonov, I.B. Radiation from matter-antimatter annihilation in the quark nugget model of dark matter. *Physical Review D*, 104(6):063042, September 2021. doi: 10.1103/PhysRevD.104.063042.
- Flambaum, V.V. and Zhitnitsky, A.R. Primordial lithium puzzle and the axion quark nugget dark matter model. *Physical Review D*, 99(2):023517, January 2019. doi: 10.1103/PhysRevD.99.023517.
- Fleury, L. and Moore, G.D. Axion dark matter: strings and their cores. *Journal of Cosmology and Astroparticle Physics*, 2016(1):004–004, January 2016. doi: 10.1088/1475-7516/2016/01/004.
- Forbes, M.M., Lawson, K. and Zhitnitsky, A.R. Electrosphere of macroscopic “quark nuclei”: A source for diffuse MeV emissions from dark matter. *Physical Review D*, 82(8):083510, October 2010. doi: 10.1103/PhysRevD.82.083510.
- Fouka, M. and Ouichaoui, S. Analytical fits for the synchrotron emission from a power-law particle distribution with a sharp cutoff. *Monthly Notices of the RAS*, 442(2):979–994, August 2014. doi: 10.1093/mnras/stu922.
- Fouka, M. and Ouichaoui, S. Analytical fits to the synchrotron functions. *Research in Astronomy and Astrophysics*, 13(6):680–686, June 2013. doi: 10.1088/1674-4527/13/6/007.
- Frampton, P.H. et al. Primordial black holes as all dark matter. *Journal of Cosmology and Astroparticle Physics*, 2010(4):023, April 2010. doi: 10.1088/1475-7516/2010/04/023.
- Fraser, G.W. et al. Potential solar axion signatures in X-ray observations with the XMM-Newton observatory. *Monthly Notices of the RAS*, 445(2):2146–2168, December 2014. doi: 10.1093/mnras/stu1865.
- Ge, S., Liang, X. and Zhitnitsky, A. Cosmological C P -odd axion field as the coherent Berry’s phase of the Universe. *Physical Review D*, 96(6):063514, September 2017. doi: 10.1103/PhysRevD.96.063514.
- Ge, S., Lawson, K. and Zhitnitsky, A. Axion quark nugget dark matter model: Size distribution and survival pattern. *Physical Review D*, 99(11):116017, June 2019. doi: 10.1103/PhysRevD.99.116017.
- Ge, S. et al. Impulsive radio events in quiet solar corona and axion quark nugget dark matter. *Physical Review D*, 102(12):123021, December 2020. doi: 10.1103/PhysRevD.102.123021.
- Ge, S. et al. X-ray annual modulation observed by XMM-Newton and Axion Quark Nugget dark matter. *Physics of the Dark Universe*, 36:101031, June 2022. doi: 10.1016/j.dark.2022.101031.
- Gelmini, G.B., Osoba, E. and Palomares-Ruiz, S. Inert-sterile neutrino: Cold or warm dark matter candidate. *Physical Review D*, 81(6):063529, March 2010. doi: 10.1103/PhysRevD.81.063529.
- Gonzalez Villalba, J.A. Stacking the spectra of eROSITA galaxy cluster data for searches of the 3.5keV line: Dark matter decay or charge exchange? *arXiv e-prints*, art. arXiv:2401.00923, January 2024. doi: 10.48550/arXiv.2401.00923.

- Gorghetto, M., Hardy, E. and Villadoro, G. Axions from strings: the attractive solution. *Journal of High Energy Physics*, 2018(7):151, July 2018. doi: 10.1007/JHEP07(2018)151.
- Gorham, P.W. et al. Characteristics of Four Upward-Pointing Cosmic-Ray-like Events Observed with ANITA. *Physical Review Letters*, 117(7):071101, August 2016. doi: 10.1103/PhysRevLett.117.071101.
- Gorham, P.W. et al. Observation of an Unusual Upward-Going Cosmic-Ray-like Event in the Third Flight of ANITA. *Physical Review Letters*, 121(16):161102, October 2018. doi: 10.1103/PhysRevLett.121.161102.
- Gorham, P.W. et al. Unusual Near-Horizon Cosmic-Ray-like Events Observed by ANITA-IV. *Physical Review Letters*, 126(7):071103, February 2021. doi: 10.1103/PhysRevLett.126.071103.
- Govoni, F. and Feretti, L. Magnetic Fields in Clusters of Galaxies. *International Journal of Modern Physics D*, 13(8):1549–1594, January 2004. doi: 10.1142/S0218271804005080.
- Grasso, D. and Rubinstein, H.R. Magnetic fields in the early Universe. *Physics Reports*, 348(3):163–266, July 2001. doi: 10.1016/S0370-1573(00)00110-1.
- Green, A.M. and Kavanagh, B.J. Primordial black holes as a dark matter candidate. *Journal of Physics G Nuclear Physics*, 48(4):043001, April 2021. doi: 10.1088/1361-6471/abc534.
- Harikane, Y. et al. SILVERRUSH. VIII. Spectroscopic Identifications of Early Large-scale Structures with Protoclusters over 200 Mpc at $z \sim 6-7$: Strong Associations of Dusty Star-forming Galaxies. *Astrophysical Journal*, 883(2):142, October 2019. doi: 10.3847/1538-4357/ab2cd5.
- Henry, R.C. et al. The Mystery of the Cosmic Diffuse Ultraviolet Background Radiation. *Astrophysical Journal*, 798(1):14, January 2015. doi: 10.1088/0004-637X/798/1/14.
- Hernández-Martínez, E. et al. Simulating the Local Web (SLOW) – II: Properties of local galaxy clusters. *arXiv e-prints*, art. arXiv:2402.01834, February 2024. doi: 10.48550/arXiv.2402.01834.
- Hillas, A.M. Cosmic Rays: Recent Progress and some Current Questions. *arXiv e-prints*, art. astro-ph/0607109, July 2006. doi: 10.48550/arXiv.astro-ph/0607109.
- Hooper, D. et al. Prospects for detecting dark matter with GLAST in light of the WMAP haze. *Physical Review D*, 77(4):043511, February 2008. doi: 10.1103/PhysRevD.77.043511.
- Hu, D. et al. The Merger Dynamics of the Galaxy Cluster A1775: New Insights from Chandra and XMM-Newton for a Cluster Simultaneously Hosting a Wide-angle Tail and a Narrow-angle Tail Radio Source. *Astrophysical Journal*, 913(1):8, May 2021. doi: 10.3847/1538-4357/abf09e.
- Hui, L. et al. Ultralight scalars as cosmological dark matter. *Physical Review D*, 95(4):043541, February 2017. doi: 10.1103/PhysRevD.95.043541.
- Jean, P. et al. Spectral analysis of the Galactic e^+e^- annihilation emission. *Astronomy and Astrophysics*, 445(2):579–589, January 2006. doi: 10.1051/0004-6361:20053765.
- Kawasaki, M., Saikawa, K. and Sekiguchi, T. Axion dark matter from topological defects. *Physical Review D*, 91(6):065014, March 2015. doi: 10.1103/PhysRevD.91.065014.
- Kim, J.E. Weak-interaction singlet and strong CP invariance. *Physical Review Letters*, 43(2):103–107, July 1979. doi: 10.1103/PhysRevLett.43.103.

- Klaer, V.B. and Moore, G.D. The dark-matter axion mass. *Journal of Cosmology and Astroparticle Physics*, 2017(11):049, November 2017. doi: 10.1088/1475-7516/2017/11/049.
- Knödlseher, J. et al. Early SPI/INTEGRAL constraints on the morphology of the 511 keV line emission in the 4th galactic quadrant. *Astronomy and Astrophysics*, 411:L457–L460, November 2003. doi: 10.1051/0004-6361:20031437.
- Kolb, E.W. and Turner, M.S. Grand unified theories and the origin of the baryon asymmetry. *Annual Review of Nuclear and Particle Science*, 33:645–696, January 1983. doi: 10.1146/annurev.ns.33.120183.003241.
- Kolb, E.W. and Turner, M.S. *The early universe*, volume 69. 1990.
- Kuksa, V. and Beylin, V. Heavy Quark Symmetry and Fine Structure of the Spectrum of Hadronic Dark Matter. *Symmetry*, 12(11):1906, November 2020. doi: 10.3390/sym12111906.
- Kumar, P., Lu, W. and Bhattacharya, M. Fast radio burst source properties and curvature radiation model. *Monthly Notices of the RAS*, 468(3):2726–2739, July 2017. doi: 10.1093/mnras/stx665.
- Lacroix, T. et al. Predicting the dark matter velocity distribution in galactic structures: tests against hydrodynamic cosmological simulations. *Journal of Cosmology and Astroparticle Physics*, 2020(10):031, October 2020. doi: 10.1088/1475-7516/2020/10/031.
- Laureijs, R. et al. Euclid Definition Study Report. *arXiv e-prints*, art. arXiv:1110.3193, October 2011. doi: 10.48550/arXiv.1110.3193.
- Lawson, K. and Zhitnitsky, A.R. The 21 cm absorption line and the axion quark nugget dark matter model. *Physics of the Dark Universe*, 24:100295, March 2019. doi: 10.1016/j.dark.2019.100295.
- Lawson, K. and Zhitnitsky, A.R. Diffuse cosmic gamma rays at 1-20 MeV: a trace of the dark matter? *Journal of Cosmology and Astroparticle Physics*, 2008(1):022, January 2008. doi: 10.1088/1475-7516/2008/01/022.
- Lawson, K. et al. Gravitationally trapped axions on the Earth. *Physical Review D*, 100(4):043531, August 2019. doi: 10.1103/PhysRevD.100.043531.
- Lee, B.W. and Weinberg, S. Cosmological lower bound on heavy-neutrino masses. *Physical Review Letters*, 39(4):165–168, July 1977. doi: 10.1103/PhysRevLett.39.165.
- Liang, X. *Dark matter in the form of axion quark nuggets: formation, detections, and evidence*. PhD thesis, University of British Columbia, 2022. URL <https://open.library.ubc.ca/collections/ubctheses/24/items/1.0418614>.
- Liang, X. and Zhitnitsky, A. Axion field and the quark nugget’s formation at the QCD phase transition. *Physical Review D*, 94(8):083502, October 2016. doi: 10.1103/PhysRevD.94.083502.
- Liang, X. and Zhitnitsky, A. Telescope array bursts, radio pulses and axion quark nuggets. *European Physical Journal C*, 82(3):249, March 2022a. doi: 10.1140/epjc/s10052-022-10208-0.
- Liang, X. and Zhitnitsky, A. ANITA anomalous events and axion quark nuggets. *Physical Review D*, 106(6):063022, September 2022b. doi: 10.1103/PhysRevD.106.063022.
- Lu, W. and Kumar, P. On the radiation mechanism of repeating fast radio bursts. *Monthly Notices of the RAS*, 477(2):2470–2493, June 2018. doi: 10.1093/mnras/sty716.

- Majidi, F. et al. On the detectability of the Axion Quark Nugget Dark Matter in Large Scale Structures. in prep.
- Martin, D.C. et al. The Galaxy Evolution Explorer: A Space Ultraviolet Survey Mission. *Astrophysical Journal, Letters*, 619(1):L1–L6, January 2005. doi: 10.1086/426387.
- McNeil Forbes, M. and Zhitnitsky, A.R. Diffuse x-rays: directly observing dark matter? *Journal of Cosmology and Astroparticle Physics*, 2008(1):023, January 2008a. doi: 10.1088/1475-7516/2008/01/023.
- McNeil Forbes, M. and Zhitnitsky, A.R. WMAP haze: Directly observing dark matter? *Physical Review D*, 78(8):083505, October 2008b. doi: 10.1103/PhysRevD.78.083505.
- Migkas, K. et al. The SRG/eROSITA All-Sky Survey: SRG/eROSITA cross-calibration with Chandra and XMM-Newton using galaxy cluster gas temperatures. *arXiv e-prints*, art. arXiv:2401.17297, January 2024. doi: 10.48550/arXiv.2401.17297.
- Mohr, J.J., Mathiesen, B. and Evrard, A.E. Properties of the Intracluster Medium in an Ensemble of Nearby Galaxy Clusters. *Astrophysical Journal*, 517(2):627–649, June 1999. doi: 10.1086/307227.
- Mondal, S., Oberoi, D. and Mohan, A. First Radio Evidence for Impulsive Heating Contribution to the Quiet Solar Corona. *Astrophysical Journal, Letters*, 895(2):L39, June 2020. doi: 10.3847/2041-8213/ab8817.
- Mori, K. et al. Xtend, the soft x-ray imaging telescope for the X-Ray Imaging and Spectroscopy Mission (XRISM). In den Herder, J.W.A., Nikzad, S. and Nakazawa, K., editors, *Space Telescopes and Instrumentation 2022: Ultraviolet to Gamma Ray*, volume 12181 of *Society of Photo-Optical Instrumentation Engineers (SPIE) Conference Series*, page 121811T, August 2022. doi: 10.1117/12.2626894.
- Müller, A. et al. Two striking head-tail galaxies in the galaxy cluster IIZW108: insights into transition to turbulence, magnetic fields, and particle re-acceleration. *Monthly Notices of the RAS*, 508(4):5326–5344, December 2021. doi: 10.1093/mnras/stab2928.
- Muno, M.P. et al. Diffuse X-Ray Emission in a Deep Chandra Image of the Galactic Center. *Astrophysical Journal*, 613(1):326–342, September 2004. doi: 10.1086/422865.
- Navarro, J.F., Frenk, C.S. and White, S.D.M. Simulations of X-ray clusters. *Monthly Notices of the RAS*, 275(3):720–740, August 1995. doi: 10.1093/mnras/275.3.720.
- Nielsen, H.B. and Froggatt, C.D. Dusty Dark Matter Pearls Developed. *arXiv e-prints*, art. arXiv:2303.06061, March 2023. doi: 10.48550/arXiv.2303.06061.
- Oaknin, D.H. and Zhitnitsky, A.R. 511 keV Photons from Color Superconducting Dark Matter. *Physical Review Letters*, 94(10):101301, March 2005. doi: 10.1103/PhysRevLett.94.101301.
- Okuda, T. Telescope Array observatory for the high energy radiation induced by lightning. In *Journal of Physics Conference Series*, volume 1181 of *Journal of Physics Conference Series*, page 012067, February 2019. doi: 10.1088/1742-6596/1181/1/012067.
- Overzier, R.A. The realm of the galaxy protoclusters. A review. *Astronomy and Astrophysics Reviews*, 24(1):14, November 2016. doi: 10.1007/s00159-016-0100-3.
- Pal, S. and Kumari, S. A new catalog of head-tail radio galaxies from LoTSS DR1. *Journal of Astrophysics and Astronomy*, 44(1):17, June 2023. doi: 10.1007/s12036-022-09892-x.

- Palade, D.I. and Pomârjanschi, L.M. Approximations of the modified Bessel functions of the second kind K_ν . Applications in random field generation. *arXiv e-prints*, art. arXiv:2303.13400, March 2023. doi: 10.48550/arXiv.2303.13400.
- Peccei, R.D. and Quinn, H.R. Constraints imposed by CP conservation in the presence of pseudoparticles. *Physical Review D*, 16(6):1791–1797, September 1977. doi: 10.1103/PhysRevD.16.1791.
- Planck Collaboration et al. Planck 2013 results. XVI. Cosmological parameters. *Astronomy and Astrophysics*, 571:A16, November 2014. doi: 10.1051/0004-6361/201321591.
- Preskill, J., Wise, M.B. and Wilczek, F. Cosmology of the invisible axion. *Physics Letters B*, 120(1-3):127–132, January 1983. doi: 10.1016/0370-2693(83)90637-8.
- Primack, J.R., Seckel, D. and Sadoulet, B. Detection of cosmic dark matter. *Annual Review of Nuclear and Particle Science*, 38(38):751–807, January 1988. doi: 10.1146/annurev.ns.38.120188.003535.
- Raza, N., Van Waerbeke, L. and Zhitnitsky, A. Solar corona heating by axion quark nugget dark matter. *Physical Review D*, 98(10):103527, November 2018. doi: 10.1103/PhysRevD.98.103527.
- Reinhardt, M. Missing Mass and the Gravitational Lense Effect. *Astronomy and Astrophysics*, 12:196, May 1971.
- Rybicki, G.B. and Lightman, A.P. *Radiative Processes in Astrophysics*. 1986.
- Santillán, O.P. and Sempé, M. Electric and magnetic axion quark nuggets, their stability and their detection. *European Physical Journal C*, 80(5):466, May 2020. doi: 10.1140/epjc/s10052-020-8027-2.
- Sarazin, C.L. X-ray emission from clusters of galaxies. *Reviews of Modern Physics*, 58(1): 1–115, January 1986. doi: 10.1103/RevModPhys.58.1.
- Seidel, M. Approximate integrals of synchrotron radiation spectra. 10 2003.
- Seljak, U. et al. Can Sterile Neutrinos Be the Dark Matter? *Physical Review Letters*, 97(19): 191303, November 2006. doi: 10.1103/PhysRevLett.97.191303.
- Sheth, R.K. and Diaferio, A. Peculiar velocities of galaxies and clusters. *Monthly Notices of the RAS*, 322(4):901–917, April 2001. doi: 10.1046/j.1365-8711.2001.04202.x.
- Shi, X. and Fuller, G.M. New Dark Matter Candidate: Nonthermal Sterile Neutrinos. *Physical Review Letters*, 82(14):2832–2835, April 1999. doi: 10.1103/PhysRevLett.82.2832.
- Sikivie, P. Axions, Domain Walls, and the Early Universe. *Physical Review Letters*, 48(17): 1156–1159, April 1982. doi: 10.1103/PhysRevLett.48.1156.
- Sloan, T. et al. Magnetised quark nuggets in the atmosphere. *Scientific Reports*, 11:22432, November 2021. doi: 10.1038/s41598-021-01658-9.
- Springel, V. et al. Populating a cluster of galaxies - I. Results at $z=0$. *Monthly Notices of the RAS*, 328(3):726–750, December 2001. doi: 10.1046/j.1365-8711.2001.04912.x.
- Strong, A.W., Moskalenko, I.V. and Reimer, O. Diffuse Continuum Gamma Rays from the Galaxy. *Astrophysical Journal*, 537(2):763–784, July 2000. doi: 10.1086/309038.

- Sun, M., Jerius, D. and Jones, C. A Small X-Ray Corona of the Narrow-Angle Tail Radio Galaxy NGC 1265 Soaring through the Perseus Cluster. *Astrophysical Journal*, 633(1): 165–173, November 2005. doi: 10.1086/452620.
- Tanuma, S. et al. Two-dimensional Magnetohydrodynamic Numerical Simulations of Magnetic Reconnection Triggered by a Supernova Shock in the Interstellar Medium: Generation of X-Ray Gas in the Galaxy. *Astrophysical Journal*, 551(1):312–332, April 2001. doi: 10.1086/320058.
- Tauber, J.A. et al. Planck pre-launch status: The Planck mission. *Astronomy and Astrophysics*, 520:A1, September 2010. doi: 10.1051/0004-6361/200912983.
- Terni de Gregory, B. et al. Narrow head-tail radio galaxies at very high resolution. *Astronomy and Astrophysics*, 608:A58, December 2017. doi: 10.1051/0004-6361/201730878.
- Testa, P., Saar, S.H. and Drake, J.J. Stellar activity and coronal heating: an overview of recent results. *Philosophical Transactions of the Royal Society of London Series A*, 373 (2042):20140259–20140259, April 2015. doi: 10.1098/rsta.2014.0259.
- Thejappa, G. A Self-Consistent Model for the Storm Radio Emission from the Sun. *Solar Physics*, 132(1):173–193, March 1991. doi: 10.1007/BF00159137.
- Tully, R.B. et al. Cosmicflows-2: The Data. *Astronomical Journal*, 146(4):86, October 2013. doi: 10.1088/0004-6256/146/4/86.
- Vallee, J.P. The 1-MEGAPARSEC Giant Head / Tail Radio Galaxy IC711 - 3-DIMENSIONAL Simulation and Additional Constraints on the Ram Pressure Theory. *Astrophysics and Space Science*, 149(2):225–231, November 1988. doi: 10.1007/BF00639792.
- van Haarlem, M.P. et al. LOFAR: The LOW-Frequency ARray. *Astronomy and Astrophysics*, 556:A2, August 2013. doi: 10.1051/0004-6361/201220873.
- Van Waerbeke, L. and Zhitnitsky, A. Fast radio bursts and the axion quark nugget dark matter model. *Physical Review D*, 99(4):043535, February 2019. doi: 10.1103/PhysRevD.99.043535.
- VanDevender, J.P. et al. Detection of magnetized quark-nuggets, a candidate for dark matter. *Scientific Reports*, 7:8758, August 2017. doi: 10.1038/s41598-017-09087-3.
- VanDevender, J.P. et al. Radio frequency emissions from dark-matter-candidate magnetized quark nuggets interacting with matter. *arXiv e-prints*, art. arXiv:2005.05316, May 2020a. doi: 10.48550/arXiv.2005.05316.
- VanDevender, J.P. et al. Mass distribution of magnetized quark-nugget dark matter and comparison with requirements and observations. *Scientific Reports*, 10:17903, October 2020b. doi: 10.1038/s41598-020-74984-z.
- VanDevender, J.P. et al. Results of Search for Magnetized Quark-Nugget Dark Matter from Radial Impacts on Earth. *Universe*, 7(5):116, April 2021a. doi: 10.3390/universe7050116.
- VanDevender, J.P. et al. Limits on Magnetized Quark-Nugget Dark Matter from Episodic Natural Events. *Universe*, 7(2):35, February 2021b. doi: 10.3390/universe7020035.
- VanDevender, J.P., Sloan, T. and Glissman, M. A Search for Magnetized Quark Nuggets (MQNs), a Candidate for Dark Matter, Accumulating in Iron Ore. *Universe*, 10(1):27, January 2024. doi: 10.3390/universe10010027.

- Vilenkin, A. and Everett, A.E. Cosmic Strings and Domain Walls in Models with Goldstone and Pseudo-Goldstone Bosons. *Physical Review Letters*, 48(26):1867–1870, June 1982. doi: 10.1103/PhysRevLett.48.1867.
- Weidenspointner, G. et al. The sky distribution of positronium annihilation continuum emission measured with SPI/INTEGRAL. *Astronomy and Astrophysics*, 450(3):1013–1021, May 2006. doi: 10.1051/0004-6361:20054046.
- Weinberg, S. A new light boson? *Physical Review Letters*, 40(4):223–226, January 1978. doi: 10.1103/PhysRevLett.40.223.
- Weniger, E.J. and Cížek, J. Rational approximations for the modified Bessel function of the second kind. *Computer Physics Communications*, 59(3):471–493, July 1990. doi: 10.1016/0010-4655(90)90089-J.
- Werhahn, M. et al. Cosmic rays and non-thermal emission in simulated galaxies - I. Electron and proton spectra compared to Voyager-1 data. *Monthly Notices of the RAS*, 505(3): 3273–3294, August 2021. doi: 10.1093/mnras/stab1324.
- Wilczek, F. Problem of strong P and T invariance in the presence of instantons. *Physical Review Letters*, 40(5):279–282, January 1978. doi: 10.1103/PhysRevLett.40.279.
- Witten, E. Cosmic separation of phases. *Physical Review D*, 30(2):272–285, July 1984. doi: 10.1103/PhysRevD.30.272.
- Yang, Z.H. and Chu, Y.M. On approximating the modified Bessel function of the second kind. *Journal of Inequalities and Applications*, 2017(1), February 2017. ISSN 1029-242X. doi: 10.1186/s13660-017-1317-z.
- Zhitnitsky, A. Width of the 511 keV line from the bulge of the galaxy. *Physical Review D*, 76(10):103518, November 2007. doi: 10.1103/PhysRevD.76.103518.
- Zhitnitsky, A. Solar Extreme UV radiation and quark nugget dark matter model. *Journal of Cosmology and Astroparticle Physics*, 2017(10):050, October 2017. doi: 10.1088/1475-7516/2017/10/050.
- Zhitnitsky, A. Solar flares and the axion quark nugget dark matter model. *Physics of the Dark Universe*, 22:1–15, December 2018. doi: 10.1016/j.dark.2018.08.001.
- Zhitnitsky, A. The mysterious bursts observed by telescope array and axion quark nuggets. *Journal of Physics G Nuclear Physics*, 48(6):065201, June 2021a. doi: 10.1088/1361-6471/abd457.
- Zhitnitsky, A. Multi-Modal Clustering Events Observed by Horizon-10T and Axion Quark Nuggets. *Universe*, 7(10):384, October 2021b. doi: 10.3390/universe7100384.
- Zhitnitsky, A. The Pierre Auger exotic events and axion quark nuggets. *Journal of Physics G Nuclear Physics*, 49(10):105201, October 2022a. doi: 10.1088/1361-6471/ac8569.
- Zhitnitsky, A. The mysterious diffuse UV radiation and axion quark nugget dark matter model. *Physics Letters B*, 828:137015, May 2022b. doi: 10.1016/j.physletb.2022.137015.
- Zhitnitsky, A. Structure formation paradigm and axion quark nugget dark matter model. *Physics of the Dark Universe*, 40:101217, May 2023. doi: 10.1016/j.dark.2023.101217.
- Zhitnitsky, A.R. ‘Nonbaryonic’ dark matter as baryonic colour superconductor. *Journal of Cosmology and Astroparticle Physics*, 2003(10):010, October 2003. doi: 10.1088/1475-7516/2003/10/010.

Zwicky, F. Die Rotverschiebung von extragalaktischen Nebeln. *Helvetica Physica Acta*, 6: 110–127, January 1933.

List of Figures

1.1	Sketch of cosmological eras in the early universe. Commonly acknowledged cosmological eras are taken from Carroll and Ostlie (2017). Formation eras relevant to the AQN theory are indicated by the colored boxes.	5
1.2	Radial number density $n(z)$ in the range of $z \in [1.24 \times 10^{-9}, r_\star]$ cm for an AQN at $T_{\text{AQN}} = 1$ eV.	7
1.3	Schematic slice of an AQN (not true-to-scale).	8
2.1	Transitions from $\kappa \geq 1$ to $\kappa = 1$ for different environmental properties of n_{gas} and Δv . The critical temperatures $T_{\text{gas}}^{\text{crit}}$ mark the transitional gas temperature of $\kappa \neq 1$ to $\kappa = 1$	18
2.2	Spectral range for thermal emission from AQNs. The magnitude and width of a thermal spectrum increases for increasing T_{AQN} and can reach from radio to X-ray frequencies for extraordinary hot AQNs.	19
2.3	Non-thermal AQN emission spectrum for different R_{eff} . The position of the peak frequency is independent of the size of R_{eff}	22
2.4	Schematic construction of a k -d tree starting from particle ‘A’.	24
2.5	Sketch of the iterative algorithm to find the nearest neighbour of an AQN particle by walking down the k -d tree.	25
2.6	Schematic illustration of the SPH mapping process for Δv in an environment where a single AQN is surrounded by gas particles. Directions of velocity vectors are neglected since absolute relative velocities will be calculated as scalars.	26
3.1	(i) & (ii) M_{vir} versus median T_{AQN} for all particles in each of the 150 galaxy clusters. (i) Δv in the colormap increase for increasing cluster masses. AQNs in low M_{vir} with low Δv are still capable of obtaining high T_{AQN} . (ii) T_{gas} increases for increasing M_{vir} . High T_{AQN} in low M_{vir} can be reached because gas with low median T_{gas} resides in these environments. A value of $\kappa > 1$ therefore becomes more likely, which can positively contribute to a rise in T_{AQN}	32
3.2	Scaling relations of Δv versus T_{AQN} color-coded by (i) T_{gas} and (ii) n_{gas} . High T_{AQN} can still be reached for high T_{gas} , because $\kappa = 1$. In these regimes only Δv and n_{gas} will contribute to the internal temperature of AQNs.	33
3.3	Histograms of physical properties relevant to the AQN emission. Median values were taken for each mass bin, i.e. for 30 galaxy clusters, respectively.	35
3.4	Radial profiles of T_{AQN} , Δv , n_{AQN} , R_{eff} , n_{gas} and T_{gas} mapped onto AQN tracer particles. The median radial profile was taken for each mass bin (i.e. 30 galaxy clusters each) and compared to other mass bins in a region of $r \in [0, 1.5] r_{200}$	37

- 3.5 Median cluster spectrum with lines for each mass bin out of sample \mathcal{A} over a frequency range of $\nu \in [10^{-8}, 10^8]/(2\pi)$ eV. The solid, dash-dot-dotted, dashed, dash-dotted and dotted lines represent AQN thermal emission, non-thermal emission, ICM Bremsstrahlung, CR synchrotron emission and pion decay emission, respectively. 38
- 3.6 General spectral sketch for an arbitrary galaxy cluster exhibiting thermal AQN emission that outshines the background emission in a certain frequency band. The transition frequency ν_T is defined where $j_{\text{AQN,thermal},\nu} < j_{\text{background},\nu}$ with $\nu_{\text{min}} < \nu_T$ and ν_{min} being the minimum possible frequency where $j_{\text{AQN,thermal},\nu} > j_{\text{background},\nu}$ 39
- 3.7 Transition frequency-integrated spectral difference relation color-coded by (i) M_{vir} and (ii) $j_{\text{gas,thermal}}$. The slope of the $\nu_T\text{-}\Delta j(\nu_{\text{min}}, \nu_T)$ relation highly depends on the total thermal gas emission and the cluster mass. 39
- 3.8 Transition frequency-integrated spectral difference relation color-coded by (i) $\sqrt{T_{\text{gas}}}$ and (ii) Δv 40
- 3.9 $\nu_T\text{-}\Delta j(\nu_{\text{min}}, \nu_T)$ relation for cross-correlated galaxy clusters in the simulation. 41
- 3.10 $\nu_T\text{-}\Delta j(\nu_{\text{min}}, \nu_T)$ relation including synchrotron radiation with thermal gas emission as background contamination. (i) sample \mathcal{A} and (ii) sample \mathcal{B} , both color-coded by M_{vir} . The y -range and colormap in (ii) are adapted to ranges of sample \mathcal{A} 41
- 3.11 Spectral plot for non-thermal AQN emission and thermal Bremsstrahlung emission of the hot ICM. A small fraction of galaxy clusters shows small regions where AQN emission dominates gas emission. 43
- 3.12 $\nu_T\text{-}\Delta j(\nu_{\text{min}}, \nu_T)$ relation of galaxy clusters that fulfilled the conditions desired to identify an AQN signature in the high energy regime taken from sample \mathcal{A} , color-coded by (i) $\sqrt{T_{\text{gas}}}$ [eV] and (ii) Δv . Both plots show that galaxy clusters are populated in the lower parameter range. 43
- 3.13 Cross-correlated Fornax cluster in all maps; (i) AQN Thermal emission from ν_{min} to ν_T ; (ii) Thermal gas emission from ν_{min} to ν_T ; (iii) Difference image from AQN and gas emission; (iv) Synchrotron emission from ν_{min} to ν_T ; (v) Relative pressure of the ICM; (vi) AQN number density; (vii) Internal AQN temperature; (viii) Relative AQN-gas velocity; (ix) Effective AQN radius. . . 46
- 3.14 Cross-correlated Virgo cluster in all maps; (i) AQN Thermal emission from ν_{min} to ν_T ; (ii) Thermal gas emission from ν_{min} to ν_T ; (iii) Difference image from AQN and gas emission; (iv) Synchrotron emission from ν_{min} to ν_T ; (v) Relative pressure of the ICM; (vi) AQN number density; (vii) Internal AQN temperature; (viii) Relative AQN-gas velocity; (ix) Effective AQN radius. . . 47
- 3.15 Fornax cluster AQN, gas and synchrotron emission generated from LOFAR, WMAP, Planck, Euclid and XRISM energy ranges. Only minimal synchrotron emission is abundant in LOFAR bands, which results in almost no impact on the difference images. Higher energies than in the LOFAR range show no synchrotron emission. Gas completely outshines AQN emission in Euclid and XRISM energies. 48
- 3.16 Virgo cluster AQN, gas and synchrotron emission generated from LOFAR, WMAP, Planck, Euclid and XRISM energy ranges. Synchrotron emission is abundant in LOFAR, WMAP and Planck bands, which in return shows a slight impact on the difference images. Higher energies than in the Planck range show no synchrotron emission. Gas completely outshines AQN emission in Euclid and XRISM energies. 49

3.17	Radial profiles for cross-correlated galaxy clusters that showed a thermal AQN emission excess in spectral features. AQN emission was compared to gas, synchrotron and a superimposed, overlaid emission of gas and synchrotron obtained after integrating from ν_{\min} to the individual ν_T	50
A.1	High energy spectra from sample \mathcal{A} . Dashed lines represent thermal gas emission and dot-dot-dashed lines show non-thermal AQN emission. Only the lowest mass bin occasionally exhibits intersecting gas-AQN spectral lines.	78
A.2	Cross-correlated A119 cluster in all maps; (i) AQN Thermal emission from ν_{\min} to ν_T ; (ii) Thermal gas emission from ν_{\min} to ν_T ; (iii) Difference image from AQN and gas emission; (iv) Synchrotron emission from ν_{\min} to ν_T ; (v) Relative pressure of the ICM; (vi) AQN number density; (vii) Internal AQN temperature; (viii) Relative AQN-gas velocity; (ix) Effective AQN radius. . .	79
A.3	Cross-correlated A539 cluster in all maps; (i) AQN Thermal emission from ν_{\min} to ν_T ; (ii) Thermal gas emission from ν_{\min} to ν_T ; (iii) Difference image from AQN and gas emission; (iv) Synchrotron emission from ν_{\min} to ν_T ; (v) Relative pressure of the ICM; (vi) AQN number density; (vii) Internal AQN temperature; (viii) Relative AQN-gas velocity; (ix) Effective AQN radius. . .	80
A.4	Cross-correlated A1185 cluster in all maps; (i) AQN Thermal emission from ν_{\min} to ν_T ; (ii) Thermal gas emission from ν_{\min} to ν_T ; (iii) Difference image from AQN and gas emission; (iv) Synchrotron emission from ν_{\min} to ν_T ; (v) Relative pressure of the ICM; (vi) AQN number density; (vii) Internal AQN temperature; (viii) Relative AQN-gas velocity; (ix) Effective AQN radius. . .	81
A.5	Cross-correlated A2256 cluster in all maps; (i) AQN Thermal emission from ν_{\min} to ν_T ; (ii) Thermal gas emission from ν_{\min} to ν_T ; (iii) Difference image from AQN and gas emission; (iv) Synchrotron emission from ν_{\min} to ν_T ; (v) Relative pressure of the ICM; (vi) AQN number density; (vii) Internal AQN temperature; (viii) Relative AQN-gas velocity; (ix) Effective AQN radius. . .	82
A.6	Cross-correlated A2877 cluster in all maps; (i) AQN Thermal emission from ν_{\min} to ν_T ; (ii) Thermal gas emission from ν_{\min} to ν_T ; (iii) Difference image from AQN and gas emission; (iv) Synchrotron emission from ν_{\min} to ν_T ; (v) Relative pressure of the ICM; (vi) AQN number density; (vii) Internal AQN temperature; (viii) Relative AQN-gas velocity; (ix) Effective AQN radius. . .	83
A.7	Cross-correlated Centaurus cluster in all maps; (i) AQN Thermal emission from ν_{\min} to ν_T ; (ii) Thermal gas emission from ν_{\min} to ν_T ; (iii) Difference image from AQN and gas emission; (iv) Synchrotron emission from ν_{\min} to ν_T ; (v) Relative pressure of the ICM; (vi) AQN number density; (vii) Internal AQN temperature; (viii) Relative AQN-gas velocity; (ix) Effective AQN radius. . .	84
A.8	Cross-correlated Coma cluster in all maps; (i) AQN Thermal emission from ν_{\min} to ν_T ; (ii) Thermal gas emission from ν_{\min} to ν_T ; (iii) Difference image from AQN and gas emission; (iv) Synchrotron emission from ν_{\min} to ν_T ; (v) Relative pressure of the ICM; (vi) AQN number density; (vii) Internal AQN temperature; (viii) Relative AQN-gas velocity; (ix) Effective AQN radius. . .	85
A.9	Cross-correlated Perseus cluster in all maps; (i) AQN Thermal emission from ν_{\min} to ν_T ; (ii) Thermal gas emission from ν_{\min} to ν_T ; (iii) Difference image from AQN and gas emission; (iv) Synchrotron emission from ν_{\min} to ν_T ; (v) Relative pressure of the ICM; (vi) AQN number density; (vii) Internal AQN temperature; (viii) Relative AQN-gas velocity; (ix) Effective AQN radius. . .	86

List of Tables

1.1	AQN parameters that were utilized for the numerical analysis throughout this thesis.	8
2.1	Table of the cosmological parameters adapted from Planck Collaboration et al. (2014) utilized in the SLOW simulation. From the left to right, the columns correspond to the Hubble constant H_0 , the total matter density Ω_M , the cosmological constant Ω_Λ , the baryon fraction Ω_B , the normalization of the power spectrum σ_8 and the slope of the primordial fluctuation spectra n as it was described in Dolag et al. (2023).	28
3.1	Table of the cross-correlated galaxy clusters with physical properties from the simulation and their ability to show AQN signatures with and without synchrotron radiation in the background ($\Delta j_{\text{no synch}}$, $\Delta j_{\text{with synch}}$) at a transition frequency ν_T	42
3.2	Band-passes for LOFAR (van Haarlem et al., 2013), WMAP (Bennett et al., 2013), Planck (Tauber et al., 2010), Euclid (Laureijs et al., 2011) and XRISM (Mori et al., 2022) in units of eV.	46
B.1	Table of cluster properties from the mass bin $M_{\text{vir}} \in [0.8, 0.9] \times 10^{14} M_\odot$	87
B.2	Table of cluster properties from the mass bin $M_{\text{vir}} \in [1.0, 2.0] \times 10^{14} M_\odot$	88
B.3	Table of cluster properties from the mass bin $M_{\text{vir}} \in [4.0, 5.0] \times 10^{14} M_\odot$	89
B.4	Table of cluster properties from the mass bin $M_{\text{vir}} \in [7.0, 8.0] \times 10^{14} M_\odot$	90
B.5	Table of cluster properties from the mass bin $M_{\text{vir}} \in [1.1, 3.2] \times 10^{15} M_\odot$	91

Appendices

Appendix A

Supplementary Figures

A.1 Spectra

A.2 SPH Maps of Additional Local Galaxy Clusters

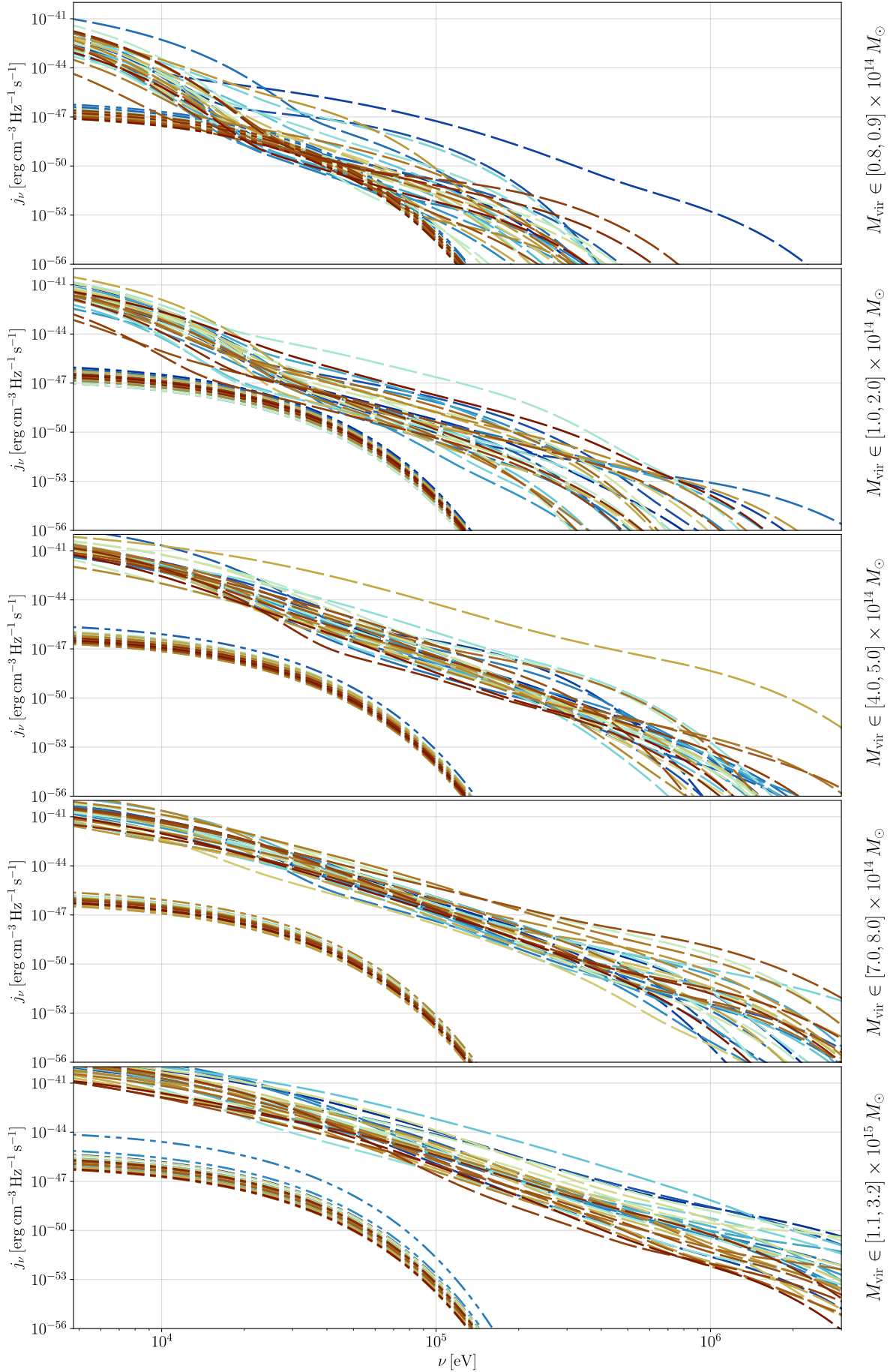


Figure A.1: High energy spectra from sample \mathcal{A} . Dashed lines represent thermal gas emission and dot-dot-dashed lines show non-thermal AQN emission. Only the lowest mass bin occasionally exhibits intersecting gas-AQN spectral lines.

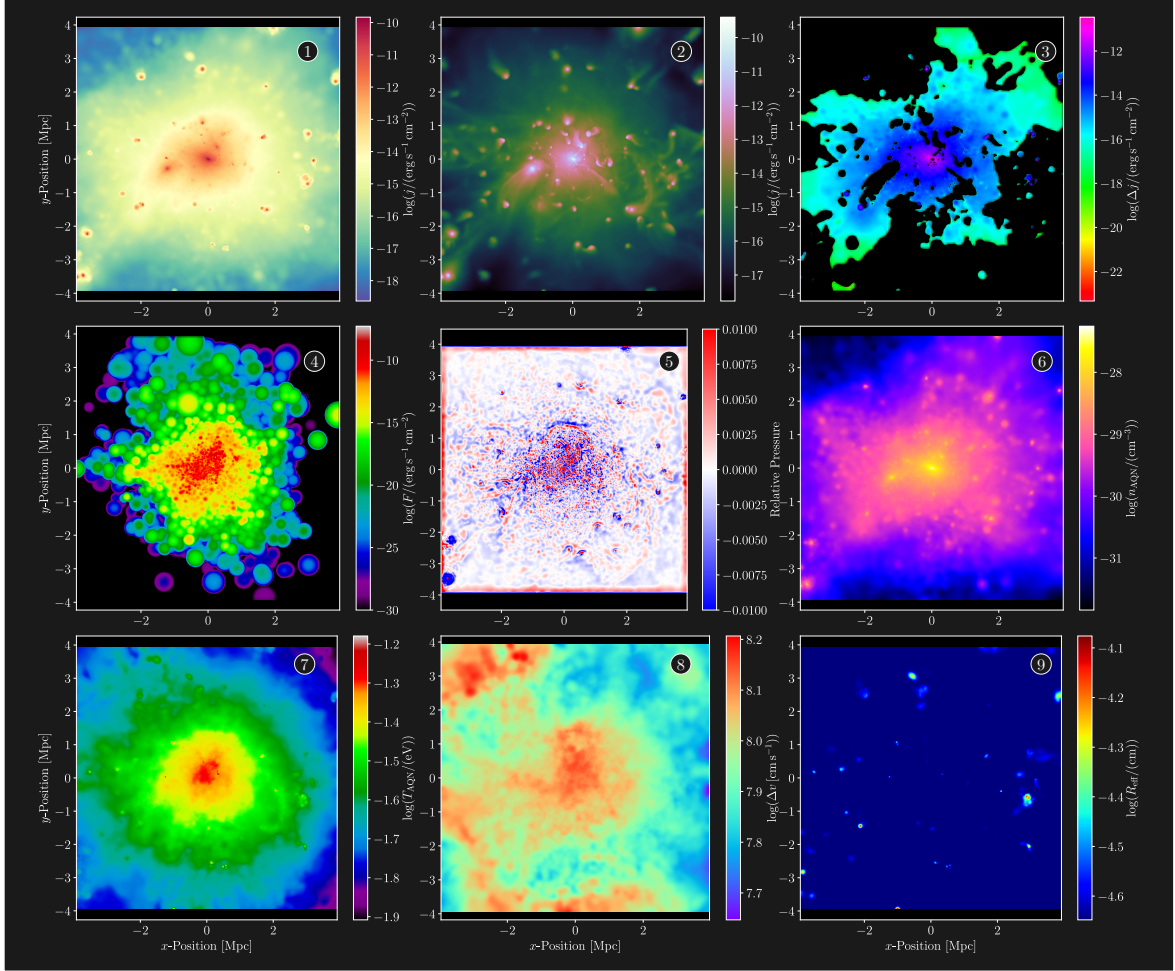


Figure A.2: Cross-correlated A119 cluster in all maps; (i) AQN Thermal emission from ν_{\min} to ν_T ; (ii) Thermal gas emission from ν_{\min} to ν_T ; (iii) Difference image from AQN and gas emission; (iv) Synchrotron emission from ν_{\min} to ν_T ; (v) Relative pressure of the ICM; (vi) AQN number density; (vii) Internal AQN temperature; (viii) Relative AQN-gas velocity; (ix) Effective AQN radius.

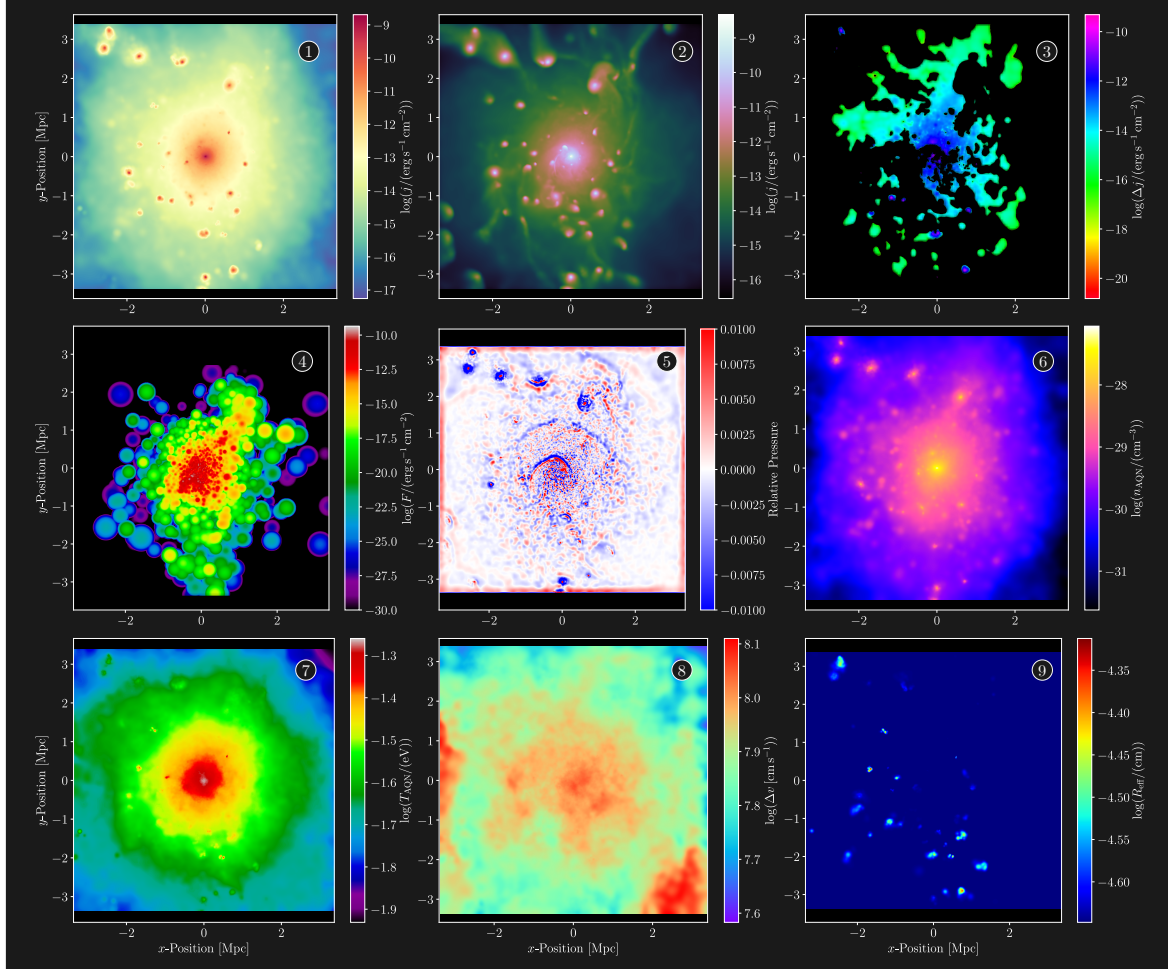


Figure A.3: Cross-correlated A539 cluster in all maps; (i) AQN Thermal emission from ν_{\min} to ν_T ; (ii) Thermal gas emission from ν_{\min} to ν_T ; (iii) Difference image from AQN and gas emission; (iv) Synchrotron emission from ν_{\min} to ν_T ; (v) Relative pressure of the ICM; (vi) AQN number density; (vii) Internal AQN temperature; (viii) Relative AQN-gas velocity; (ix) Effective AQN radius.

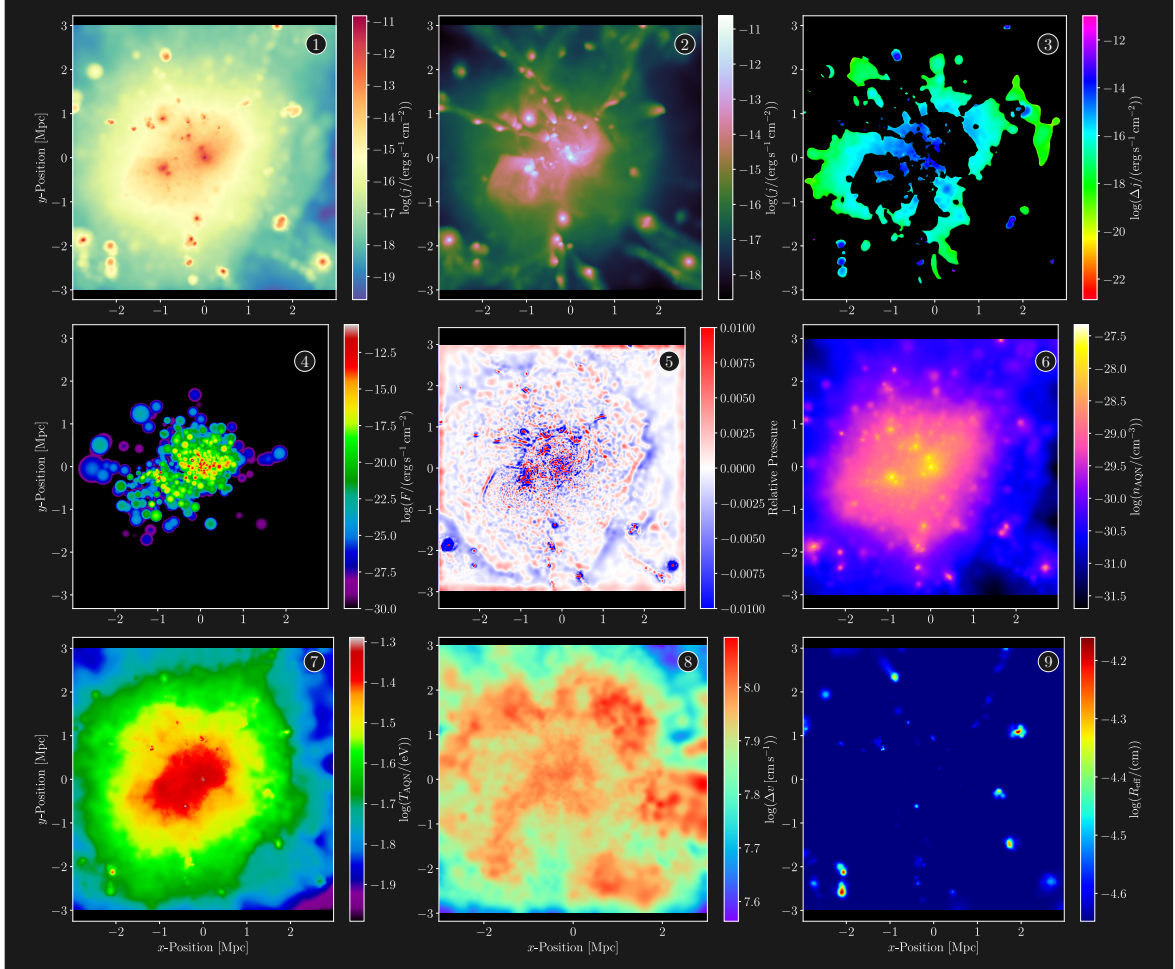


Figure A.4: Cross-correlated A1185 cluster in all maps; (i) AQN Thermal emission from ν_{\min} to ν_T ; (ii) Thermal gas emission from ν_{\min} to ν_T ; (iii) Difference image from AQN and gas emission; (iv) Synchrotron emission from ν_{\min} to ν_T ; (v) Relative pressure of the ICM; (vi) AQN number density; (vii) Internal AQN temperature; (viii) Relative AQN-gas velocity; (ix) Effective AQN radius.

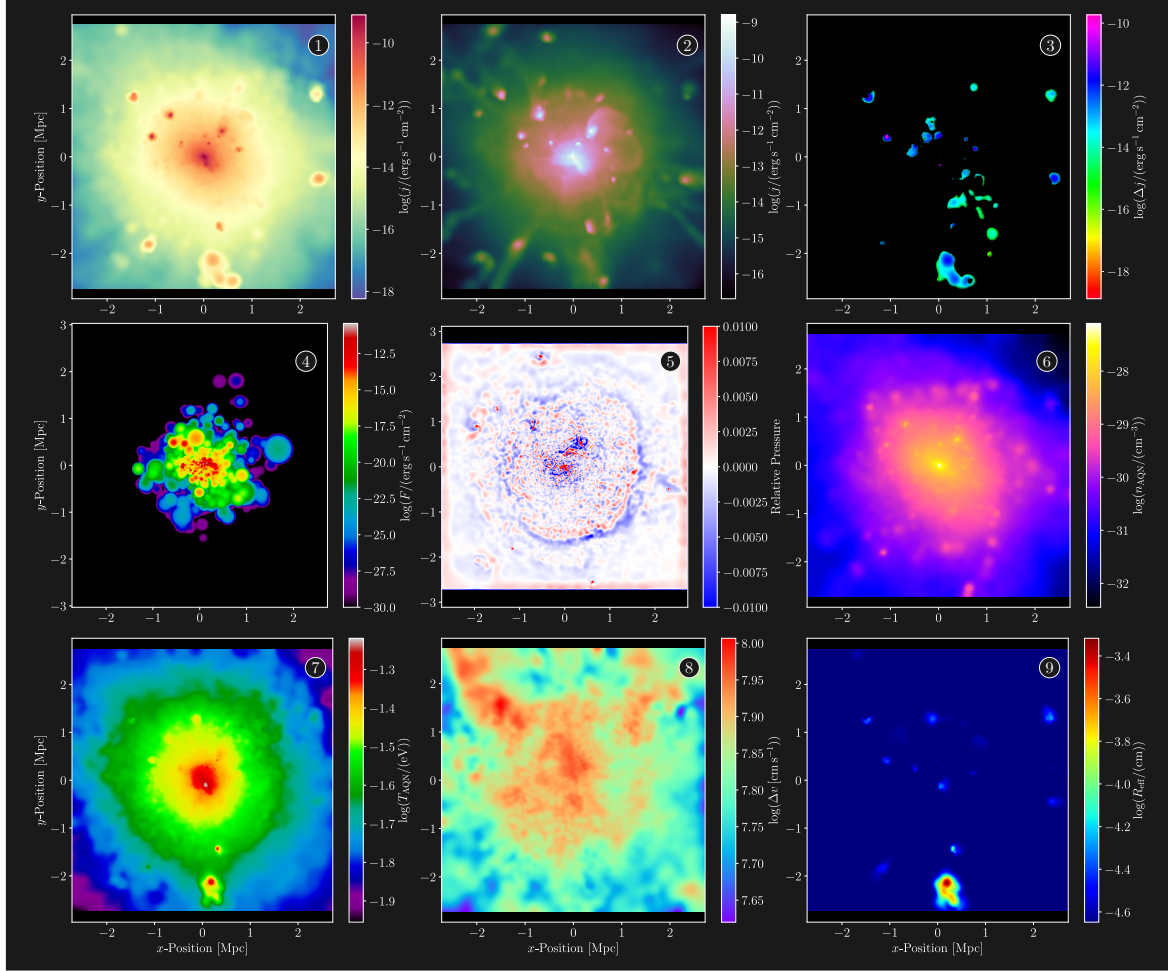


Figure A.5: Cross-correlated A2256 cluster in all maps; (i) AQN Thermal emission from ν_{\min} to ν_T ; (ii) Thermal gas emission from ν_{\min} to ν_T ; (iii) Difference image from AQN and gas emission; (iv) Synchrotron emission from ν_{\min} to ν_T ; (v) Relative pressure of the ICM; (vi) AQN number density; (vii) Internal AQN temperature; (viii) Relative AQN-gas velocity; (ix) Effective AQN radius.

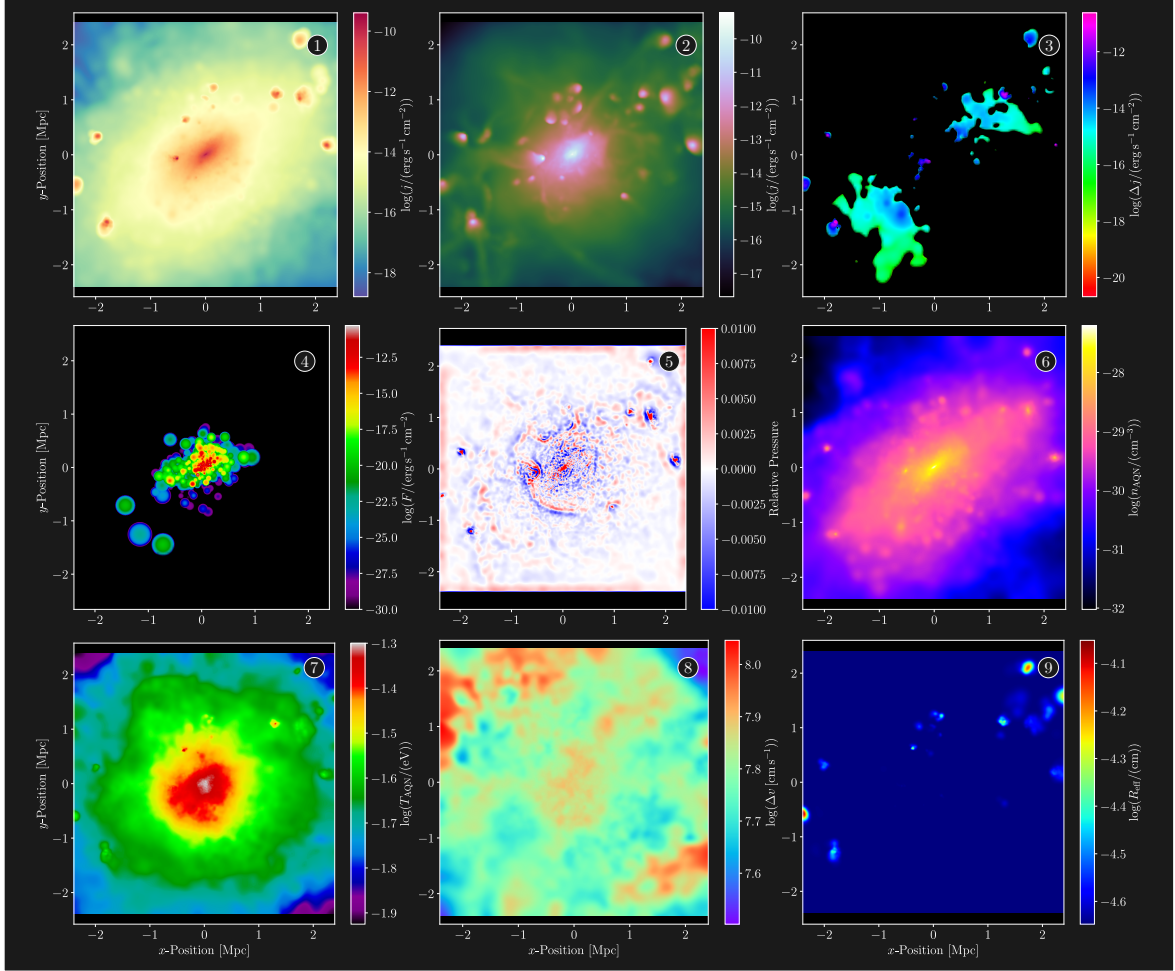


Figure A.6: Cross-correlated A2877 cluster in all maps; (i) AQN Thermal emission from ν_{\min} to ν_T ; (ii) Thermal gas emission from ν_{\min} to ν_T ; (iii) Difference image from AQN and gas emission; (iv) Synchrotron emission from ν_{\min} to ν_T ; (v) Relative pressure of the ICM; (vi) AQN number density; (vii) Internal AQN temperature; (viii) Relative AQN-gas velocity; (ix) Effective AQN radius.

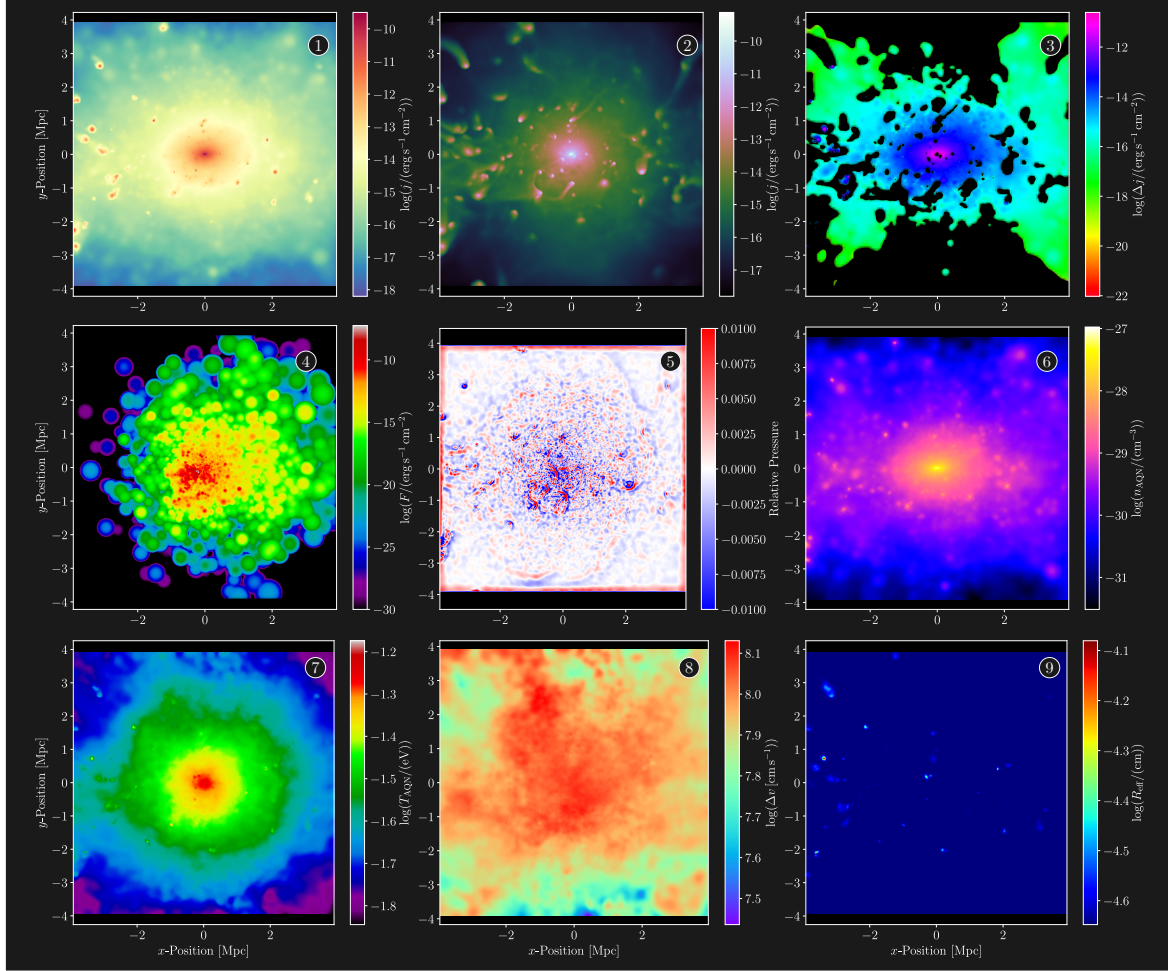


Figure A.7: Cross-correlated Centaurus cluster in all maps; (i) AQN Thermal emission from ν_{\min} to ν_T ; (ii) Thermal gas emission from ν_{\min} to ν_T ; (iii) Difference image from AQN and gas emission; (iv) Synchrotron emission from ν_{\min} to ν_T ; (v) Relative pressure of the ICM; (vi) AQN number density; (vii) Internal AQN temperature; (viii) Relative AQN-gas velocity; (ix) Effective AQN radius.

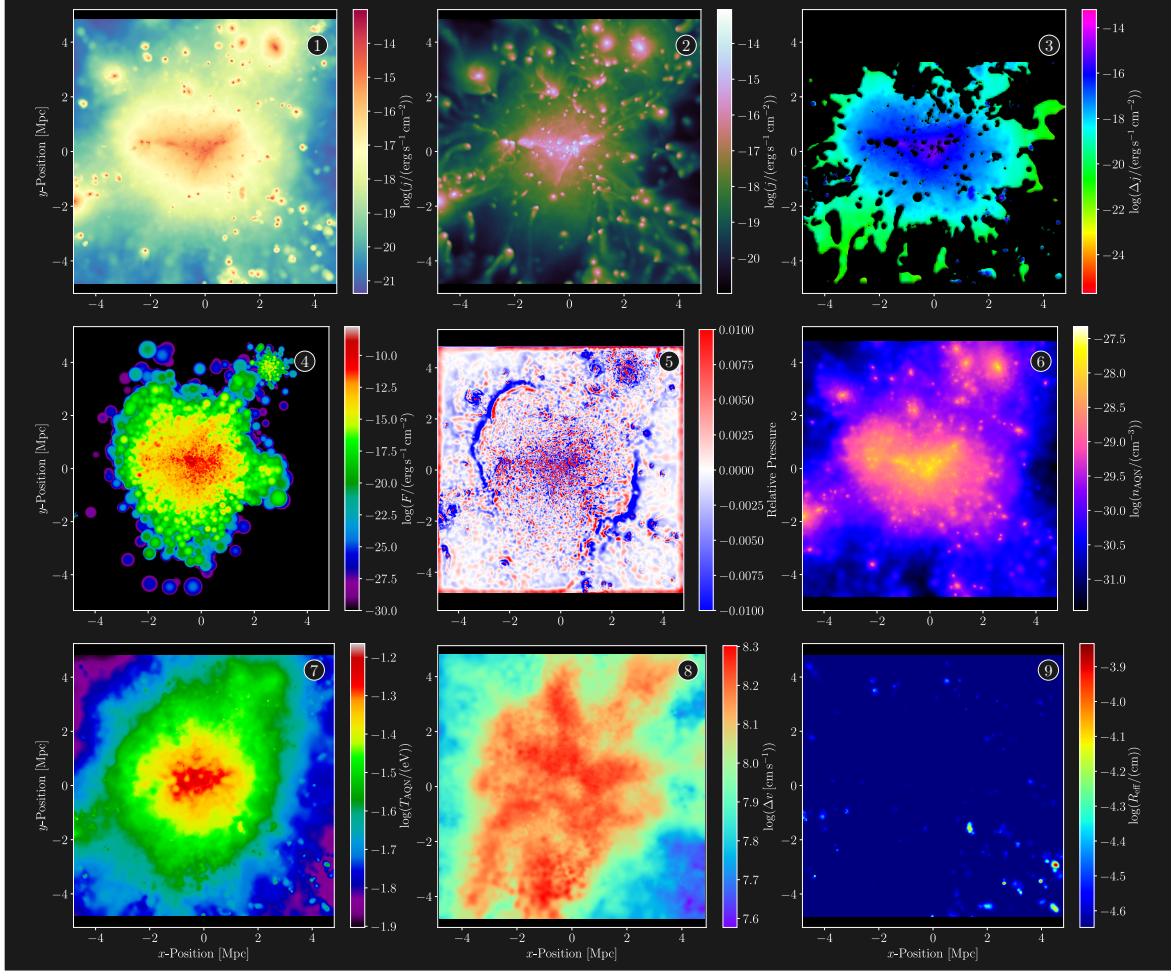


Figure A.8: Cross-correlated Coma cluster in all maps; (i) AQN Thermal emission from ν_{\min} to ν_T ; (ii) Thermal gas emission from ν_{\min} to ν_T ; (iii) Difference image from AQN and gas emission; (iv) Synchrotron emission from ν_{\min} to ν_T ; (v) Relative pressure of the ICM; (vi) AQN number density; (vii) Internal AQN temperature; (viii) Relative AQN-gas velocity; (ix) Effective AQN radius.

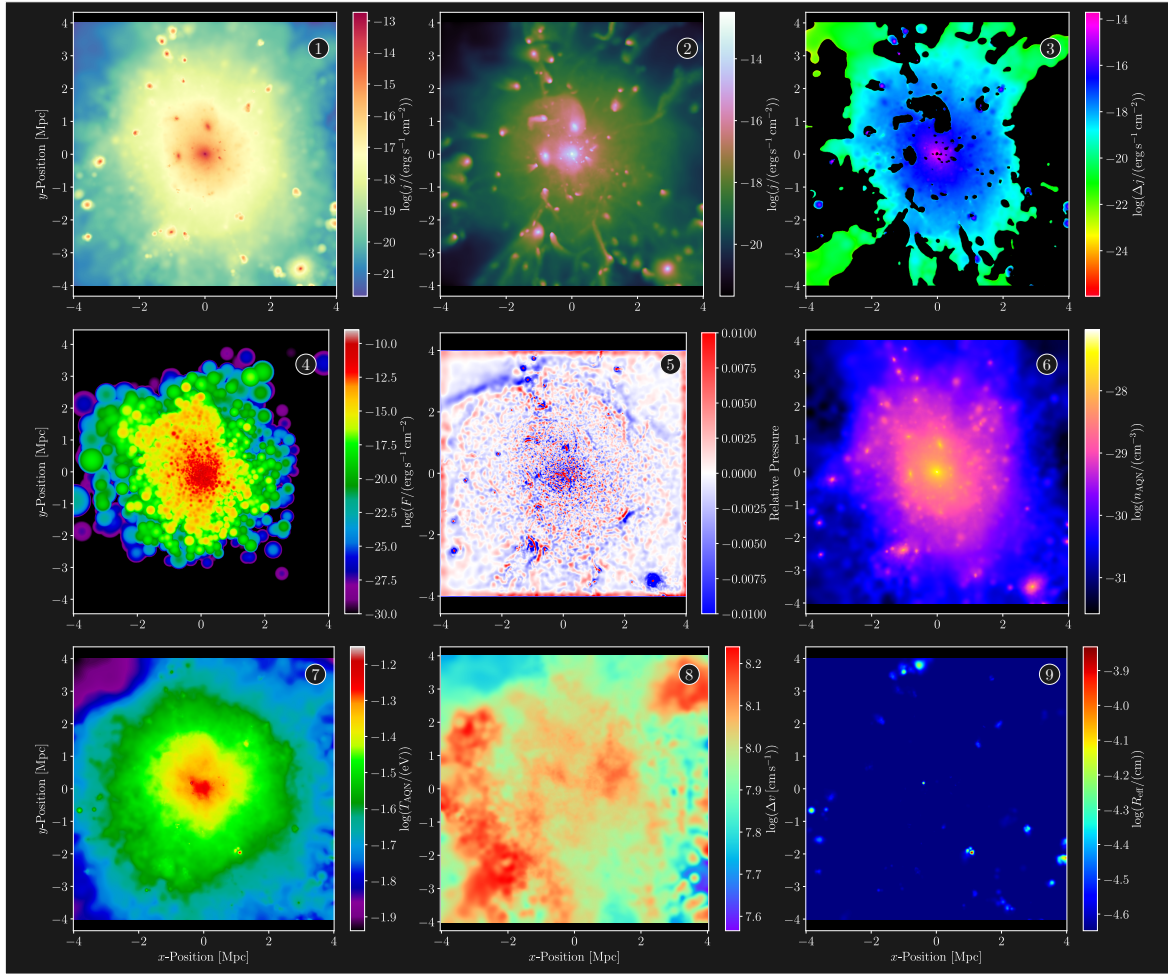


Figure A.9: Cross-correlated Perseus cluster in all maps; (i) AQN Thermal emission from ν_{\min} to ν_T ; (ii) Thermal gas emission from ν_{\min} to ν_T ; (iii) Difference image from AQN and gas emission; (iv) Synchrotron emission from ν_{\min} to ν_T ; (v) Relative pressure of the ICM; (vi) AQN number density; (vii) Internal AQN temperature; (viii) Relative AQN-gas velocity; (ix) Effective AQN radius.

Appendix B

Supplementary Tables

$M_{\text{vir}} \in [0.8, 0.9] \times 10^{14} M_{\odot}$					
HaloID	M_{vir} [$10^{14} M_{\odot}$]	Low ν_T [eV]	Low $\Delta j_{\text{with synch}}$ [$\text{erg cm}^{-3} \text{s}^{-1}$]	High ν_T [eV]	High $\Delta j_{\text{X-ray only}}$ [$\text{erg cm}^{-3} \text{s}^{-1}$]
(17, 42)	0.88	8.10×10^{-7}	2.14×10^{-32}	3.90×10^4	7.33×10^{-30}
(18, 14)	0.86	2.40×10^{-7}	7.50×10^{-34}	X	X
(18, 102)	0.89	2.67×10^{-9}	3.35×10^{-36}	X	X
(18, 128)	0.83	1.69×10^{-6}	4.18×10^{-32}	3.90×10^4	1.28×10^{-29}
(20, 156)	0.88	2.54×10^{-6}	8.48×10^{-32}	X	X
(21, 50)	0.82	3.67×10^{-6}	4.08×10^{-32}	6.07×10^4	4.90×10^{-30}
(21, 156)	0.81	X	X	6.78×10^4	4.36×10^{-30}
(21, 180)	0.89	5.10×10^{-8}	4.44×10^{-34}	4.87×10^4	4.64×10^{-30}
(21, 231)	0.83	4.10×10^{-6}	4.66×10^{-32}	4.69×10^4	2.39×10^{-30}
(21, 243)	0.89	2.55×10^{-4}	3.25×10^{-30}	2.90×10^4	2.78×10^{-32}
(21, 272)	0.8	2.64×10^{-6}	3.28×10^{-32}	X	X
(22, 91)	0.88	2.03×10^{-8}	2.58×10^{-34}	X	X
(22, 128)	0.89	1.04×10^{-3}	1.88×10^{-29}	X	X
(22, 152)	0.87	X	X	X	X
(22, 181)	0.88	X	X	8.78×10^4	1.51×10^{-30}
(22, 212)	0.85	3.47×10^{-7}	2.45×10^{-33}	X	X
(22, 267)	0.86	1.63×10^{-6}	2.09×10^{-32}	4.69×10^4	1.49×10^{-30}
(22, 272)	0.87	5.12×10^{-6}	8.10×10^{-32}	X	X
(22, 274)	0.88	1.65×10^{-9}	2.12×10^{-38}	X	X
(23, 49)	0.89	3.48×10^{-5}	5.75×10^{-31}	X	X
(23, 64)	0.82	2.04×10^{-6}	2.51×10^{-32}	X	X
(23, 129)	0.84	3.66×10^{-8}	2.68×10^{-34}	X	X
(23, 202)	0.89	X	X	X	X
(23, 225)	0.82	1.42×10^{-4}	2.58×10^{-30}	X	X
(23, 243)	0.89	4.83×10^{-7}	4.88×10^{-33}	3.01×10^4	3.16×10^{-31}
(23, 257)	0.84	1.03×10^{-5}	8.23×10^{-32}	2.90×10^4	3.36×10^{-30}
(23, 287)	0.86	X	X	5.44×10^4	7.56×10^{-32}
(23, 302)	0.83	6.85×10^{-8}	1.07×10^{-33}	4.52×10^4	1.32×10^{-29}
(24, 45)	0.84	X	X	3.62×10^4	1.50×10^{-31}
(24, 117)	0.9	7.40×10^{-6}	4.93×10^{-32}	4.69×10^4	1.49×10^{-30}

Table B.1: Table of cluster properties from the mass bin $M_{\text{vir}} \in [0.8, 0.9] \times 10^{14} M_{\odot}$.

$M_{\text{vir}} \in [1.0, 2.0] \times 10^{14} M_{\odot}$					
HaloID	M_{vir} [$10^{14} M_{\odot}$]	Low ν_T [eV]	Low $\Delta j_{\text{with synch}}$ [erg cm $^{-3}$ s $^{-1}$]	High ν_T [eV]	High $\Delta j_{\text{X-ray only}}$ [erg cm $^{-3}$ s $^{-1}$]
(6, 61)	1.73	5.81×10^{-7}	3.26×10^{-32}	X	X
(7, 90)	1.41	5.29×10^{-8}	1.36×10^{-33}	X	X
(9, 89)	1.8	3.47×10^{-7}	9.93×10^{-33}	X	X
(9, 109)	1.7	3.11×10^{-7}	7.42×10^{-33}	X	X
(9, 110)	1.99	5.31×10^{-6}	2.45×10^{-31}	X	X
(9, 111)	1.91	8.58×10^{-6}	1.88×10^{-31}	X	X
(9, 120)	1.82	1.39×10^{-5}	3.71×10^{-31}	X	X
(10, 30)	1.45	7.84×10^{-5}	6.88×10^{-31}	X	X
(10, 61)	1.98	4.33×10^{-7}	1.67×10^{-32}	X	X
(11, 61)	1.84	6.71×10^{-9}	X	X	X
(11, 101)	1.34	3.75×10^{-5}	1.09×10^{-30}	X	X
(11, 108)	1.77	3.06×10^{-6}	6.22×10^{-32}	X	X
(11, 110)	1.15	X	X	X	X
(12, 8)	1.71	2.67×10^{-9}	X	X	X
(12, 14)	1.73	5.02×10^{-7}	8.79×10^{-33}	X	X
(12, 36)	1.95	1.57×10^{-6}	1.47×10^{-32}	X	X
(12, 37)	1.88	1.26×10^{-8}	1.70×10^{-34}	X	X
(12, 41)	1.89	X	X	X	X
(12, 49)	1.97	6.63×10^{-6}	1.69×10^{-31}	X	X
(12, 95)	1.05	2.49×10^{-7}	5.96×10^{-33}	X	X
(12, 123)	1.67	X	X	X	X
(12, 124)	1.97	5.20×10^{-7}	1.39×10^{-32}	X	X
(12, 126)	1.89	2.18×10^{-8}	2.26×10^{-34}	X	X
(12, 129)	1.67	1.61×10^{-5}	3.33×10^{-31}	X	X
(12, 153)	1.43	X	X	X	X
(12, 157)	1.27	1.67×10^{-5}	3.98×10^{-31}	X	X
(13, 7)	1.84	1.47×10^{-4}	3.50×10^{-30}	X	X
(13, 9)	1.08	1.86×10^{-5}	4.56×10^{-31}	X	X
(13, 32)	1.88	2.83×10^{-8}	4.50×10^{-34}	X	X
(13, 42)	1.98	1.93×10^{-5}	5.08×10^{-31}	X	X

Table B.2: Table of cluster properties from the mass bin $M_{\text{vir}} \in [1.0, 2.0] \times 10^{14} M_{\odot}$.

$M_{\text{vir}} \in [4.0, 5.0] \times 10^{14} M_{\odot}$					
HaloID	M_{vir} [$10^{14} M_{\odot}$]	Low ν_T [eV]	Low $\Delta j_{\text{with synch}}$ [$\text{erg cm}^{-3} \text{s}^{-1}$]	High ν_T [eV]	High $\Delta j_{\text{X-ray only}}$ [$\text{erg cm}^{-3} \text{s}^{-1}$]
(3, 34)	4.67	4.35×10^{-5}	1.29×10^{-30}	X	X
(4, 20)	4.8	5.04×10^{-5}	1.52×10^{-30}	X	X
(4, 23)	4.7	6.88×10^{-6}	2.66×10^{-31}	X	X
(4, 26)	4.29	X	X	X	X
(4, 36)	4.23	2.72×10^{-8}	X	X	X
(4, 51)	4.78	4.02×10^{-7}	X	X	X
(5, 11)	4.39	1.63×10^{-6}	X	X	X
(5, 15)	4.04	4.47×10^{-9}	X	X	X
(5, 36)	4.72	7.81×10^{-7}	3.17×10^{-32}	X	X
(6, 13)	4.18	2.45×10^{-6}	1.26×10^{-31}	X	X
(6, 16)	5.0	7.77×10^{-9}	X	X	X
(6, 31)	4.82	4.58×10^{-6}	2.31×10^{-31}	X	X
(6, 40)	4.94	1.08×10^{-8}	X	X	X
(6, 51)	4.21	1.49×10^{-7}	X	X	X
(6, 54)	4.5	1.22×10^{-6}	X	X	X
(6, 62)	4.78	1.22×10^{-6}	4.14×10^{-32}	X	X
(6, 64)	4.64	2.41×10^{-5}	X	X	X
(6, 72)	4.26	4.26×10^{-6}	6.72×10^{-33}	X	X
(6, 84)	4.79	2.24×10^{-5}	3.47×10^{-31}	X	X
(7, 9)	4.32	4.42×10^{-6}	1.26×10^{-31}	X	X
(7, 14)	4.24	1.05×10^{-6}	X	X	X
(7, 32)	4.71	1.21×10^{-8}	X	X	X
(7, 51)	4.04	2.24×10^{-5}	3.01×10^{-31}	X	X
(7, 52)	4.06	5.40×10^{-7}	X	X	X
(7, 55)	4.7	2.78×10^{-7}	X	X	X
(7, 60)	4.13	1.05×10^{-6}	X	X	X
(7, 61)	4.08	2.46×10^{-4}	7.18×10^{-30}	X	X
(7, 65)	4.71	1.63×10^{-6}	X	X	X
(7, 66)	4.09	4.17×10^{-7}	1.54×10^{-32}	X	X
(7, 69)	4.9	7.14×10^{-6}	1.86×10^{-31}	X	X

Table B.3: Table of cluster properties from the mass bin $M_{\text{vir}} \in [4.0, 5.0] \times 10^{14} M_{\odot}$.

$M_{\text{vir}} \in [7.0, 8.0] \times 10^{14} M_{\odot}$					
HaloID	M_{vir} [$10^{14} M_{\odot}$]	Low ν_T [eV]	Low $\Delta j_{\text{with synch}}$ [$\text{erg cm}^{-3} \text{s}^{-1}$]	High ν_T [eV]	High $\Delta j_{\text{X-ray only}}$ [$\text{erg cm}^{-3} \text{s}^{-1}$]
(2, 22)	7.61	5.04×10^{-5}	\times	\times	\times
(3, 3)	7.86	2.31×10^{-7}	\times	\times	\times
(3, 6)	7.04	3.29×10^{-6}	\times	\times	\times
(3, 19)	7.94	9.95×10^{-6}	3.41×10^{-31}	\times	\times
(3, 21)	7.52	5.37×10^{-9}	\times	\times	\times
(3, 23)	7.11	1.43×10^{-7}	\times	\times	\times
(3, 26)	7.25	3.22×10^{-7}	\times	\times	\times
(3, 28)	7.23	1.38×10^{-7}	\times	\times	\times
(3, 37)	7.61	1.41×10^{-6}	\times	\times	\times
(3, 38)	7.05	1.28×10^{-7}	\times	\times	\times
(4, 14)	7.11	2.50×10^{-5}	8.60×10^{-31}	\times	\times
(4, 16)	7.51	1.63×10^{-6}	\times	\times	\times
(4, 22)	7.04	2.32×10^{-5}	\times	\times	\times
(4, 31)	7.86	3.01×10^{-5}	\times	\times	\times
(4, 32)	7.72	7.44×10^{-4}	4.22×10^{-29}	\times	\times
(4, 34)	7.16	2.75×10^{-4}	2.68×10^{-29}	\times	\times
(4, 35)	7.14	1.39×10^{-5}	\times	\times	\times
(4, 38)	7.82	3.12×10^{-5}	1.21×10^{-30}	\times	\times
(4, 41)	7.37	3.11×10^{-7}	3.21×10^{-33}	\times	\times
(4, 46)	7.33	3.47×10^{-7}	\times	\times	\times
(4, 47)	7.85	1.44×10^{-5}	1.18×10^{-30}	\times	\times
(4, 48)	7.71	9.90×10^{-8}	\times	\times	\times
(4, 49)	7.58	1.26×10^{-8}	\times	\times	\times
(4, 52)	7.5	3.34×10^{-7}	\times	\times	\times
(4, 54)	7.3	9.90×10^{-8}	\times	\times	\times
(4, 55)	7.17	1.39×10^{-5}	\times	\times	\times
(4, 56)	7.43	2.31×10^{-7}	\times	\times	\times
(4, 57)	7.6	1.02×10^{-4}	5.82×10^{-30}	\times	\times
(4, 58)	7.58	8.94×10^{-4}	3.46×10^{-29}	\times	\times
(5, 1)	7.74	8.72×10^{-7}	\times	\times	\times

Table B.4: Table of cluster properties from the mass bin $M_{\text{vir}} \in [7.0, 8.0] \times 10^{14} M_{\odot}$.

$M_{\text{vir}} \in [1.1, 3.2] \times 10^{15} M_{\odot}$					
HaloID	M_{vir} [$10^{14} M_{\odot}$]	Low ν_T [eV]	Low $\Delta j_{\text{with synch}}$ [$\text{erg cm}^{-3} \text{s}^{-1}$]	High ν_T [eV]	High $\Delta j_{\text{X-ray only}}$ [$\text{erg cm}^{-3} \text{s}^{-1}$]
(0, 1)	31.74	7.56×10^{-5}	\times	\times	\times
(0, 2)	16.78	1.66×10^{-7}	\times	\times	\times
(0, 3)	18.35	1.31×10^{-6}	\times	\times	\times
(0, 4)	21.65	\times	\times	\times	\times
(0, 5)	12.24	7.81×10^{-7}	\times	\times	\times
(0, 6)	19.6	1.82×10^{-6}	\times	\times	\times
(1, 1)	14.15	9.43×10^{-5}	4.42×10^{-29}	\times	\times
(1, 2)	20.08	7.97×10^{-6}	\times	\times	\times
(1, 3)	15.84	4.19×10^{-5}	\times	\times	\times
(1, 4)	18.22	2.30×10^{-9}	\times	\times	\times
(1, 5)	19.29	1.17×10^{-6}	\times	\times	\times
(1, 6)	17.03	3.33×10^{-9}	\times	\times	\times
(1, 7)	12.93	8.06×10^{-9}	\times	\times	\times
(1, 8)	18.0	6.49×10^{-7}	\times	\times	\times
(1, 9)	16.57	5.31×10^{-6}	\times	\times	\times
(1, 10)	16.19	2.31×10^{-7}	\times	\times	\times
(1, 11)	18.06	3.04×10^{-8}	\times	\times	\times
(1, 12)	17.02	1.11×10^{-5}	\times	\times	\times
(1, 13)	14.73	\times	\times	\times	\times
(1, 14)	15.75	2.49×10^{-7}	\times	\times	\times
(1, 15)	13.06	2.53×10^{-8}	\times	\times	\times
(1, 17)	15.51	8.44×10^{-5}	\times	\times	\times
(1, 18)	10.7	1.36×10^{-6}	\times	\times	\times
(1, 19)	14.21	1.61×10^{-5}	\times	\times	\times
(2, 1)	15.1	2.90×10^{-5}	\times	\times	\times
(2, 2)	13.51	4.31×10^{-9}	\times	\times	\times
(2, 3)	11.91	2.11×10^{-6}	\times	\times	\times
(2, 5)	13.1	5.81×10^{-7}	\times	\times	\times
(2, 6)	12.84	9.20×10^{-8}	\times	\times	\times
(2, 7)	12.72	5.51×10^{-6}	\times	\times	\times

Table B.5: Table of cluster properties from the mass bin $M_{\text{vir}} \in [1.1, 3.2] \times 10^{15} M_{\odot}$.

Appendix C

Abbreviations

Abbreviation	Meaning
AQN	Axion Quark Nugget
BBN	Big Bang Nucleosynthesis
CP	Charge-Conjugation Parity
CR	Cosmic Ray
CS	Color Superconducting
ICM	Intracluster Medium
ISM	Interstellar Medium
MQN	Magnetized Quark Nugget
MAQN	Magnetized Axion Quark Nugget
PQ	Peccei-Quinn
QCD	Quantum Chromodynamic
QGP	Quark-Gluon Plasma

Appendix D

Units

eV Equivalents for $c = \hbar = 1$ and $h = 2\pi$	
m_e	510998.950 eV
cm^{-1}	$1.973 \times 10^{-5} \text{eV}$
K	$8.617 \times 10^{-5} \text{eV}$

Danksagung

Ich möchte mich an dieser Stelle von ganzem Herzen bei denen bedanken, die eine wichtige Rolle in meinem Werdegang gespielt haben. Insbesondere Prof. Klaus Dolag und Dr. Ludwig Böss haben mir während meines Bachelorstudiums die faszinierende Welt der numerischen Astrophysik nahegebracht. Die Zusammenarbeit an neuen und spannenden Projekten war für mich eine bereichernde Erfahrung, und ich habe ihre Unterstützung sehr genossen. Ein besonderer Dank gilt auch Dr. Ildar Khabibullin für seine zusätzliche Betreuung und die inspirierenden Denkanstöße nach unseren wissenschaftlichen Austauschen. Klaus, Ludwig und Ildar standen mir stets zur Seite, wenn ich Hilfe benötigte, und gleichzeitig ließen sie mir den Freiraum, meine Ideen zu entwickeln. Diese Betreuung habe ich sehr geschätzt und wünschte mir, dass jeder Student das Glück hat, Ähnliches zu erleben.

Ohne Prof. Ludovic Van Waerbeke und Dr. Xunyu Liang hätte ich die komplexen Mechanismen der Axion Quark Nuggets nicht so intuitiv verstanden. Ihre Tipps und direkter Austausch haben meine Ergebnisse maßgeblich vorangebracht.

Die Zeit in der CAST-Gruppe mit all den freundlichen Mitgliedern habe ich sehr genossen. Ich kann mir keine bessere Gruppe vorstellen, in der man sowohl über spannende astrophysikalische Themen als auch über Alltägliches sprechen konnte. Insbesondere möchte ich mich bei Elena Hernández Martínez, Stephan Vladutescu-Zopp und Justo Gonzalez für die individuelle Unterstützung in manchen Herausforderungen während meiner Masterarbeit bedanken.

Ich hätte niemals gedacht, dass ich einmal einen Master in Astrophysik haben würde, und für die Erfüllung dieses Traums möchte ich insbesondere den Personen aus meinem persönlichen Umfeld danken. Ich bin sehr glücklich über die jahrelange finanzielle und moralische Unterstützung meiner interessierten und fürsorglichen Eltern. Danke, Mama und Papa. Auch meiner Schwester Phyllis, die stets Interesse an meinen astrophysikalischen Problemen zeigte und mir durchwegs Zuspruch gab, möchte ich herzlich danken.

Vielen Dank, Paul Jakobs, für deine hervorragenden Verbesserungsvorschläge zur Sprache und Formulierungen in meiner Arbeit.

Ein besonderer Dank gebührt Ferdinand Vongehr, dessen Unterstützung während meiner Masterarbeit mein Leben erheblich erleichtert hat.

Meiner Band Skyborn (Lukas Greber, Paul Jakobs und Eduardo Romero) möchte ich danken, dass sie mir während meiner Masterarbeit den Rücken freigehalten und die gesamte Organisation übernommen haben.

Ohne die tolle Zeit mit Leon Ecker, Surya Shivaprasad, Jan-Niklas Pippert, Bhashin Thakore und Parth Nayak während meines Masterstudiums hätte der Abschluss nur halb so viel Spaß gemacht.

Ein ganz besonderer Dank gilt auch der Hans-Rudolf-Stiftung, die mir mit ihrer finanziellen Unterstützung ein Leben in der Münchner Innenstadt ermöglicht hat. Dank ihrer Unterstützung konnte ich mich voll und ganz auf das Schreiben meiner Masterarbeit konzentrieren.

Declaration

I hereby declare that this thesis is my own work, and that I have not used any sources and aids other than those stated in the thesis.

München, den 11. März 2024

Julian Silvester Sommer